



Royal Netherlands  
Meteorological Institute  
*Ministry of Infrastructure  
and Water Management*

# Turbulent stress observations at Lake IJssel

F.C. Bosveld

De Bilt, 2022 | Technical report; TR-396



# Turbulent stress observations at Lake IJssel

Note: This report contains a large number of figures. To avoid interspersing the text too much all the figures are positioned at the end of the report (Chapter 13). The reader may want to open a copy of the report in a second window and use this window specifically for the figures while they are referenced in the text.

## Content

Turbulent stress observations at Lake IJssel .....	1
1 Project.....	3
1.1 Project assignment.....	3
1.2 Project results .....	4
1.3 Purpose of this report.....	5
2 Locations, measurement set-up and storm conditions.....	5
3 Instruments, data availability and data treatment .....	6
3.1 Data processing software.....	6
3.2 Meteo and hydro data .....	6
3.3 Sonic anemometer data.....	7
3.4 Inclinometers .....	8
4 Data issues with the sonic anemometer.....	9
4.1 The occurrence of data gaps .....	9
4.2 Resampling.....	9
5 Basic quality checks and comparison of state variables.....	10
5.1 Sonic anemometer thermometer.....	10
5.2 Inclinometers .....	11
5.3 Interference between standard wind instruments and the sonic anemometer.....	12
6 Quality checks of vertical wind speed and turbulence .....	12
7 Spectral characteristics .....	13
8 A method to correct EC stress observations for sonic vibration .....	16
8.1 Introduction .....	16
8.2 Check of spectral information in relation to resampling .....	16
8.3 Correction for the influence of vibrations. ....	17
8.4 All corrections .....	17
8.5 The drag relation on the basis of fully corrected EC-stress data .....	18
9 Results for the Nov 2018 – Jun 2019 period .....	19
9.1 Magnitude of the various corrections performed to the stress.....	19
9.2 Comparison between 20 Hz and 50 Hz based data. ....	19
9.3 The drag relations for FL47 and FL48 .....	19
9.4 The relation between stress and standard deviation of the horizontal wind .....	20

10 Summary and conclusions.....	21
11 References .....	22
12 Acknowledgement.....	22
13 Figures .....	23
Appendix A: Working and configuration of the Thies 3D UltraSonic Anemometer.....	70
Appendix B Influence of frame deformation on sonical wind speed and temperature .....	71
Appendix C Data archiving, processing and visualisation.....	72

## **Samenvatting** (in Dutch)

Dit rapport is de weerslag van de analyse van turbulentie observaties op twee locaties op het IJsselmeer. Het doel van de metingen was een beter inzicht te krijgen in de relatie tussen windsnelheid, golfhoogte en turbulente stress aan het water oppervlakte. Hiertoe zijn gedurende vier storm seizoenen metingen verricht met sonische anemometers op twee al bestaande locatie op het IJsselmeer (FL47 en FL48). Op deze twee locaties worden al essentiële andere parameters gemeten om tot een goede analyse van stress metingen te kunnen komen.

De eerste drie storm seizoenen zijn gebruikt om verbeteringen aan te brengen aan de meetopstelling. Het betreft twee problemen: 1) data uitval juist bij de meest interessante situaties met hoge wind snelheid; 2) Verstoring van het turbulente signaal door vibraties in het frame van de sonische anemometers, ook juist bij de meest interessante hoge windsnelheden. Hoewel de verbeteringen de problemen iets verminderd hebben blijven zij hinderlijk aanwezig in de tijdseries van het vierde en laatste stormseizoen.

Dit rapport beschrijft de waarnemingen en behandelt de correctie methoden die ontwikkeld zijn om tot bruikbare gegevens te komen. Door de, bij aanvang, onvoorziene problemen met de metingen was binnen het project onvoldoende tijd om een bevredigende inhoudelijke analyse van de gegevens uit te voeren.

Het resultaat van dit project is dan ook: 1) een methodiek om uit turbulentie data met variabele meet frequentie toch stress waarden en co-spectra af te kunnen leiden; 2) een methodiek om afwijkingen in de turbulentie metingen door vibratie effecten van de sonische anemometer te corrigeren; 3) een eerste maar beperkte inhoudelijke analyse van Cd-relaties op het IJsselmeer; 4) een dataset van gecorrigeerde stress metingen samen met relevante aanvullende parameters om nadere analysis op het gebied van golf-wind interactie mee uit te voeren

### **Summary**

This report is the result of the analysis of turbulence observations at two locations at Lake IJssel in the Netherlands. The aim of the measurements was to gain a better understanding of the relationship between wind speed, wave height and turbulent stress at the water surface. To this end, measurements were taken during four storm seasons with sonic anemometers at two existing locations on Lake IJssel (FL47 and FL48). At these two locations, essential other parameters are already measured in order to arrive at a good analysis of stress measurements.

The first three storm seasons were used to make improvements to the measurement setup. It concerns two problems: 1) Data loss especially in the most interesting situations with high wind speed; 2) Disruption of the turbulent signal by vibrations in the frame of the sonic anemometers, also especially at the most interesting cases with high wind speeds. While the improvements have mitigated the issues to some extent, they remain problematic in the time series of the fourth and final storm season.

This report describes the observations and discusses the correction methods that have been developed to arrive at useful data. Due to these unforeseen problems with the measurements there was insufficient time within the project to carry out a satisfactory analysis of the data.

The result of this project is therefore: 1) a method to derive stress values and co-spectra from turbulence data with a variable measuring frequency; 2) a methodology to correct turbulent stress observations for vibrational effects on the sonic anemometer; 3) a first but limited substantive analysis of Cd relations on Lake IJssel; 4) a dataset of corrected stress measurements together with relevant additional parameters to perform further wave-wind interaction analysis

## **1 Project**

### **1.1 Project assignment**

Turbulent wind stress over a wavy water surface, together with the related aerodynamic roughness, is a key parameter in the hydro-meteorological modelling chain of the Safety Assessment Instrument “WBI” (Wettelijk Beoordelingsinstrumentarium) for the Dutch primary flood defenses. Unfortunately

it is also a relatively uncertain parameter, and direct measurements of it are scarce. Measurements of this parameter are highly desirable (see [Informatie behoefte WBI-BOI veldmetingen](#)). Eddy correlation measurements with a high-frequency ultrasonic anemometer are a commonly applied method to measure such turbulent wind stresses, and the measurement sites at Lake IJssel offered a unique opportunity to measure these stresses over Lake IJssel.

The purpose of the ultrasonic wind measurements is to provide more clarity in the transfer of the turbulent wind impulse to the waves. To this end, Rijkswaterstaat has performed 3D ultrasonic wind measurements on Lake IJssel. More specifically, the intention was to measure the drag coefficient  $CD = (u^*/U10)^2$  within the full range of interest (in terms of wind and temperatures spanned by the ranges  $10 \text{ m/s} < U10 < 30 \text{ m/s}$  resp.  $-6\text{oC} < T_{air} - T_{water} < +6\text{oC}$ ) accurately within 5%.

Within this assignment, the usability and reliability of these new measurement setups and the archived data are examined.

More specifically, this assignment includes:

- Validating raw measurement data from the 3D Sonic Anemometer. Processing the raw measurement data into relevant parameters, including a substantiation of processing choices and corrections.
- Indicative substantiated analysis to determine whether the sonic provides sufficient signal quality and reliable parameters (means, standard deviations and covariances of wind components and temperature, as well as CD).
- Drafting and supplying transferable flow diagrams and algorithm descriptions that allow Rijkswaterstaat to see which actions have been performed and with which an external agency can program and carry out further data processing
- Reporting of the aforementioned matters plus substantiated recommendations for adjustments to the measurement set-up and data collection, and for analyzes of the complete data set.

## 1.2 Project results

In a first interim report (Bosveld, 2014) improvements have been proposed for the settings of the sonic anemometer, in order to make optimal use of the high time resolution of this instrument.

In a second interim report (Bosveld, 2015) it was established that the measurements carried out in the period 15-Sep-2014 up to and including Jan 21, 2015 are of better quality than the previous measurements. However, because of this better quality, other problems could only now be identified.

Firstly, in terms of mechanical stability. Strong vibrations, especially during high winds, seem to generate anomalies in the sonic anemometer signals. These deviations are correlated and lead to undesirable contributions to the covariances.

Secondly, there appear to be gaps and irregularities in the data collection. This problem is also more pronounced at high wind speeds.

As a result of this report, further improvements have been made to the measurement setups on FL47 and FL48:

- One of the sonic anemometer setups (on FL48) has been reinforced in an effort to reduce instrument vibration.
- Inclinometers with a faster response time are installed at both locations.
- The data collection has been adapted to reduce gaps and irregularities in the data flow.

This period (winter half year 2016-2017) is described in a 3rd report.

- The reinforced setup on FL48 does indeed seem to lead to some improvement with regard to the vibration problem.
- The problem of missing data at high wind speed has been partially solved by resampling the raw sonic data to a lower frequency.

- To correct the turbulent covariances for vibrational influences, a spectral method has been developed in which the disturbed high-frequency part of the spectrum is replaced by a modeled spectrum.

For the storm of 20-Nov-2016, this correction method was applied for data from FL48 (with reinforced setup) and reported in a supplement to the 3rd report. The impression is that this leads to realistic results.

For the 2018-2019 season, the sonic anemometer setup has now also been reinforced on FL47. The measuring posts FL47 and FL48 have also been replaced. It is possible that this also contributes to a more stable setup. In the summer of 2019, the sonic anemometer setups were dismantled.

### 1.3 Purpose of this report

This report analyzes a new set of observations taken in the period 14-Nov-2018 to 26-Jun-2019. It is being examined whether the adjustments to the measuring poles and the reinforcement of the sonic setup on FL47 actually lead to improvement. Subsequently, the developed correction methods (resampling and spectral correction) are implemented and evaluated. The question we want to answer is to what extent the current measurement setup and correction methods lead to stress values with sufficient quality to answer the questions formulated within the project assignment.

## 2 Locations, measurement set-up and storm conditions.

Measurement location FL47 is located in the central northern part of Lake IJssel in water between 4 to 6 m deep. This location has a fetch of at least 10 km in all direction. FL48 is located close to the western coast in shallower waters of 2 to 4 m deep. This location has a minimum fetch of 1.6 km in WSW wind direction. The locations FL47 and FL48 are indicated on the map in Figure 1. A reconstruction of the boom of the sonic anemometer was performed at FL47 to avoid instrument vibrations. For FL48 this was already done in an earlier stage. At both locations the platforms and the foundational tower has been replaced. Figure 2 shows photos of the masts and their instrumentation after the reconstruction.

The sonic anemometers are positioned at approximately 10 m above NAP. The 3D inclinometers are positioned at the lower side of the stem on which the sonic anemometers resides.

**Table 1 Height (m relative to NAP) of sensors at the two locations**

	FL47	FL48
Air temperature	5.14	5.26
Sonic 3D	9.95	10.05
Inclinometer	9.40	9.52
Wind vane	9.90	10.02
Cup-anemometer	10.35	10.47

The orientation of the cup-vane combination is 090° - 270° respectively. The sonic anemometer is in 225° direction. The north markers at the sonic anemometers were oriented to the north on-eye by using a ship compass (octans), and with help of the wind vane readings. The north markers at the inclinometers were oriented to the north on-eye by using the ship compass.

Quite some high wind occasions occurred in this measurement period, especially in the month of March 2019, and quite exceptionally a summer storm in June 2019. Here we list the days, or period of days with maximum 10 minute mean winds at or above 15 m/s. For cases that wind maximum was above 19 m/s the maximum wind is given between brackets. They are: 20181120, 20181207-10,

20181215,20181221, 20181229, 20190101, 20190108, 20190113, 20190117, 20190128, 20190207 (19.2), 20190209 (19.3), 20190303-04, 20190307 (19.2), 20190309 (21.6), 20190311-14 (19.7), 20190315-17 (19.8), 20190325, 20190608 (20.2).

### 3 Instruments, data availability and data treatment

A logbook for the current observational period was available. No specific remarks on the sonic anemometers are given. Although other information sources revealed the following significant events: The dismantling in June 2019 of the sonic configurations at both FL47 and FL48; the change from summer time to winter time in the logging at FL48; and the reset of the sonic datalogging clock at 20190319 10:30 UTC, in the period before time mismatch ranging from are. +153 to -11 seconds were found.

#### 3.1 Data processing software

For data processing and analysis use is made of the software package MOBIBASE, hereafter called MB. This software package is developed at KNMI (Bosveld, 2017).

High frequency data files from the sonic anemometers were transformed from the original data format (CSV) to MB sample-file data format (FORTRAN Binary with IEEE floating point value) with the MB-application SAMPTRNS. Data values were not changed. MOBIBASE software developments were done to allow for peculiarities of the sonic anemometer data streams. This includes resampling of the original approximately 55 Hz data to 50 and 20 Hz respectively. For each second the number of samples in the original data stream was archived.

From these sample-files 10-min reduced data are calculated and archived with the MB-application SAMPPROC\_STANDARD. This involves the derivation of the average, minimum, maximum and standard deviation of each parameter and all (co-)variances between the relevant sets of parameters. Also archived are the number of missing samples in the 10 minute period for each reduced parameter and each co-variance. The reduced data are stored in the MB-database “*ijsselm3*”.

#### 3.2 Meteo and hydro data

FL47 and FL48 are part of a network of measuring stations at Lake IJssel. In this network a number of standard observations are performed. Standard observations from the two locations FL47 and FL48 are provided for the period 14-Nov-2018 till 18-May-2019. Due to a data transmission problem these data were not available for the last period 18-May-2019 till 26-Jun-2019. Here all the data sources used in this study are described. A summary is given in Table 1.

Daily 10 minute reduced data are provided (filenames: <yyyymmdd>Stat.dat) of wind speed (FF), wind direction (DD), significant wave height (HM0), air temperature (TA), conductivity (C), Chloride concentration (CL), and in case of FL48 also water temperature (TW). Wind speed and direction are measured with a cup anemometer and wind vane respectively. They are referred to as standard wind measurements in the following to distinguish them from the sonic measurements. Time is in local wintertime. Data are read into the MB-database *ijsselm3* (with the MB-application TRANSFER).

Daily 1 Hz data of wind speed (FF) and wind direction (DD) are provided (filename: <yyyymmdd>Wind.dat). Although in these data files still columns are present for the 2D inclinometers we note that these have been replaced by 3D inclinometers and archived at a higher sample rate in the sonic anemometer data files. These data are transformed to MB-sample files (with SAMPTRNS) and 10 minute reduced data are generated and imported in MB-database *ijsselm3* (with SAMPPROC\_STANDARD). These reduced data should match the values obtained from the Stat.dat files. This is confirmed by a check for 3 days (20181115, 20190309, 20190517) for FL47 and for two days (20181115, 20190309) for FL48.

Daily 4 Hz data of the water level are provided (Waves.dat). These data are transformed to MB-sample files (with SAMPTRNS) and 10 minute reduced data (avg, max, min, sdv) are generated and imported in MB-database *ijsselm3* (with SAMPPROC\_STANDARD). The standard deviation of the

water level should correlate with the significant wave height from the Stat.dat files. This has been verified for the month of December 2018.

Precipitation is not measured at the sites FL47 and FL48. KNMI maintains a land covering rain product derived from the weather radar data, and calibrated on the basis of the ground based precipitation network. 5 minute based precipitation data are extracted for the locations FL47, FL48 and Cabauw for the period 201811-201906. These data are aggregated to 10 minute values. Note that the quality of this product is less good than of the KNMI rain gauge network. Moreover the weather radar detects rain at a certain height. Part or all of this rain may not reach the ground.

Time stamps of the data are given in local winter time. From 14-Nov-2018 till 12-Dec-2018 12:14 UTC Sonic data were given in local summer time. In all cases the time stamps are converted to Universal Time Coordinated (UTC).

**Table 2 Data sources with their sample rate and parameters**

Data file	Time stamp	Parameters
Sonic FL47	55 Hz	U V W T X Y Z
Sonic FL48	55 Hz	U V W T X Y Z
Wind FL47	1 Hz	FF DD
Wind FL48	1 Hz	FF DD
Waves FL47	4 Hz	WL
Waves FL48	4 Hz	WL
Stat FL47	10 min	FF DD WH TA C CL
Stat FL48	10 min	FF DD WH TA C CL TW

### 3.3 Sonic anemometer data

Thies 3D UltraSonic anemometers are employed at both locations. In Appendix A a few excerpts from the sonic anemometer manual are shown which clarify the operation principles of the sonic anemometers. Averaging of basic measurements inevitably gives rise to spectral loss in co-variances at the high frequency end of the spectrum. To avoid this averaging we have chosen to configure the Ultra Sonic in the raw data output mode.

In general time stamps are given in local winter time. However, the sonic data of FL48 has been time stamped in local summer time until 12-Dec-2018 12:14 UTC, this has been accounted for in the post-processing.

Hourly files of approximately 55 Hz data of the 3D sonic-anemometer/thermometers are available for the period 20181114 – 20190617. Due to a data failure sonic anemometer data for the period 20190424-20190528 are missing at FL48.

Timestamping is done at each new second, based on the data logger time. The data stream is not always continuous which makes the interpretation of the data complicated in terms of spectral characteristics. This happens in particular at high wind speeds which are the most interesting cases for this study.

By comparing high time resolution sonic wind speeds with 1 Hz cup-anemometer wind data it was found that the clocks of both systems deviate from each other. Table 2 lists the deviations found. No

correction was made for these varying delays. This means that when comparing 10 minute values of the standard meteorological instruments with the sonic anemometers extra deviations will occur.

**Table 3 Delay in seconds of sonic datalogging time compared to cup anemometer time**

Date \ Station	FL47	FL48
20181115	13.1	256.2
20181211	41.1	284.0
20181213	44.4	16.4
20190309	153.5	69.8
20190319 0000	175.3	
20190319 1030	-11.0	
20190325	0.0	
20190401	8.8	50.1
20190501	66.2	
20190517	78.9	

### 3.4 Inclinometers

Three dimensional inclinometers (x,y,z) were co-sampled with the sonic anemometer at lower sampling rate, typically 3 samples in a cycle of 5 sonic samples. This 3D inclinometers supersedes the original 2D inclinometers. Although these instruments are called inclinometers, we note that they in fact are accelerometers. Under static conditions they measure the component of the earth gravity vector projected on planes of reference, and output the results in terms of tilting angles. When conditions are not static, for example with vibrations, the result is a combination of tilt and the acceleration induced by these movements.

The instrument is oriented on eye to the North with help of a north indicator at the instrument and with lines at the platform that have a known orientation. From the documentation of the RWS Datalogger from Observer Instruments we find for the instrument reading:

Coordinate	Name	Rotation vector	Orientation
X	Roll	North-South	Positive is west down
Y	Pitch	East-West	Positive is south down
Z	Yaw	Vertical	North is 0, no orientation given

## 4 Data issues with the sonic anemometer

### 4.1 The occurrence of data gaps

The stability of the sampling rate has improved compared to previous measurement periods. Under normal operation there is a slight variation of the number of raw samples in a second. The amount typically varies between 54 and 56 samples. The nominal rate is 55.4 Hz. At this stage it is unclear whether this variation is caused by the sonic anemometer or by the data logger. Typically the first second of the hourly files contains even less sample (around 47). The first hourly file of the day has even less samples in the first second (typically 11). Here we suspect that the data logging process is the cause of the extra missing data. This may result from the CPU being occupied by closing and opening of the data files, which may interrupt the continuous process of data logging.

During some episodes, especially at strong winds, much more data are missing. It is important to determine the cause of these data downfall. Experience with sonic anemometers show that especially during rain these instruments may suffer from malfunctioning. Rain information was taken from the KNMI weather radar product.

In Figure 3 an overview is shown of the average number of samples per second together with wind speed and rain amounts for the whole period, and for both locations FL47 and FL48. Significant drops in sample rates are found during high wind periods. Overall FL47 shows slightly more data reduction at some occasions with high winds and rain than FL48. Section 4.2 on resampling describes how the statistics on missing data is derived.

In Figure 4 sampling rate is displayed as function of wind speed for both FL47 and FL48. Data are classified into no-rain and rain. Again stronger reductions are observed for FL47 as compared to FL48. Rate reduction increases with wind speed and becomes significant from 8 m/s onward. Although rate reduction also occurs when there is no rain, during rainy conditions the reduction is in general larger. Note that the amount of no-rain points is significantly larger than rain points.

In Figure 5 we zoom in at the windy period of 20190304 - 20190317. We see that at lower wind speeds no data reduction occurs even if there is rain (20190307 FL47), at moderate wind speeds with rain data reduction may occur (20190304 FL47 and FL48). High wind speeds are often accompanied by rain and then always data reduction occurs, but for example at 20190316 we see that at winds of 19 m/s less data reduction occurs when there is no rain.

If we zoom in further at the single strong wind day 20190314 for FL47 (Figure 6) we see that data reduction occurs especially in the rainy period before the peak of the storm. When the rain stops before 1200 UTC less data reduction occurs. The inclinometers show larger excursions during high wind, but excursions are much less than in the previous reported period (2016-2017). This may well be related to the new foundation of the mast. Also shown in the inclinometer graphs is the 10 minute average value. Slight changes are observed during the day when wind speed and direction vary. But, these effects are significantly smaller as compared to the previous periods. For FL48 (Figure 7) we see a comparable behaviour with slightly less data reduction

Missing data occurs especially during the combination of rain and high winds. But occasionally this occurs also with rain and low winds, or in rare situations when there is no rain. This correlation of missing values and rains/high winds suggest that it is not the data transmission that causes the problem. Moreover the newly placed more stable tower does not seem to have much influence on data reduction. The manufacturer (Thies) communicates that an internal quality check in the sonic anemometer is performed. It seems that when no reliable measurements are obtained during a measurement cycle no values are sent out for transmission. But there is no information provided on this by Thies.

### 4.2 Resampling

As data gaps occur primarily under conditions which are especially relevant for the current study we look whether it is possible to derive reliable stress data even when a significant part of the data is missing.

Bosveld and Beljaars (2003) give an account on the influence of sampling rate on the reliability of turbulent flux estimates. Based on their results we can conclude that missing values in the raw data stream are not particularly problematic for the estimation of co-variances, as long as the samples are more or less evenly distributed over the time interval of interest, and as long as resulting sampling rate is significantly larger than the rate at which dominant transporting turbulent eddies pass the measuring location. This rate is of the order of  $U/z$ , which at a wind speed of 20 m/s and a measuring height of 10 m is 2 Hz. However, missing values are more problematic for the calculation of spectra. And it is precisely through spectra that we can assess the quality of the stress observations.

To see how the samples are distributed in time we plot in Figure 8 for a few 60 minute time frames the number of samples in each second. We choose for both locations, FL47 and FL48, three cases with no data reduction, limited data reduction, and significant data reduction respectively. In all except the last (N47, significant data reduction) we see that the number of samples in each second stay above 20. For N47 with significant data reduction we see that sample rates often fall well below 20 Hz and there are seconds where no data are available at all. Differences in data reduction between the instrument at FL47 and FL48 remain unexplained.

A way to deal with the sometimes varying amount of raw data per unit of time is to resample the data stream with a lower sampling rate, say 20 Hz. No information is available on the timestamp of individual data points. Here we assume that in each second the available samples are equally spaced in time. The resampled time series is obtained by selecting for each time stamp, at intervals of 0.05 s, the original sample that is closest in time to this timestamp. Further analysis is on the basis of this 20 Hz resampled time series. We may expect that when the sampling rate drops below 20 Hz the calculated spectra will become unreliable. It remains to be seen whether the calculated stress is unreliable as well.

Occasionally we want to look into the spectral behaviour at higher frequencies. Therefore we also constructed a resampled time series at 50 Hz. It is clear that spectral analysis with this time series will become more quickly unreliable than the 20 Hz time series when it comes to episodes with missing data.

Together with the resampling, statistics is saved on the number of missing data. For each second the number of samples (N47, N48) in the original time series is saved in the first sample of that second in the resampled time series. These are the values displayed in Figure 8. During the data reduction process to 10 minute values average, minimum, maximum, and standard deviation of the number of samples per second is calculated and archived. These are the values displayed for example in Figure 3 until Figure 7.

## **5 Basic quality checks and comparison of state variables**

The resampling technique enables us to derive in a well-defined manner 10 minute reduced statistics. Before continuing with the quality of the stress observations we first perform a number of more basic quality checks. These checks are important to get confidence in the observations. Especially information on the stability of the equipment and on flow obstruction around the sonic anemometer are of importance here.

### **5.1 Sonic anemometer thermometer**

Figure 9 shows 10 minute values of the sonic wind components and sonic temperature for the complete period. Displayed are mean, maximum, and minimum value in each 10 minute interval. Only very few outliers were found in these time series. These outliers are labelled in the database and ignored in this graph. This suggests, as described in the manual (see Appendix A), that the sonic anemometer itself already performs an effective quality test. This may also be related to the missing of data records, although on this aspect the manual is not clear.

In Figure 10 time series are given of the sonic anemometer together with the standard wind and temperature observation at FL47 and FL48. For wind speed and wind direction the two timeseries overlap so well that the standard observations can often not be seen in the graph. See section 5.3 on the way sonic wind direction is corrected. The same data are displayed in the scatter diagrams of Figure 11. Wind speed and direction do compare reasonably, although a better correlation was

expected. Further inspection of the high frequency data revealed that there is a timing difference which varies between -11 and 284 seconds between the standard observations and the sonic anemometer, which introduces a decorrelation in the 10 minute values. For both FL47 and FL48 positive offset is observed of 1 to 3 °C, with higher values at higher temperature. Sonic temperature is influenced by humidity. As humidity is not measured at the locations a relative humidity is assumed of 80% to calculate the humidity corrected sonic temperature (labelled q-corr in the figure). The bias is now more constant over the full temperature range, and between 1 and 2 °C.

Sonic temperature is also influenced by the cross-wind speed which bends the sound path (Schotanus et al., 1983). This will result in a lower estimate of the speed of sound, and consequently a lower estimate of the temperature. The sonic is configured (by default) for cross-wind correction on sonic temperature (Initial value Command TC = 1). In Figure 12 the difference of observed sonic temperature and standard air-temperature is shown as function of the wind speed. Sonic temperatures are corrected for humidity by assuming a relative humidity of 80%. At both locations a positive offset is observed between 1 and 2 °C. This is larger than the temperature specifications of the manufacturer of 0.5 °C (Thies, 2015). Uncorrected cross wind would result in a -1°C deviation at 20 m/s. This is indicated by the curve in the left panel. Remarkably we see that at the underside of the bulk of the data the deviations tend to increase with increasing wind speed. In magnitude this deviation is of the same magnitude as the cross-wind correction, but with different sign. Selection on no-rain and no-missing raw data did not make a difference (not shown here). This remains unexplained at this stage.

## 5.2 Inclinometers

Three inclinometers are mounted close to the sonic anemometers in the x, y, and z direction. Figure 13 shows 10 minute values for FL47, and Figure 14 for FL48. Mean, maximum and minimum values are displayed. At FL47 the x-component (Roll) is around zero, and the y-component (Pitch) around -2.5°. Variations are limited to ±2°, and larger during strong winds. The z-component (Yaw) average around 70°. This is to be interpreted as the azimuthal orientation, and as such only small deviations of North (0°) are to be expected, thus at this stage unsure how to interpret this value. The z-component appears to have slightly more variation from mid-February 2019 onward, and from thereon is slightly increasing. At FL48 the behaviour is similar, with the x-component (Roll) on average at 1°, and the y-component (Pitch) at -0.5° with larger excursions when wind speed is high. The z-component is on the average around -35°, also here uncertain how to interpret this value. As at FL47 the z-component appears to have slightly more variation from mid-February 2019 onward, and from thereon is slightly decreasing.

Here we investigate the relation between movement of the inclinometers and the wind speed. Often a linear response between the squared wind speed (Stalling pressure) and movement of a construction is observed. Figure 15 displays the relation between the standard deviation of the inclinometer x- and y-component as function of the squared wind at both locations. Here the amplitude of the sdv, ( $\sqrt{sx_i^2 + sy_i^2}$ ) is plotted on the y-axis. This shows a more or less linear response, especially at higher wind speeds. At FL47 the wind response is stronger than at FL48. In the lower panels the ratio between the two standard deviations, in terms of  $\text{atan2}(sx_i, sy_i)$  (phase < 45° then  $sx_i < sy_i$ ), is displayed as function of wind direction. This means when they are equal the phase is 45°. A definite relation is seen with larger x-component (Roll) movements at northerly and southerly winds, and larger y-component (Pitch) movements with easterly and westerly winds. Around the wind direction of 180° a secondary branch is seen, which is more pronounced for FL48. Until now this second branch is unexplained.

Spectra of the inclinometer readings for four periods with different wind speeds (3.5, 7.0, 10.0, and 13.0 m/s) reveal a dominant frequency around 1 Hz for FL47 (see Figure 16) and 1.5 Hz for FL48 (see Figure 17). In general peak levels are higher with increasing wind speed. FL47 shows also smaller contributions around 5 Hz, at FL48 this contribution is spread over a broader range of frequencies. Also apparent is a lower intensity broad band contribution especially at higher wind speeds. If we interpret the variation in the inclinometer values as horizontal accelerations then we can make an estimate of the speed involved. Given a sigma of 0.4° at 20 m/s. This corresponds with an acceleration  $0.4/57 \text{ (rad)} \times 9.8 \text{ (m/s}^2) = 0.07 \text{ m/s}^2$ . At a frequency of 1 Hz this is 0.07 m/s movement speed.

### 5.3 Interference between standard wind instruments and the sonic anemometer

The standard wind instruments and the sonic anemometer are positioned at the same level and approximately 1 m apart. Some interference and flow obstruction may be present depending on wind direction. We investigate this interference by comparing wind speeds and wind directions of the standard wind instruments and the sonic anemometer as a function of wind direction. Note that sonic wind direction have been corrected for FL47 with  $+15^\circ$ , and for FL48 with  $+3^\circ$ , based on a comparison with the standard wind direction observations over the full circle.

Figure 18 shows wind speed ratios and wind direction differences as function of wind direction for FL47 (upper panel) and FL48 (lower panel). Cases are selected with wind speed above 3 m/s. Individual observations show large variations, but on average wind speed ratios show variations as function of wind direction of typically 2%. Wind direction difference shows typical variations of a few degrees over the full wind direction range. Both locations show the same characteristics as function of wind direction. For both locations we observe a significant deviation in wind speed ratio around  $DD=50^\circ$  ( $52^\circ$  at FL47, and  $56^\circ$  at FL48). This corresponds approximately with the wind blowing from the cup-vane rack towards the sonic anemometers.

## 6 Quality checks of vertical wind speed and turbulence

Flow obstruction around the sonic measuring volume has potential effects on the quality of the stress observations. This can be understood by realising that a tilt of streamlines through the measuring volume will result in contamination of the vertical wind speed by the horizontal wind speed. As fluctuations in the horizontal wind speed are in general significantly larger than in the vertical wind speed, this will have a significant influence on the stress estimates.

Flow obstruction around the sonic can be studied by looking at the tilt of the streamlines through the measuring volume of the instrument. Important factors that affects streamline tilt are: (1) non-horizontal orientation of the sonic, this results in a sinus response; (2) the stem on which the transducers of the sonic anemometer are mounted will in general lead to a positive tilt of the streamlines regardless of the wind direction; (3) when the sonic is in the wake of the cup-vane combination, streamline tilt may be of the same order as deviations in horizontal direction measurements; (4) the transducers and their bearings, given the design of the sonic this influence is expected to have a  $120^\circ$  rotational symmetry. See Lee et al. (2004, Chapter 3) for an account on coordinate systems and flux bias corrections.

Figure 19 shows the observed slope of the streamlines as function of (sonic) wind direction. The slope is derived from the ratio of observed 10-min mean vertical and horizontal wind speeds. Only data are plotted when wind speeds are larger than 3 m/s. For both location around 50 degrees a well-defined obstruction is observed as was also found in Figure 18 for the wind speed ratio between sonic anemometer and cup anemometer. This is most likely induced by the cup-vane combination. Point 1 and 2 of possible causes of stream line tilt mentioned above would result in a response that is sinus-like and an offset respectively. In the figure on-eye fits of such a response are drawn. Any deviations from the sinus-like response must be due to other influencing causes as listed under 3 and 4. Binned average values are shown. Piece wise linear functions connecting these binned average values are then used to perform the tilt corrections on the (co-)variances. As a check for the correct implementation of this procedure we also corrected the mean vertical wind speed itself. Figure 20 shows that indeed systematic deviations from zero in the vertical wind speed as function of wind direction have disappeared, except for the wind directions where the cup-vane combination obstructs the flow along the sonic anemometer.

We now turn to correction methods for the stress related to flow obstruction. A simple correction procedure by rotation is correct for scalar fluxes as temperature flux. Wyngaard (1981) shows that this method is only an approximation for the effect of streamline deformation on the stress. For the pure sinus response, as function of wind direction, introduced by a tilted sonic, the effect on the stress can be transformed away by a goniometric coordinate transformation. However, the remaining observed tilt is induced not only by a pure rotation of the streamlines but also by deformation of the streamlines. In the current situation the tilt angles and resulting corrections are relatively small. Therefore, we will

ignore the effect of streamline deformation, and apply a pure rotation to arrive at tilt corrected stress values.

X-Y inclinometer data are also available to measure the tilt of the sonic configuration. In Table 3 the results of the two methods to derive the orientation of the sonic anemometers relative to the vertical are summarized. It is clear that the two methods do not result in corresponding results. Unclear at this stage is the orientation of the x and y axis of the inclinometers relative to north and their signs, and unclear is how accurate the perpendicular mounting of the inclinometers on the stem of the sonic anemometers is.

The same X-Y inclinometers can be used to monitor the stability of the platform. The idea is that wind and the resulting waves may deflect the platform and supporting construction of the sonic anemometer in the downwind direction. Figure 21 shows tilt angles derived from the inclinometer combinations as function of wind direction. Shown are, for both locations, the tilt (deviation from the vertical) and the azimuth (direction) of the tilt relative to north. Only a small effect of wind direction is observed.

**Table 4 Slope and of azimuth sonic derived from x-y inclinometer readings and of streamline tilt analysis at FL47 and FL48.**

Location	x-y inclinometers		On-eye sinus fit	
	Tilt (o)	Azimuth (o)	Amplitude (o)	Direction (o)
<b>FL47</b>	2.30	186	1.5	200
<b>FL48</b>	0.95	124	1.5	300.

## 7 Spectral characteristics

Analysing turbulent data by using spectral information may help to judge the quality of the data. The functional form of spectra and co-spectra in the lowest atmospheric layers is well established (Kaimal et al. (1972), and a comparison with observed spectra may reveal shortcomings in the observations.

As an introduction to various spectral characteristics we show in Figure 22A-D co-spectral information from turbulence observation at the 60-m level of the Cabauw meteorological tower for a case with wind speed of 10 m/s. In Figure 22A the co-spectrum is shown for the component along the mean wind vector (YS060) and the vertical wind (WS060). These are the components that form the stress along the direction of the mean wind. The upper left panel shows the power spectra of the two parameters. The horizontal axis represents frequency at a logarithmic scale. Vertically the power spectrum multiplied by frequency is shown. The multiplication with frequency ensures that, with a logarithmic frequency scale, areas under the curve are proportional to the contribution to the total variance of the two components. A strong decrease in contribution is observed when going to higher frequencies. Variance of the horizontal wind is in general significantly larger than variance in the vertical wind. The spectrum shows that this is caused by large low frequency contributions. Going to higher frequencies we see that the two spectra become comparable in magnitude.

The upper right panel shows the co-spectrum. Here a (negative) peak, corresponding to downward transport, is observed and a decrease of contributions when going to higher frequencies and when going to lower frequencies. The peak frequency is a function of wind speed, measuring height, and atmospheric stability.

The lower left panel represents the coherence spectrum, or to be precise the square root of the coherence spectrum. It is 1 at a given frequency, when the two signals are perfectly correlated at that specific frequency. It is 0 when there is no correlation. If the coherence spectrum were 1 over the whole frequency range (and the phase spectrum, see below, was constant and zero) then the co-spectrum would be equal to the square root of the product of the two power spectra. In this case we see that the coherence is maximal around the peak frequency and decreases when going to higher values. This implies that the co-spectrum falls-off more rapidly than the power spectra.

The coherence is defined as the factor between the square of the co-spectrum and the product of the two power spectra. When the focus is more on the co-spectrum it is more intuitive to plot the square root of the coherence (as is done for most co-spectra in this report), which then represents the factor between the co-spectrum and the geometric mean of the two power spectra.

Finally, in the lower right panel the phase spectrum is displayed. This shows the phase relation between the two signals at a specific frequency. The y-axis is in units of the full circle. 0 means in phase, 0.25 means exactly out of phase, and 0.5 means a half circle out of phase (anti phase). A constant phase spectrum is observed at a value of 0.5, which means that vertical and (along wind) horizontal wind fluctuations are anti-correlated at all frequencies.

A subtle unexpected feature is observed in the high frequency range of the co-spectrum, where the trend toward zero stops around 0.6 Hz. Also the coherence fails to go to zero. This issue is not further pursued here.

In Figure 22B the same type of information is displayed, but now for the cross wind and the vertical wind. Here we see that the coherence spectrum is much smaller than in the along wind case (note the difference in y-axis scaling). Consequently the co-spectrum is much smaller in magnitude and also has a less well defined signature. This is in line with the expectation that the mean momentum transport is with the along wind component.

In Figure 22C the same type of information is displayed, but now for the along wind and the cross wind component. Here we see that the coherence spectrum is relatively small, but there is still a reasonable amount of correlation.

In Figure 22D the co-spectral information of the vertical temperature flux is displayed. The temperature power spectrum shows unexpected high values at high frequencies, whereas a decrease towards zero is expected. As the coherence with the vertical wind goes to zero only a limited contribution in the co-spectrum is observed at these high frequencies. Note, however, that the phase between  $w$  and  $t$  changes there from anti phase to in-phase.

The unexpected results on the high frequency side both for the stress- and the temperature flux co-spectrum, and especially the large deviations in the temperature power spectrum may hint at vibrations in the frame of the sonic anemometer. Such vibrations may induce changes in the path length between the transducers. In Appendix C an account is given of the effect of static and dynamic deviations of the transducer path on measured sonic wind speed and temperature. As long as the vibration cycle time is much longer than the cycle time between the upwind and downwind path of the sonic transducer pair sonic temperature deviations are more pronounced than wind speed deviations.

This example of the Cabauw tower was supposed to be more or less a text book situation. But already there, relevant issues with the turbulent observations become clear when looking at spectra. Now we turn to stress spectra of the Lake IJssel observations. Table 4 lists the periods for which co-spectral analyses are performed. Note that most of the periods have high winds, except for the period of 10-Mar-2019 which has low winds. To avoid missing data, which would deteriorate the spectral calculation, we use the 50 Hz resampled data.

Figures	Period (UTC)	Wind Speed	Wind Direction
Figure 23 (FL47) Figure 24 (FL48)	04-Mar-2019 1200-1500	17.0 m/s	258°
Figure 25 (FL47, FL48)	05-Mar-2019 1200-1500	9.7 m/s	236°
Figure 26 (FL47, FL48)	09-Mar-2019 1400-1700	16.5 m/s	285°
Figure 27 (FL47, FL48)	11-Mar-2019 1100-1400	18.1 m/s	291°

Figure 28 (FL47, FL48)	13-Mar-2019 1100-1310	15.4 m/s	263°
Figure 29 (FL47, FL48)	14-Mar-2019 0800-1100	13.1 m/s	227°
Figure 30 (FL47, FL48)	10-Mar-2019 0650-0850	3.6 m/s	165°

**Table 5 Periods for which co-spectral analyses are performed with meteorological characterisation base on observations from location FL47.**

Figure 23A-E displays for the period 04-mar-2019 1200-1500 UTC co-spectral information. This three hour period had an average wind speed of 17 m/s and a wind direction of 260°. Figure 23A shows the along wind component and the vertical wind for FL47, this is the stress spectrum. The (co-) spectrum shows a normal behaviour. As in the Cabauw case, a slight increase in coherence is found for frequencies above 10 Hz. This is accompanied by a slight and unexpected contribution to the covariance at these frequencies.

Figure 23B shows the co-spectral information of the along wind and cross wind component. As expected the coherence is very small over the whole frequency range, and co-spectrum and phase spectrum are not well-defined.

For the same period Figure 23C shows the crosswind co-spectrum with the vertical wind. As expected the co-spectrum is small, and again a slight extra coherence is observed around and above 10 Hz.

Looking at the high frequency part of the power spectra in Figure 23A-C we see that V and W have the same values, whereas U is smaller. This is related to the theoretical 4/3 ratio for iso-tropic turbulence, and it is a positive indicator for the quality of the turbulence measurements. The ratios are better seen in the logarithmically scaled power spectra in Figure 23E. In the frequency range 2-5 Hz the V and W spectra are equal. In the same frequency range the ratio between W and U varies between 5/4 and 4/3.

Figure 23D shows the temperature flux co-spectrum. Here we see a deviating signal in T already from frequencies below 1 Hz. As sonic temperature is more sensitive to changes in pathlength of the transducer pairs, the vibration problem shows up much clearer in the temperature signal. We see that coherence with W does not go to zero at high frequencies, and the phase start to deviate from 0.5, for this case with negative temperature flux. The contribution to the flux is so large that the co-spectrum changes sign at 2 Hz.

We now turn to FL48. Figure 24A-E displays for the same period the co-spectra at FL48. Figure 24A shows the forward stress co-spectral information. Here we see an increasing coherence from 5 Hz on without a change in phase. Which suggests that the effect of vibration on W and U are in anti-phase. As seen in the co-spectrum this results in an extra negative contribution to the stress.

The along-wind cross-wind co-spectrum in Figure 24B shows that the vibration dominates from 5 Hz onward, and the effects on U and V are in phase.

For the same period Figure 24C shows the crosswind co-spectrum with the vertical wind. As expected the co-spectrum is small, and again an extra coherence is observed around and above 10 Hz.

Ratios of the power spectra can be judged from the logarithmically scaled power spectra in Figure 24D. As in FL47 case (Figure 23E) in the frequency range 2-5 Hz the V and W spectra are equal. In the same frequency range the ratio between W and U varies between 5/4 and 4/3.

The temperature co-spectrum as displayed in Figure 24D, shows deviating behaviour at high frequencies, which is less strong than at FL47, but coherence at high frequency is higher. As the phase of the vibration effect on W and T are out of phase (1/4 of a circle) no extra contribution to the co-spectrum is observed in this case.

Figure 25 through Figure 29 show the co-spectral information for the along wind stress for five other periods in the windy episode between 04-14 Mar-2019 for both FL47 and FL48. Here we see that deviations due to the vibration effect is more the rule than the exception under these strong wind

situations. In conclusion, although inclinometer readings suggest an improvement of the stability of the platforms FL47 and FL48, still significant deterioration of the stress signal occurs at both platforms due to vibrations in the sonic frame. Finally Figure 30 shows that even under low wind speed conditions unexpected enhancement of the co-spectra may occur at the high frequency side. At this stage it is unclear what the cause is in this case.

Useful stress observations can only be expected if an adequate correction procedure can be found.

## **8 A method to correct EC stress observations for sonic vibration**

### **8.1 Introduction**

First a small resumé of findings based on earlier data, which are confirmed above for the new observation period 2018-2019. Missing samples in the raw data stream of 55 Hz were identified in particular during strong wind situations. Especially for the calculation of spectra this is problematic. A resampling procedure has been developed to overcome this problem. Here we use resampling from 55 Hz to 50 and 20 Hz respectively.

High frequency vibrations have been identified to disturb the eddy-covariance stress observations at FL47 and FL48 especially at high wind speeds. An attempt has been made to decrease the intensity of this vibrations at the two locations by stabilizing the mechanical configuration on which the sonic is mounted. This was found to have a positive effect. Also the new platforms operational since 2018 appear to be more stable, which may help to improve the performance of the sonic anemometers.

It could well be that vibration is one of the causes of the missing of raw data samples. But this is difficult to prove because high winds, rain, and vibrations often occur simultaneously.

It is found that the vibrations are limited to frequencies above 1 Hz. A spectral method has been developed to exclude the high frequency part of the spectrum from the calculation of the variances  $\langle uu \rangle$  and  $\langle ww \rangle$ , and of the co-variance  $\langle uw \rangle$ . Standard spectral functions are fitted to the observed (co-) spectra in the low-frequency range. The high frequency part of this fitted spectral functions are then used to estimate the true contribution to the turbulent (co-) variance in this high frequency range instead of using the observed contribution contaminated by the vibrations.

We developed and applied the method on the basis of a previous measurement period (2016-2017). For this we took 20-nov-2016, a day with strong winds up to 20 m/s. Figure 31 shows the 10 minute mean meteorological conditions during this day, and (first panel) the average sampling rates per 10 minute intervals for both FL47 and FL48. We see that both FL47 and FL48 suffer from sample loss in the period where wind speed is around 15 m/s or more. This panel also suggests that rain is of less importance for sample loss, as rain rates are low after 12:00 UTC, whereas sample loss continuous. Note however, that rain rate is derived from the rain radar and susceptible to uncertainties.

### **8.2 Check of spectral information in relation to resampling**

To get some further confidence in the resampling procedure we compare spectra based on 50 Hz and 20 Hz resampling. Figure 32 shows for the period 16:00-18:00 UTC full spectral information both for the 50 Hz and for the 20 Hz resampled time series. This is a period for which only a small number of data are missing.

The segment size is chosen the same for the 20 and 50 Hz spectra. To obtain optimal statistics half segment overlap is applied.  $M=1024$  in the graph refers to the half segment size. Thus there are 2048 samples in a segment. This also means that segment length for 20 Hz is 2.5 times longer (in seconds) than for 50 Hz. The Nyquist frequencies of 25 Hz and 10 Hz are nicely shown. Also seen is the aliasing because the raw data are not low-pass filtered. This is best seen for the 20 Hz WS48 spectrum. On the low frequency side the spectra are nicely on top of each other. However the 20 Hz data show some more variation. This is due to the smaller number of segments that are available for the 20 Hz in the given time period. Another consequence of the different segment time length is that the lowest frequency for which a spectral value is obtained is also 2.5 times lower for the 20 Hz spectrum. This

gives for the spectral point with the lowest frequency for the 20 Hz time series:  $2048/20 \text{ sec} = 0.00976 \text{ Hz}$ , and for the 50 Hz time series:  $2048/50 = 0.0244 \text{ Hz}$ .

These spectra are quite well behaved although some small effects of vibrations are seen at the high frequency side of the spectra. Figure 33 shows the same information but now for the period 06:00-08:00 UTC. Here strong effects are seen due to vibrations that deform the spectra for frequencies above 1 Hz.

The differences observed between the 20 and 50 Hz co-spectra for both periods are in line with what the larger aliasing effects that can be expected for the 20 Hz case.

### 8.3 Correction for the influence of vibrations.

We observe in Figure 32 and Figure 33 that the vibrations have frequencies ( $f$ ) which are on the right (high frequency) side of the spectral peaks, at least for  $\langle uu \rangle$  and  $\langle uw \rangle$ . This means that most of the vibrational energy is in the so-called inertial sub range. For  $\langle ww \rangle$  the contribution of vibration starts already at the spectral peak.

The normalized frequency is defined as  $n = fz/U$ , where  $z$  is measuring height and  $U$  is wind speed at this height. The spectral inertial subrange starts at normalized frequencies well above  $n = 1$ .

Kaimal et al. (1972) describe the scaling behaviour of (co-)spectra of turbulence in the surface layer. We use their normalized modelled (co-)spectra and fit them with a multiplication factor to the observed level of the co-spectra in the range of normalized frequencies  $n=[0.5:1.0]$ , the highest frequency range supposed not to be effected by the vibration effect. In fact we use Kaimal spectra but include the effect of aliasing at the Nyquist frequency, as the observed raw data are not filtered.

We aim at a procedure that is able to correct for each 10 minute covariance. To this end we use in the spectral calculation a small segment size to obtain spectral estimates with small uncertainty. Note that the variance in an estimated spectral value scales inversely proportional to the number of segments used. For 50 Hz we go to a half segment size of 256 samples ( $10s = 0.1 \text{ Hz}$ ), and for 20 Hz 128 samples ( $13s = 0.08 \text{ Hz}$ ) which is still long enough to cover all the relevant frequencies for this exercise.

We calculate the observed contribution to the co-variance for  $n > 1$  including the effect of vibration, and we calculate the contribution that we expect given the Kaimal spectra which are fitted on the spectral region at the low frequency side of the inertial subrange,  $n = [0.5:1.0]$ . The difference between the two can then be subtracted from the uncorrected observed co-variance to obtain a corrected co-variance.

Figure 34 and Figure 35 show the observed and the fitted spectra for a 10 minute interval with little vibration and an interval with strong vibration respectively. So we expect a small correction in the first case and a large correction in the second case. In the next section corrections will be shown for all 10 minute intervals in this day, and these two 10 minute periods will be highlighted.

### 8.4 All corrections

Three corrections are applied to the 10 minute stress data. They are in this order:

1. Vibration correction (first, because this signal has nothing to do with turbulence)
2. Tilt correction ( to arrive at the true vertical momentum flux)
3. Low frequency loss due to finite (10 minute) time series used to calculate the turbulent stress

Figure 36 shows comparisons of the friction velocity after each correction step. Panel A shows the effect of the vibration correction. The effect is in general a decrease in friction velocity up to 20%.

Note that the two data points corresponding to the time intervals analysed in the previous chapter are black encircled. The upper point corresponds to the no-vibration case (15:30-15:40 UTC). This shows that the estimate of the contribution of frequencies above  $n=1$  based on Kaimal spectra is accurate for this case where only turbulence and no vibration is present. The lower encircled point corresponds to the strong vibration case (06:10-06:20 UTC). Here a correction of more than 20% is calculated.

Panel B shows the effect of the tilt correction. This correction is also substantial. The lower branch is the morning period and the upper branch the afternoon period when the wind has veered after the passage of the cold front. The tilt correction takes into account the cross talk between the forward horizontal wind component  $U$  and the vertical wind speed  $W$ . As the water surface is aerodynamically relatively smooth,  $\langle uu \rangle$  is much larger than  $\langle uw \rangle$  and thus a small tilt angle already results in a substantial tilt correction. It is at the low frequency side that  $U$  has much larger variations than  $W$ , whereas in the inertial subrange these variations have approximately the same magnitude.

Panel C shows the effect of finite time series length. This effect is estimated on the bases of, again, the Kaimal spectra. As conditions are close to neutral stability, and winds are strong this effect is small. For low wind and convective conditions as more often encountered over land this correction can be significant.

Panel D will be discussed in the next section.

### 8.5 The drag relation on the basis of fully corrected EC-stress data

Having performed all the relevant corrections we now plot the friction velocity as function of wind speed (FF48) in Figure 37 To reduce scatter we average the 10 minute values to 30 minute values. Shown are the fully corrected friction velocity (UST484) and the original uncorrected friction velocity (UST48). Also shown is the expected relation based on the Charnock relation for surface roughness, and neutral stability. Two curves are shown, one with a Charnock coefficient ( $\alpha_c$ ) of 0.018 and one with 0.032. Also shown is the linear relation obtained when assuming a constant surface roughness length of 1.8 mm. This is the value we get from the Charnock relation with  $\alpha_c = 0.018$  at  $u^* = 1$  m/s. and  $FF(z=10m) = 21.5$  m/s. Clearly the data show the effect of the increasing sea surface roughness with wind speed/friction velocity. The data fall reasonably on the Charnock curves, although the observed relation appears to be steeper, and especially at the highest wind speeds some extra scatter is observed.

Interestingly the uncorrected data (UST48) lie systematically lower in this scatter plot, but also the scatter is larger. This latter observation gives some extra confidence in the correctness and usefulness of the corrections applied.

It is noted that the scatter in the corrected data increases at the highest wind speeds of 15 m/s. This may hint at some remaining uncertainties in the vibration correction which are most strongly present at these high wind speeds. Note that for the highest wind speeds of this day no reasonable vibration correction could be done, due to too much missing data.

As a last remark we return to Figure 36 panel D. Here we have taken into account the effect of atmospheric stability on the friction velocity. This is derived from the observed wind speed, the Charnock surface roughness parameterization, and the observed temperature difference between the water and the air. Here we have used the flux-profile relations from Beljaars and Holtslag (1991). As temperature of the air is larger than that of the water for this day, up to 4 °C, the atmosphere is stably stratified. This results into a smaller friction velocity then would be obtained at neutral stability. UST484 is then the friction velocity we would have had with neutral stratification, and this can then be compared to the Charnock based curves for neutral stratification in Figure 37. The effect however, is small, much smaller than the influence of vibration and tilt.

## 9 Results for the Nov 2018 – Jun 2019 period

### 9.1 Magnitude of the various corrections performed to the stress

The correction method applied to the stress data is described in Section 8.4. In Figure 38 and Figure 39 the influence of the successive corrections (vibration, tilt, low frequency, and stability) are shown for FL47 and FL48 respectively for the period 04-17 Mar 2019. It shows that vibration and tilt give rise to the largest corrections, of typically 10 to 20%.

### 9.2 Comparison between 20 Hz and 50 Hz based data.

As the vibration correction procedure is a new and rather complex procedure, any further checks to improve reliability are welcome. To further investigate the reliability of this vibration correction procedure we compare the stress observations derived from the 20 Hz resampled data and of the 50 Hz resampled data as described in section 4.2. All reduced parameters have been derived separately from these two time series, including the spectral vibration corrections.

Figure 40 and Figure 41 show the comparison of stress vibration corrections based on 20 Hz and 50 Hz resampled data for FL47 and FL48 respectively. Panel A compares the uncorrected stress derived from the 20 Hz and 50 Hz resampled data. Differences are very small as may be expected given the dense coverage of samples relative to the integral time scale of the turbulence as discussed in Section 4.2. Panel B compares the corrected stress derived from the 20 Hz and 50 Hz resampled data. Here the differences are slightly larger.

Panel C and D compare uncorrected and corrected stress values for the 20 Hz resampled data (C) and for the 50 Hz resampled data (D). We observe that there are two branches of corrections both for 20 Hz as for 50 Hz. A narrow band with small negative corrections, and a more broad band with larger positive corrections. For FL48 the corrections in the narrow band are smaller in magnitude than for the FL47 case, and the positive corrections in the broadband are larger in magnitude. At this stage it is unclear what causes the two branches.

Zooming in, panel E and F compare the high frequency contributions to the stress for 20 Hz and 50 Hz. Observed, with vibration in panel E, and modelled, without vibration in Panel F. It is clearly seen that vibrations may add significantly to the observed uncorrected stress, whereas modelled values are an order of magnitude smaller.

Finally panel G compares the correction for going from uncorrected to corrected data for 20 Hz and 50 Hz (by subtraction). Ideally the corrections should be the same for both 20 Hz and 50 Hz resampled data. Here we see that the corrections are slightly larger in magnitude for 50 Hz as compared to 20 Hz. Differences however are relatively small as is shown in perspective of the magnitude of the stress in panel B. This gives some further confidence in the validity of the vibration correction method applied in this study.

### 9.3 The drag relations for FL47 and FL48

Figure 42 shows the relation between wind speed and friction velocity. Here data are taken for the high wind period of 20190304-20190317. A clear curvature is observed, as may be expected from a Charnock-like relation between friction velocity and surface roughness over water. The two lines are for Charnock parameter  $\alpha = 0.018$  and  $0.032$  respectively. In the high wind speed range the  $\alpha = 0.032$  line seems to fit better, whereas in the low wind speed range the  $\alpha = 0.018$  line fits better. This indicates a surface roughness increase with wind speed stronger than Charnock. Especially in the low wind speed range the FL48 values are larger than for FL47, and the FL48 values there seems to follow the Charnock relation better. Note that FL47 is the location with the best fetch. Also shown in the same figure are uncorrected data. This indicates that the corrections are significant and that accurate corrections are essential for judging the precise drag relations.

Figure 43 shows the drag relation but now for the full period 201811-201906. Here only fully corrected data are shown. A clear narrow band of data is observed which show a nice functional relationship, although, as in Figure 42, not in full concord with the two Charnock relations shown in

the figure. But also outliers are observed. We investigated a few (8) of these outliers (with positive deviation in the friction velocity) and found that all of them are related to non-stationary wind conditions within the 30 minutes used to calculate the eddy-correlation momentum flux. For each location we show one example. Figure 44 shows 10 min. wind speed and stresses for 20190102 at FL47. The wind speed gradually decreases over the day from 13 m/s to 7 m/s. In the period 0400-0800 UTC a few data points show large stresses which are not accompanied by increased wind speeds. In Figure 45 we zoom in at one of such occasions, the 10 min. period starting at 0700 UTC. High resolution data of horizontal and vertical wind speed are displayed in the upper panels respectively. In the lower panels the contributions in terms of Reynolds decomposition  $(u(t)-\langle u \rangle)(w(t)-\langle w \rangle)$  are displayed. The lower right panel is low-pass filtered with a block filter of 10 sec., clearly showing the variations in flux contributions over time. In this case the wind speed is far from stationary, a prerequisite for a meaningful interpretation of the flux value obtained over this 10 min. period. In Figure 46 we look at the day 20190108 at FL48. Again a number of short periods with exceptional high stress values are found, given that the wind speed is quite steady over time. Figure 47 zooms in at the 10 min. period starting at 1750 UTC. As in the previous case a quite irregular behaviour is observed, here especially around  $t=200$  s, which gives rise to an exception high flux contribution.

This analysis shows that the outliers in the drag relation plots stems from non-stationary behaviour of the wind, and not from errors introduced by the vibration correction procedure.

#### 9.4 The relation between stress and standard deviation of the horizontal wind

Surface roughness, wind speed, and friction velocity ( $u_*$ ) are intimately connected through the logarithmic wind profile relation. Over land the variability of the wind in terms of gusts and standard deviation ( $\sigma_U$ ) has also been shown to depend on the surface roughness (Wieringa, 1986, Beljaars 1987, Verkaik et al., 2000). As standard deviation is a more robust statistical measure for the variability of the horizontal wind than is gust, it is the preferred parameter for roughness characterisation provided this information is available. The two parameters  $\sigma_U$  and  $u_*$  are related through:

$$\frac{\sigma_U}{u_*} = 2.2 f\left(\frac{z}{L}, \frac{z}{z_i}\right)$$

Where  $z$  is measuring height,  $z_i$  is the atmospheric boundary layer height, and  $L$  is the Obukhov length. The function  $f(\cdot)$  is 1.0 for neutral condition ( $L \rightarrow \infty$ ) and the absence of an atmospheric boundary layer that is restrictive to the larger turbulent eddies. The value 2.2 is taken from Verkaik et al. (2000). As  $\sigma_U$  is dominated by larger eddies then is the case for  $u_*$  the estimate of roughness is expected to be representative for a relatively larger are, called regional scale roughness in contrast to local roughness respectively.

If the wave field over the seas and larger lakes are sufficiently homogeneous this difference between local and regional scale roughness becomes irrelevant. This opens the possibility to estimate the momentum transport from atmosphere to the water by means of  $\sigma_U$ . The advantage being that the observation of  $\sigma_U$  is much easier to perform then the direct observation of  $u_*$ , especially under the harsh conditions during storm and rain.

In Figure 48 the relation between  $\sigma_U$  and  $u_*$  is shown for the two locations FL47 and FL48. Data are selected on wind speeds larger than 5 m/s to avoid conditions far from neutrality. At stronger winds, which corresponds to the right side of the scatter diagram, the effect of the ABL will decrease, as it may be very high, or the ABL may be even absence in the sense of an absence of relevant temperature gradients in the lowest few kilometres of the atmosphere. In this case also the effect of the second argument in  $f$  will be small.

A slightly curved relation is observed, the ratio between  $\sigma_U$  and  $u_*$  decreases with increasing wind speed but stays well above 2.2 as is indicated by the line in the graph. At FL48 the standard deviations are slightly larger than at FL47. It is likely that this different behaviour is related to regional scale roughness differences at the location of FL48 close to the coast. This may be by the proximity of the land surface or by changes in the wave height going from the coast to the measurement location.

In Figure 49 for completeness the same relation is shown but now for the full period of 201811-201906.

## 10 Summary and conclusions

The correct measurement of the turbulent stress in the surface layer of the atmosphere is a complicated task. The more so if such measurements are to be performed over water during high wind conditions. In this experiment it took three storm seasons to refine the measurement set-up, and still the resulting observations suffered from serious problems. A time consuming analysis was undertaken to try to correct for these shortcomings in the observations. The shortcomings were 1) a loss of data rate during rainy and hard wind conditions, and 2) high frequency vibration of the sonic anemometer frame. The loss of data rate made spectral analysis problematic, and spectral analysis and processing was necessary to filter the effect of high frequency vibration. Both effects seem to occur preferably at high wind speeds although occasionally also vibration issues were found at much lower wind speeds.

There is an indication that sonic data loss is related to an internal check in the Thies 3D sonic anemometer. However the instrument does not seem to give status information that show data loss.

The irregular loss of data was tackled by resampling the 55Hz data at a lower rate. In our case resampling rates of 50 and 20 Hz were used. As may be expected no significant differences were found between fluxes calculated on the basis of these two different resampled time series.

A spectral method was developed to correct for the vibrational effects on the turbulent stress. Also here it was shown that the results did not differ significantly between the two resampled time series.

Various corrections were applied to the stress data. The largest corrections are the vibrational correction and the streamline tilt corrections.

The observed drag coefficient at the two locations follow more or less the Charnock relation. At least in the sense that the drag coefficient increases with wind speed. However, at low wind speeds drag seems to be smaller and at high wind speeds larger than obtained from the Charnock relation with  $\alpha = 0.018$ . Slight differences are observed between FL47 and FL48. The results also show that the accuracy with which the corrections for tilt and vibration are determined is very relevant for the accuracy with which the best-fit Charnock constant can be determined from the observations.

Outliers in stress observations occur. For a number of cases it was shown that these deviating behaviour is not related to the vibration correction, but to non-stationary behaviour of the wind speeds during the time frame for which the stress is calculated. Stationarity is one of the assumptions behind the eddy-correlation method for flux determination.

Drag coefficients can also be determined from the standard deviation of the horizontal wind. This is an indirect method which has been applied over land surfaces. The method needs a calibration by a direct observational method. The advantage is that such observations are more easily to perform than turbulent stress measurements. In this study a connection is made with the turbulent stress observations. It is shown that a strong relation exists between observed friction velocity and standard deviation of the horizontal wind. The coefficient that relates the two seems to be larger than the one normally used over land surfaces (2.2).

This report describes the technical aspects of obtaining a reliable dataset of stress over the Lake IJssel. Especially the high wind speed cases are of interest for the purpose of these observations. One technical aspect not yet covered is to see whether the 20 Hz based stress data indeed gives more observations at highest wind speeds. This is the condition that data rate failure happens the most and stress data based on the 50 Hz dataset may occasionally be missing.

Another technical aspect is whether movements of the platforms are dependent on wind direction. And whether the strength of this movement is coupled to vibration issues.

A first attempt has been made to analyze the usefulness of the standard deviation of the horizontal wind as a proxy for the friction velocity. A further analysis on wind direction dependence of the results will be interesting for the interpretation of these results. Also analyzing the relation between standard deviation of the vertical wind and friction velocity may be interesting. This then should be

accompanied by a judgment of the correctness of the vibration correction for the standard deviation of the vertical wind.

The current data allow for the analysis of sensible heat flux and the possibility to derive this parameter from wind speed and temperature difference between water and air. Note that the sonic temperature is significantly affected by frame vibration, and currently the temperature flux data are not corrected. However, such an analysis could also be performed on the basis of conditions with low wind speed where vibration effects are expected to be smaller. As a byproduct a reliable atmospheric stability parameter (Obukhov length) can be derived.

The Cd relations shown in this report can be further analyzed as function of wind speed. This could shed light on the difference between the coastal (FL48) and mid Lake (FL47) location.

Further analysis can be done of the stress observations in relation with wave parameters like Hm0, wave steepness, and wave age. In this context also a comparison with wave independent drag formulas would be interesting.

## 11 References

- Beljaars, A.C.M. (1987). *On the memory of wind standard deviation for upstream roughness*. Bound.-Layer Meteorol., **38**, 95–101.
- Beljaars, A.C.M. and Holtslag A.A.M. (1991). *Flux parameterization over land surfaces for atmospheric models*. J. Appl. Meteorol., **30**, 327-341.
- Bosveld, F.C. and A.C.M. Beljaars (2001), *The impact of finite sampling rate on eddy-covariance fluxes*. Agricultural and Forest Meteorol., **109**, 39-45.
- Kaimal, J.C., Wyngaard, J.C., Izumi, Y., Cote', O.R. (1972). *Spectral characteristics of surface-layer turbulence*. Quart. J. Roy. Meteorol. Soc., **98**, 563–589.
- Lee, X., Massman, W., and Law, B. (2004). *Hand book of micrometeorology – A guide for surface flux measurement and analysis*. Kluwer Academic Publisher, Dordrecht/Boston/London, pp250.
- Schotanus P., Nieuwstadt, F.T.M., and De Bruin H.A.R. (1983). *Temperature-Measurement with a Sonic Anemometer and its application to heat and moisture fluxes*. Bound.-Layer Meteorol., **26**, 81-93.
- Verkaik J.W. (2000). *Evaluation of Two Gustiness Models for Exposure Correction Calculations*. J. Appl. Meteorol., **39**, 1613-1626.
- Wieringa, J. (1986). *Roughness-dependent geographical interpolation of surface wind speed averages*. Quart. J. Roy. Meteorol. Soc., **112**, 867–889.
- Wyngaard, J.C. (1981). *The Effects of Probe-Induced Flow Distortion on Atmospheric Turbulence Measurements*. J. Appl. Meteorol., **20**, 784-794.

## 12 Acknowledgement

I would like to thank the following persons who have helped over time with this project. Hans Miedema, Andrea Jansen and Marco Peters (RWS) for providing the sonic data and technical meta data of the observations at Lake IJssel. Pieter Dekker (Xi) for providing the standard data from FL47 and FL48. Jan-Willem Schoonderwoerd (KNMI) for advises on improving the supporting construction of the sonic anemometers. Hidde Leijnse and Aart Overeem (KNMI) for providing weather radar based precipitation estimates for Lake IJssel. Marcel Bottema (RWS) for discussing directions of the project, and carefully commenting on earlier versions of this manuscript. Andreas Sterl (KNMI) for carefully reading the final version of this report.

# 13 Figures

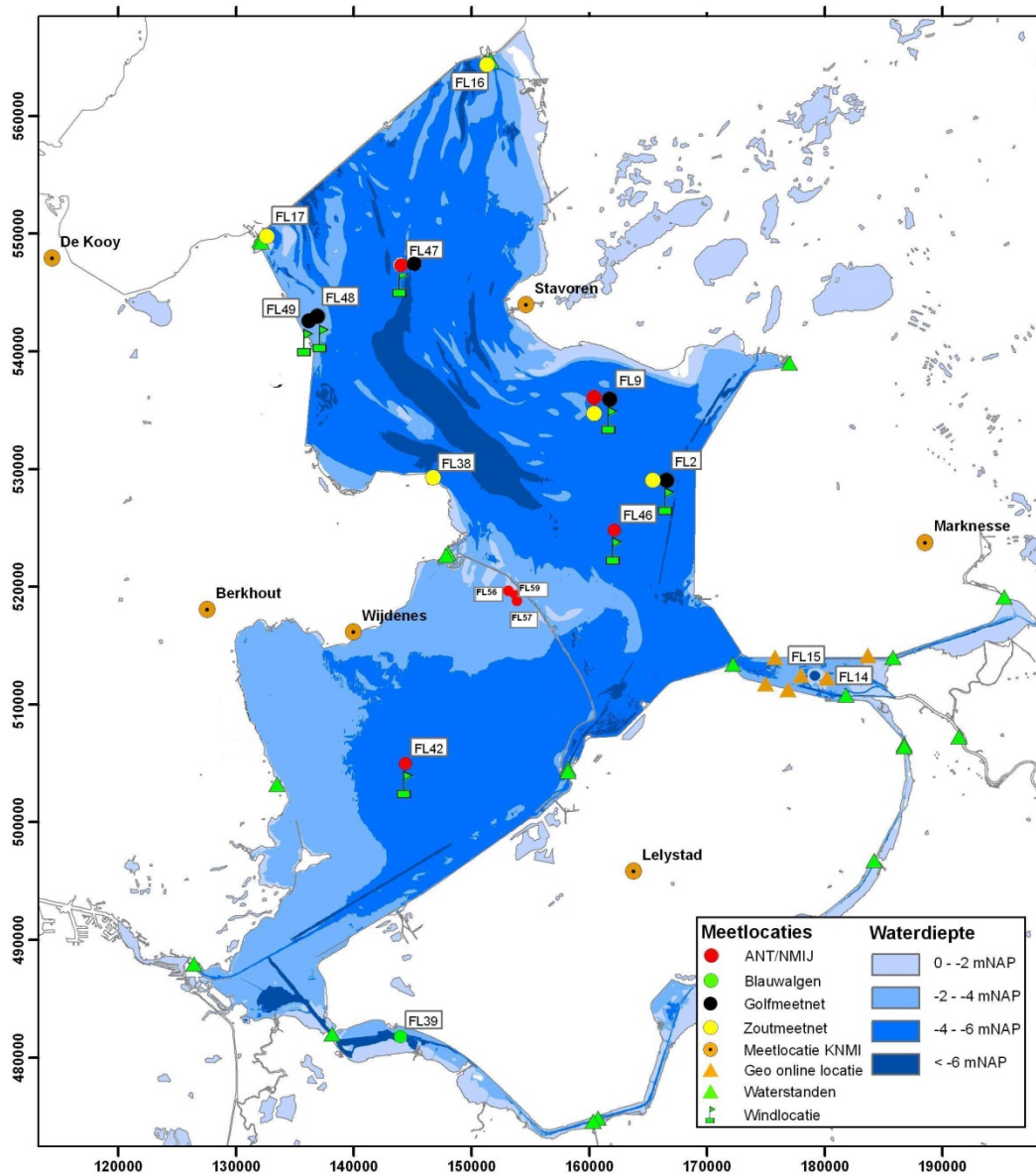
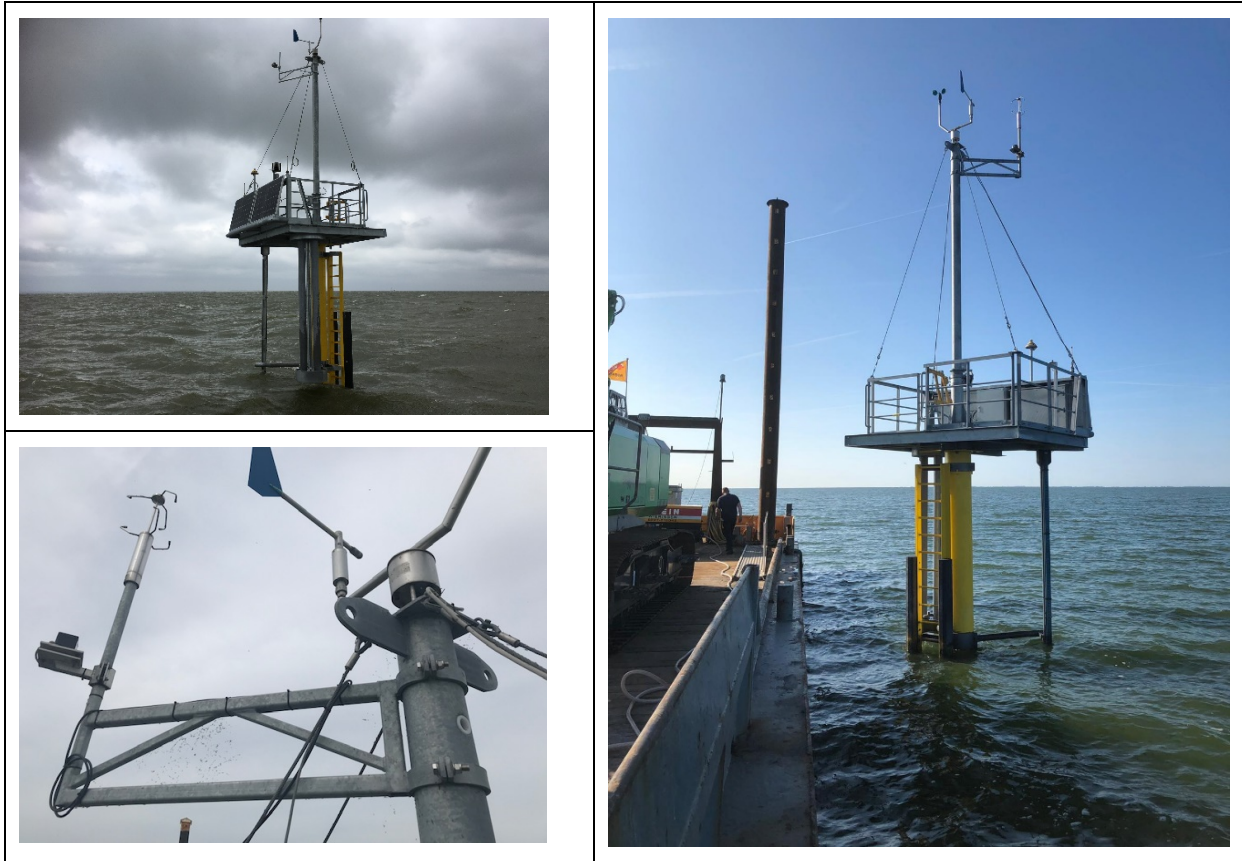


Figure 1 Map of Lake IJssel with positions of the various measuring locations including FL47 and FL48 at a line perpendicular to the West-Frisian coast.



**Figure 2 Measurement set-up for the period 201811 – 201906. (Upper left) Location FL47, (right) location FL48, and (Lower left) close-up of FL47. Inclinometers are positioned at the lower side of the sonic anemometer stem. Note that the upper left photo was taken after the sonic anemometer had been dismantled.**

201811-201906 IJSSELM3.B10

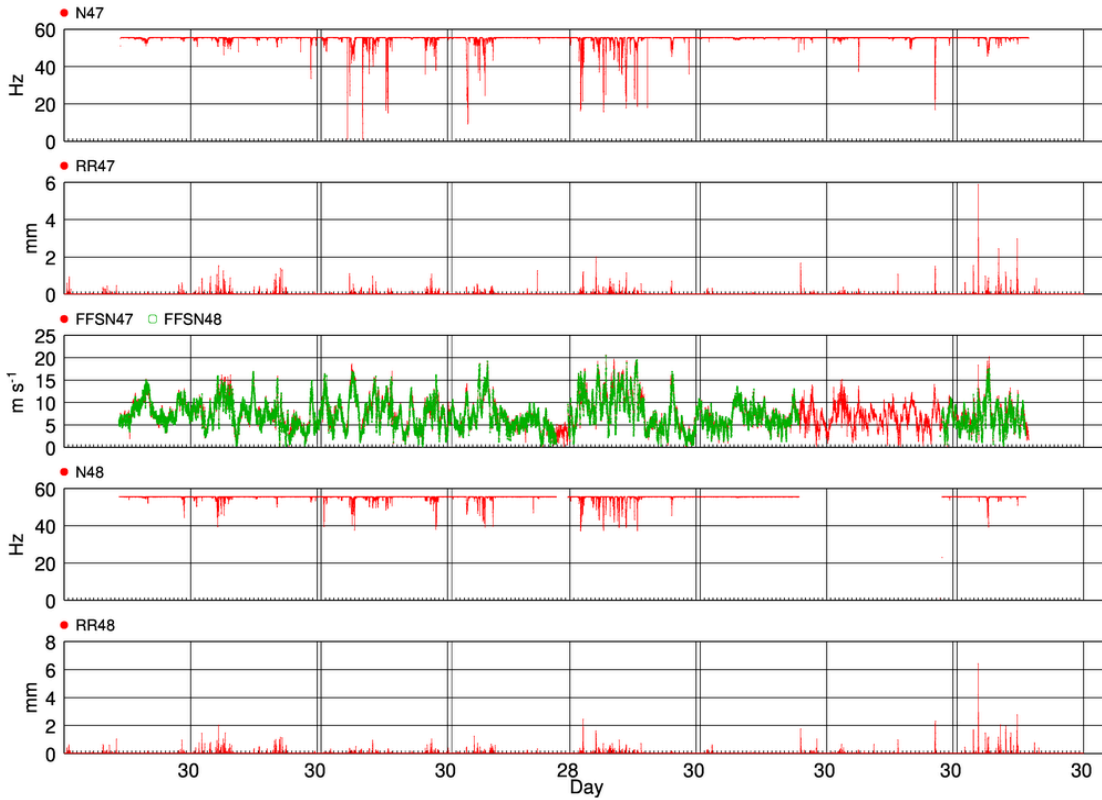


Figure 3 Average of sampling rate (N) for FL47 and FL48 for the full period Nov 2018 – Jun 2019. Nominal value is 55.4 Hz. Also displayed are the 10 minute average wind speeds (FFSN) and rain amounts (RR) in mm per 10 minutes.

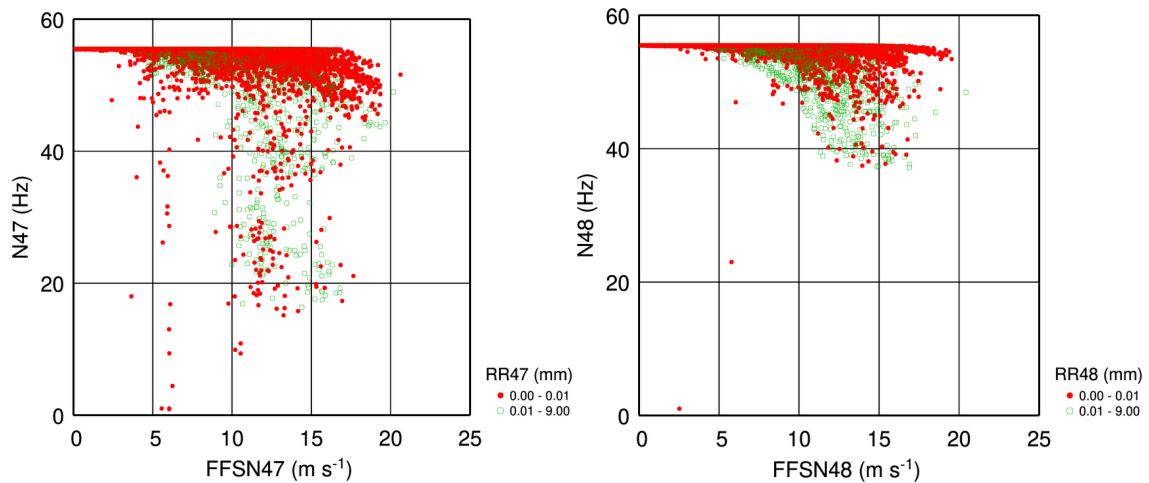


Figure 4 10 minute average sampling rate as function of wind speed, for the full period Nov 2018 – Jun 2019. Data are classified into no-rain (red dots) and rain (green circles). (Left panel) FL47 and (right panel) FL48.

IJSSELM3.B10

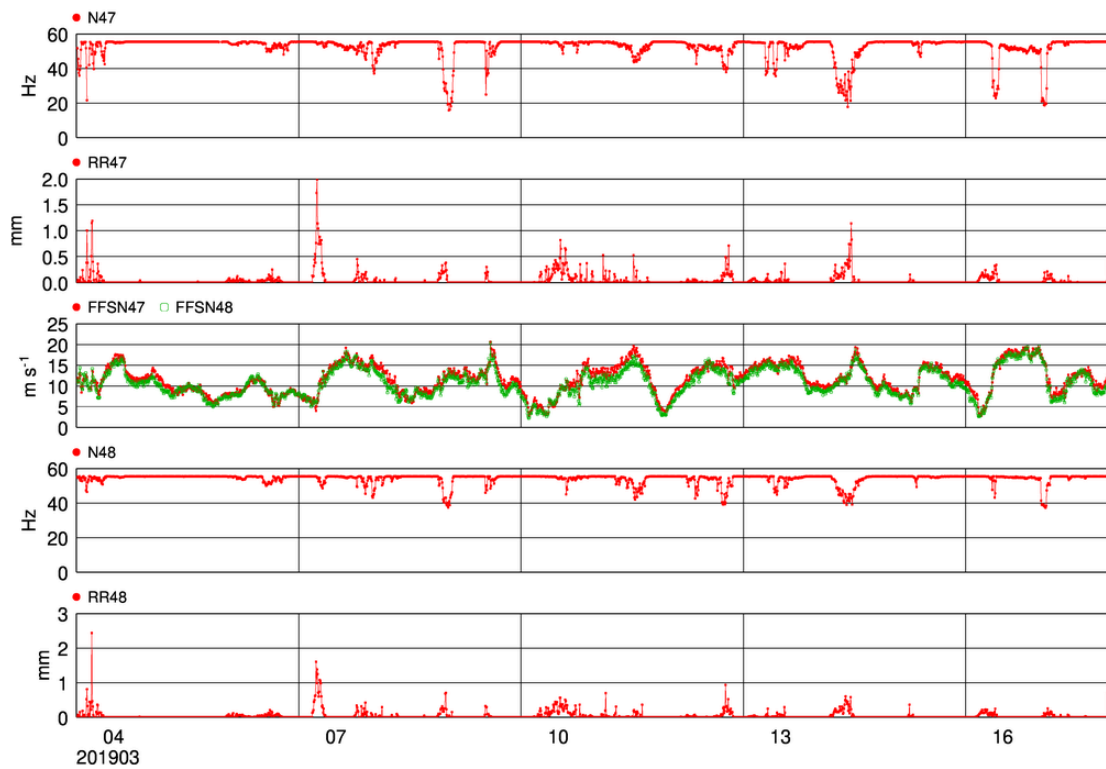
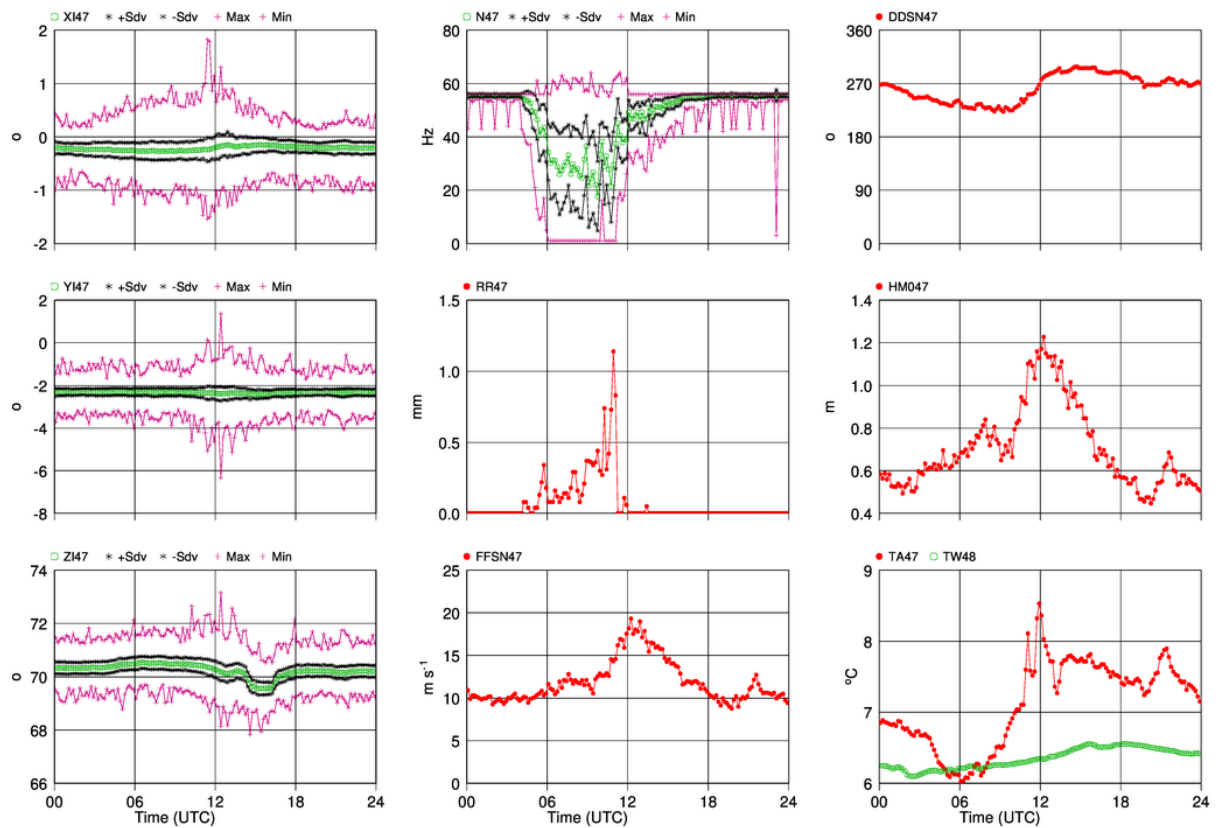


Figure 5 Average sampling rate for FL47 and FL48 for the period 20190304 – 20190316. Nominal value is 55.4 Hz. Also displayed is the 10 minute average wind speeds (FFSN) and rain amounts (RR) in mm per 10 minutes.

20190314 IJSSELM3.B10



**Figure 6** 10 minute values at FL47 for the strong wind case of 20190314. In the left column inclinometer readings (average  $\pm$ standard deviation, maximum and minimum value). In de middle column sampling rate (average  $\pm$ standard deviation, maximum and minimum value), rain amount, and wind speed. In the right column wind direction, significant wave height, and temperature of air and water. Water temperature is at FL48.

20190314 IJSSELM3.B10

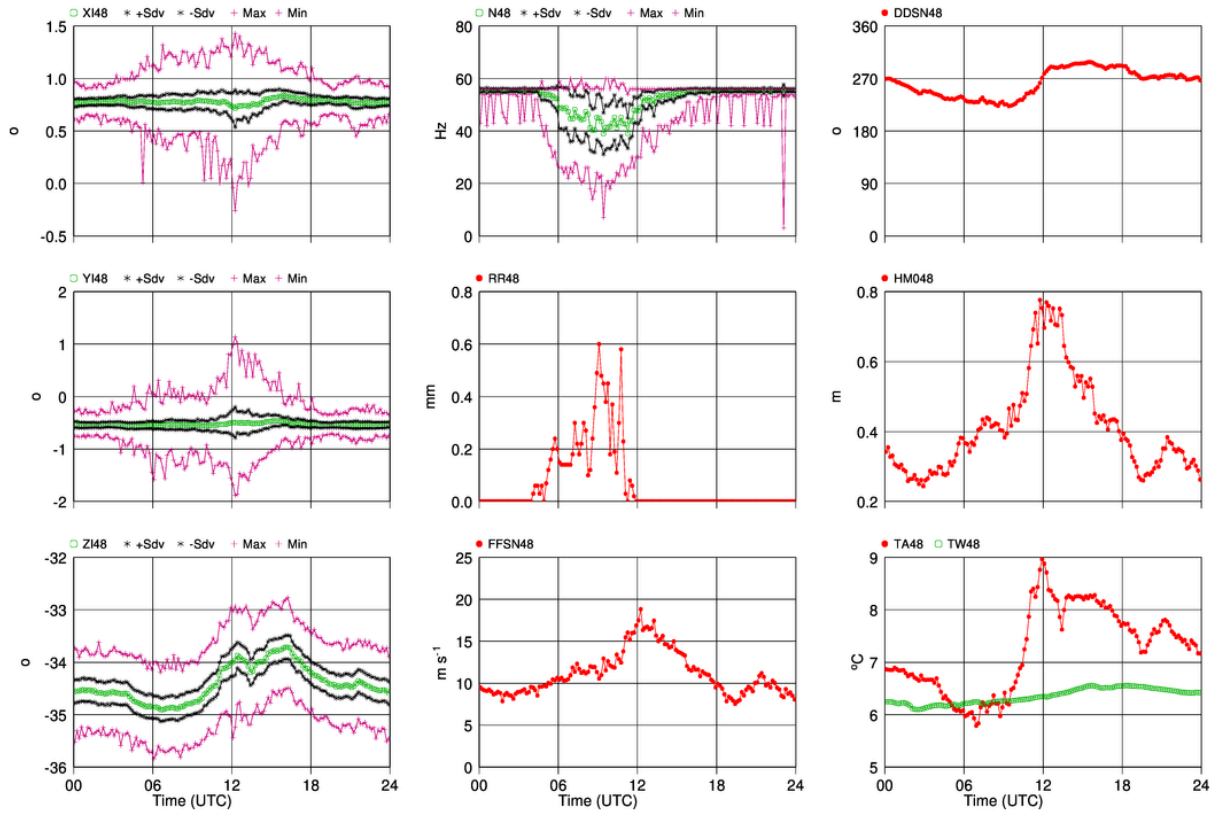


**Figure 7** 10 minute values at FL48 for the strong wind case of 20190314. In the left column inclinometer readings (average  $\pm$ standard deviation, maximum and minimum value). In de middle column sampling rate (average  $\pm$ standard deviation, maximum and minimum value), rain amount, and wind speed. In the right column wind direction, significant wave height, and temperature of air and water.

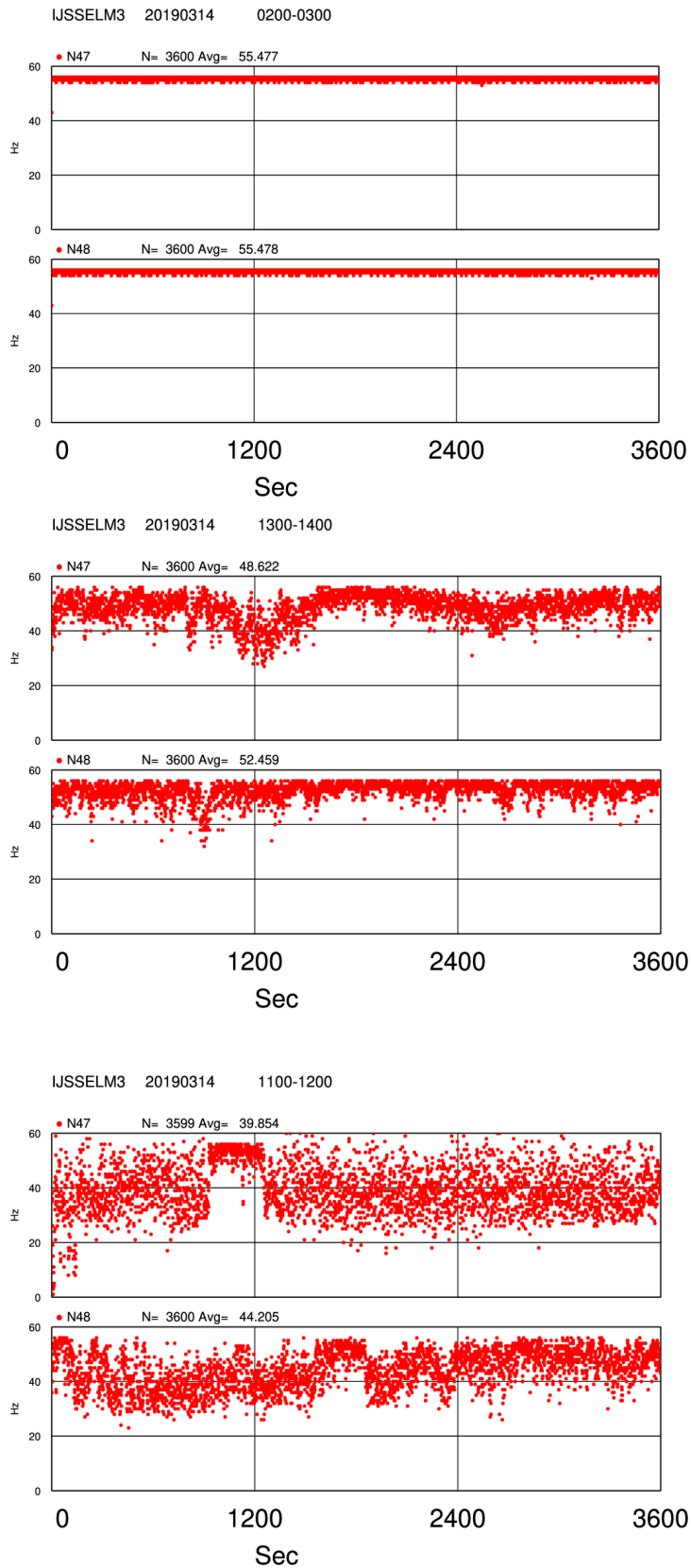


**Figure 8** Samples in each second for three periods of one hour during 20190309 at FL47 and FL48. (Top panel) 0200-0300 UTC, no data reduction, (Middle panel) 1300-1400 UTC, limited data reduction, and (Lower panel) 1100-1200 UTC, significant data reduction.

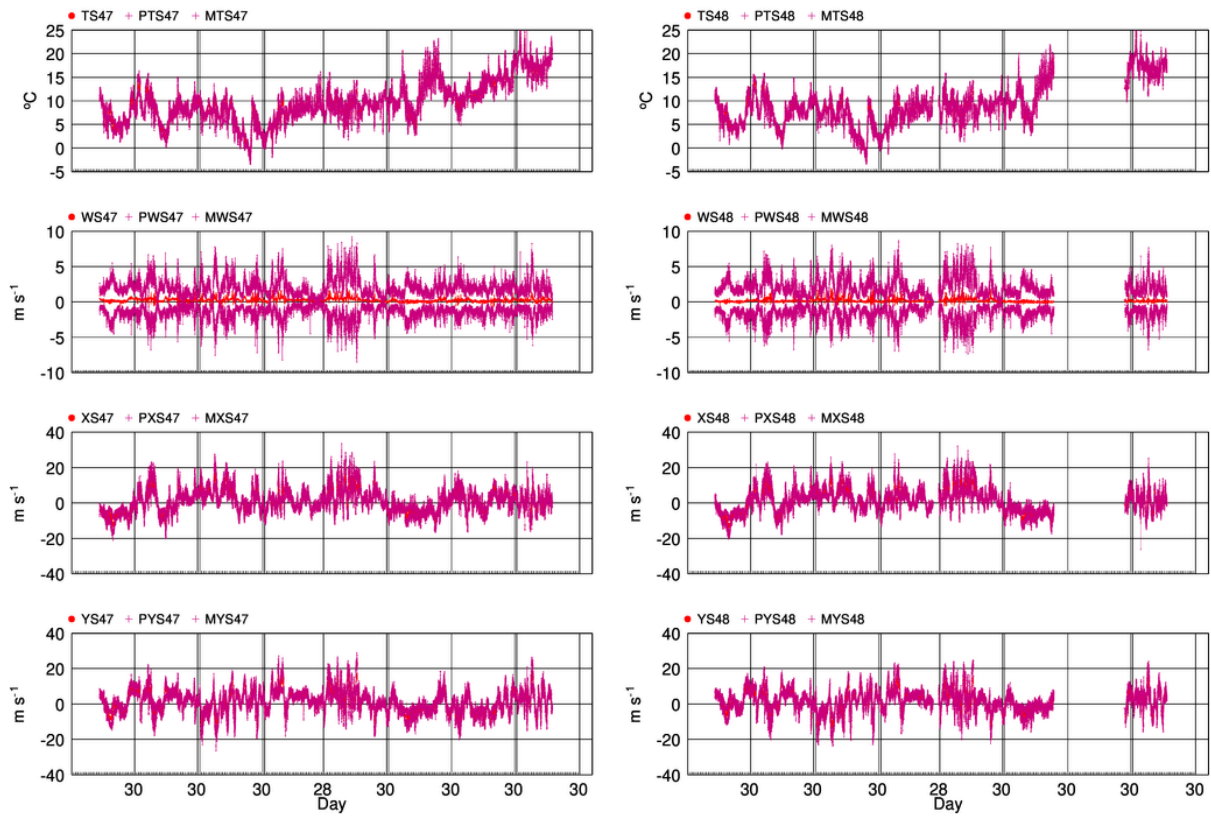


**Figure 9** Time series of temperature (TS), vertical wind speed (WS), forward wind speed (XS) and cross wind speed (YS) of the sonics at FL47 (Left panels) and FL48 (Right panels) for the period Nov 2018 - Jun 2019. Displayed are 10-min average (red dots and connecting lines), minimum and maximum (pink + signs with connecting lines). Note that often lines overlap and red dots may not be visible.

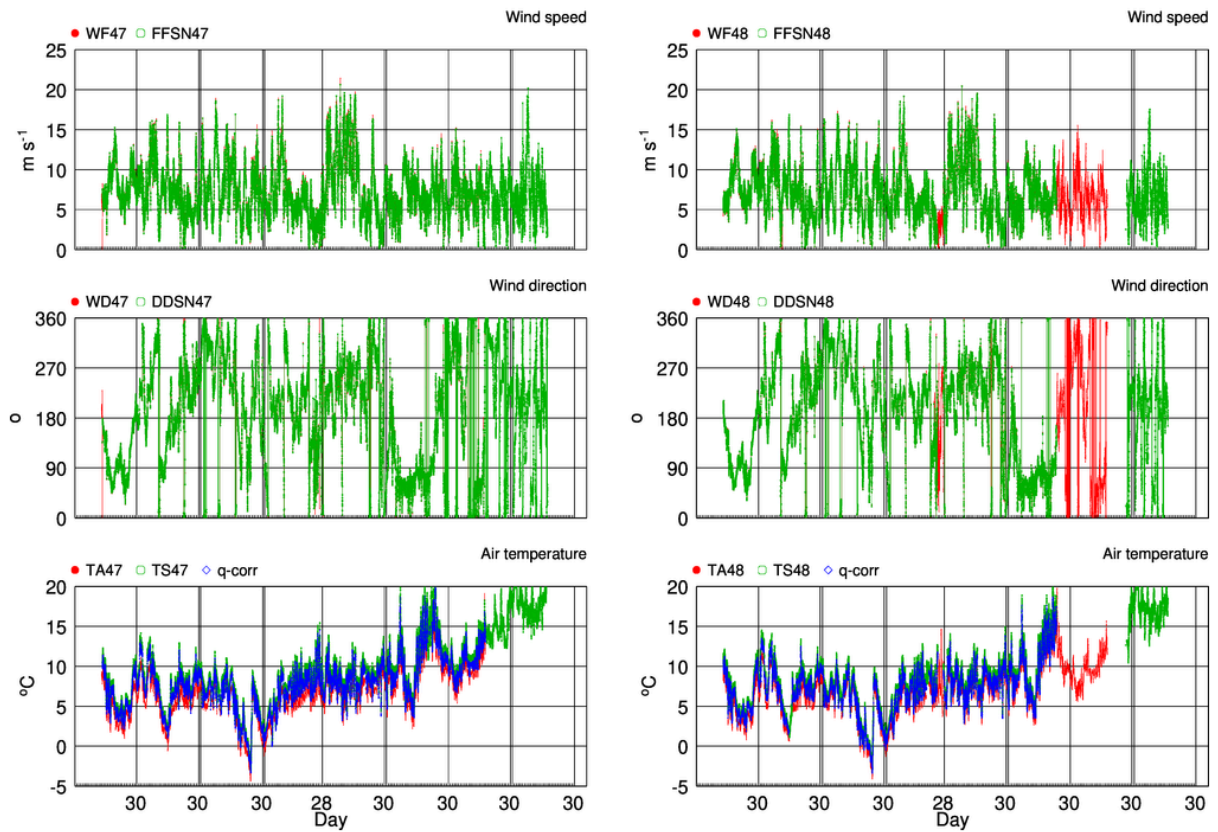


**Figure 10** Time series of wind speed (FF), wind direction (DD) and air temperature (TA) both from the sonic as from the standard observations at (Left Panels) FL47 and (Right Panels) FL48, for the period Nov 2018 – Jun 2019.

# IJSSELM3.B10

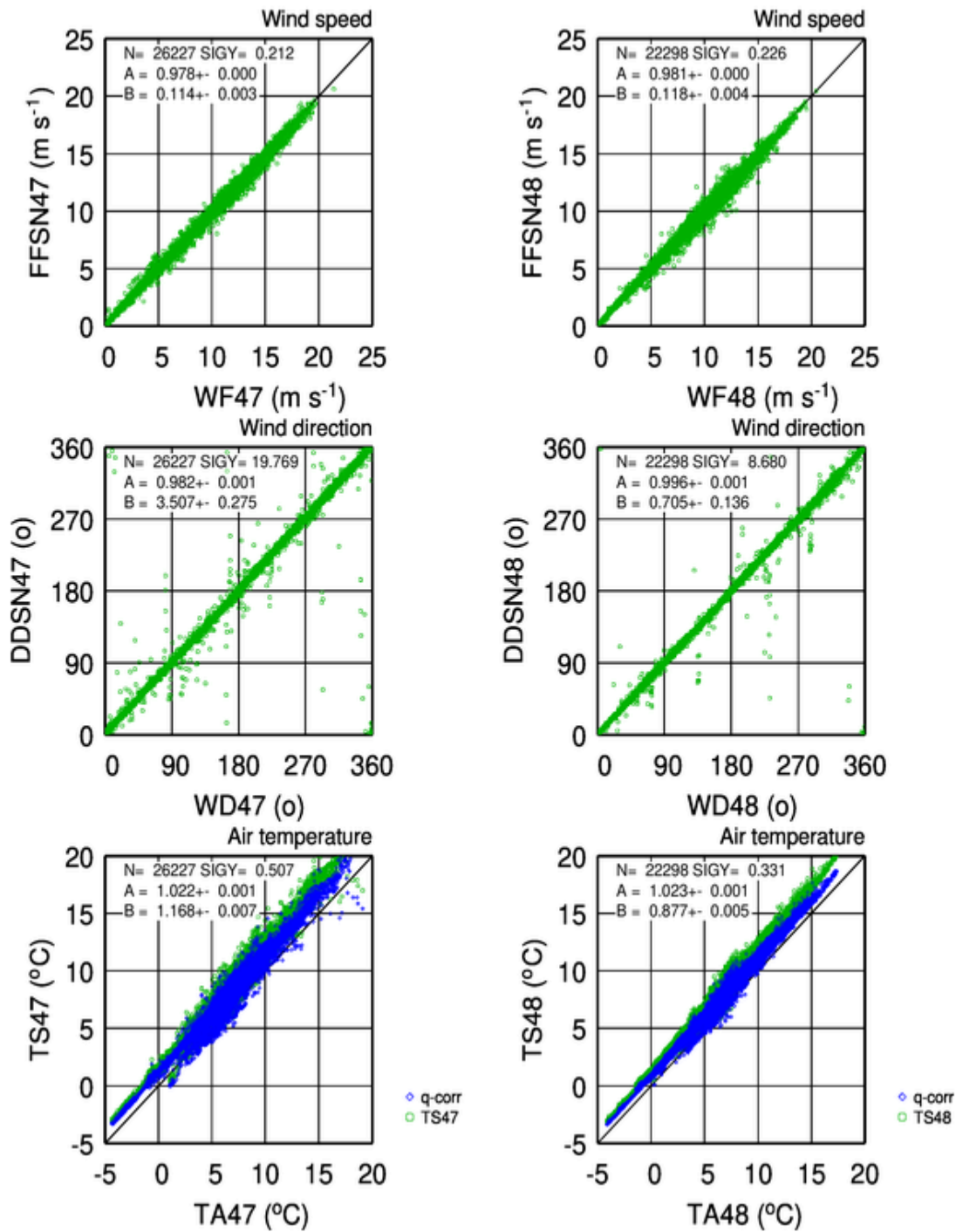
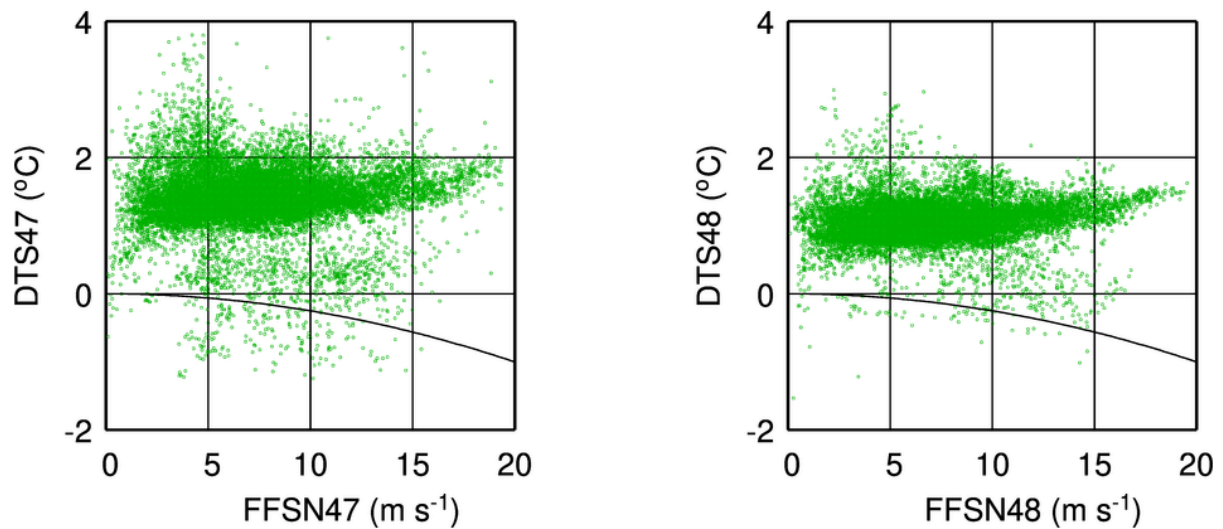


Figure 11 Scatter diagram of sonic wind speed (FFSN, upper panels), wind direction (DDSN, middle panels) and air temperature (TS, lower panels) as function of the corresponding parameters from the standard observations at (Left Panel) FL47 and (Right Panel) FL48. Data are from the full period Nov 2018 – Jun 2019. The lower panels also show sonic temperature with humidity corrections with assumed relative humidity of 80 %.



**Figure 12** Difference of sonic temperature and standard temperature as function of wind speed for FL47 (left panel) and FL48 (right panel) for the full Nov-2018 to Jun-2019 period. Sonic temperatures are corrected for humidity with an assumed relative humidity of 80%. The curve in the panels indicates the expected relation when no cross wind correction is performed.

201811-201906 IJSSELM3.B10

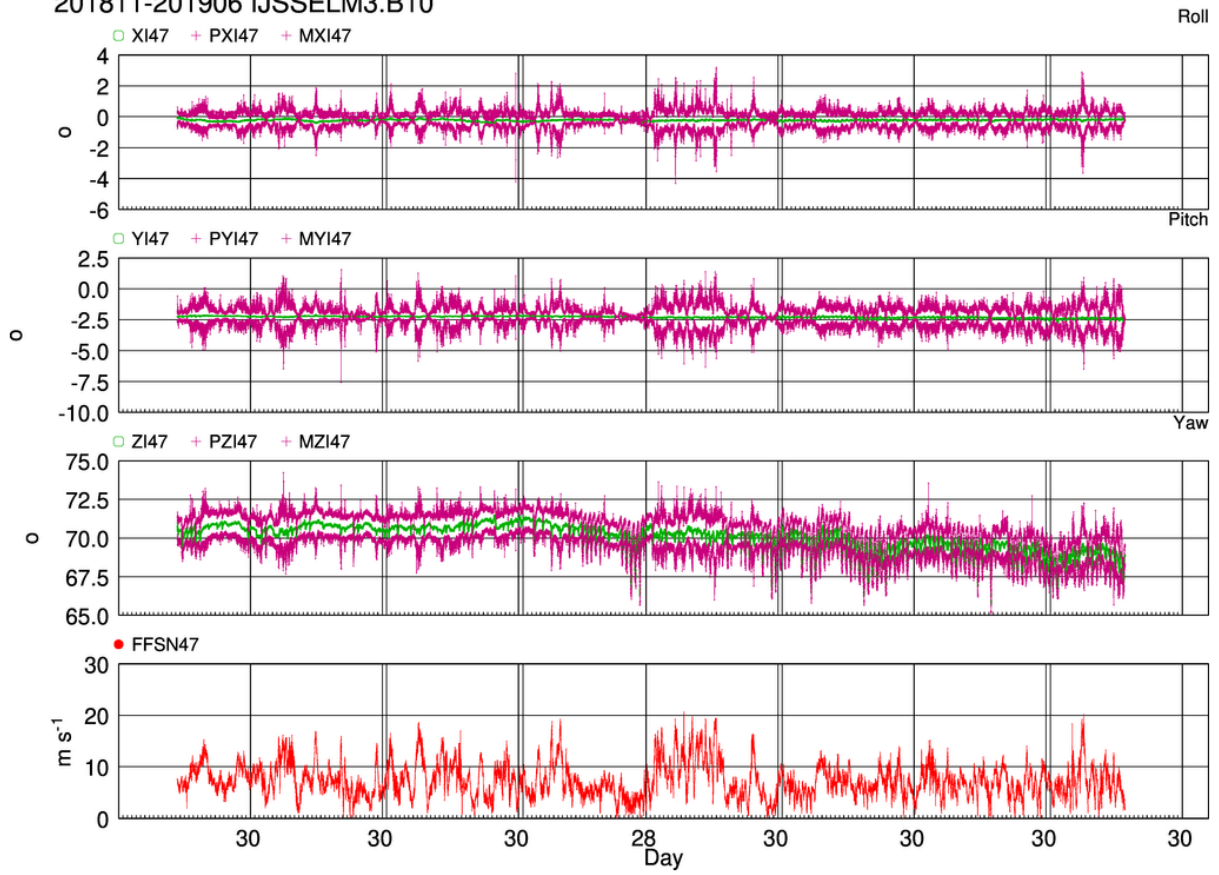


Figure 13 Inclinometers at FL47. 10 minute average minimum and maximum values are shown for the period Nov 2018 – Jun 2019. The lowest panel shows wind speed.

201811-201906 IJSSELM3.B10

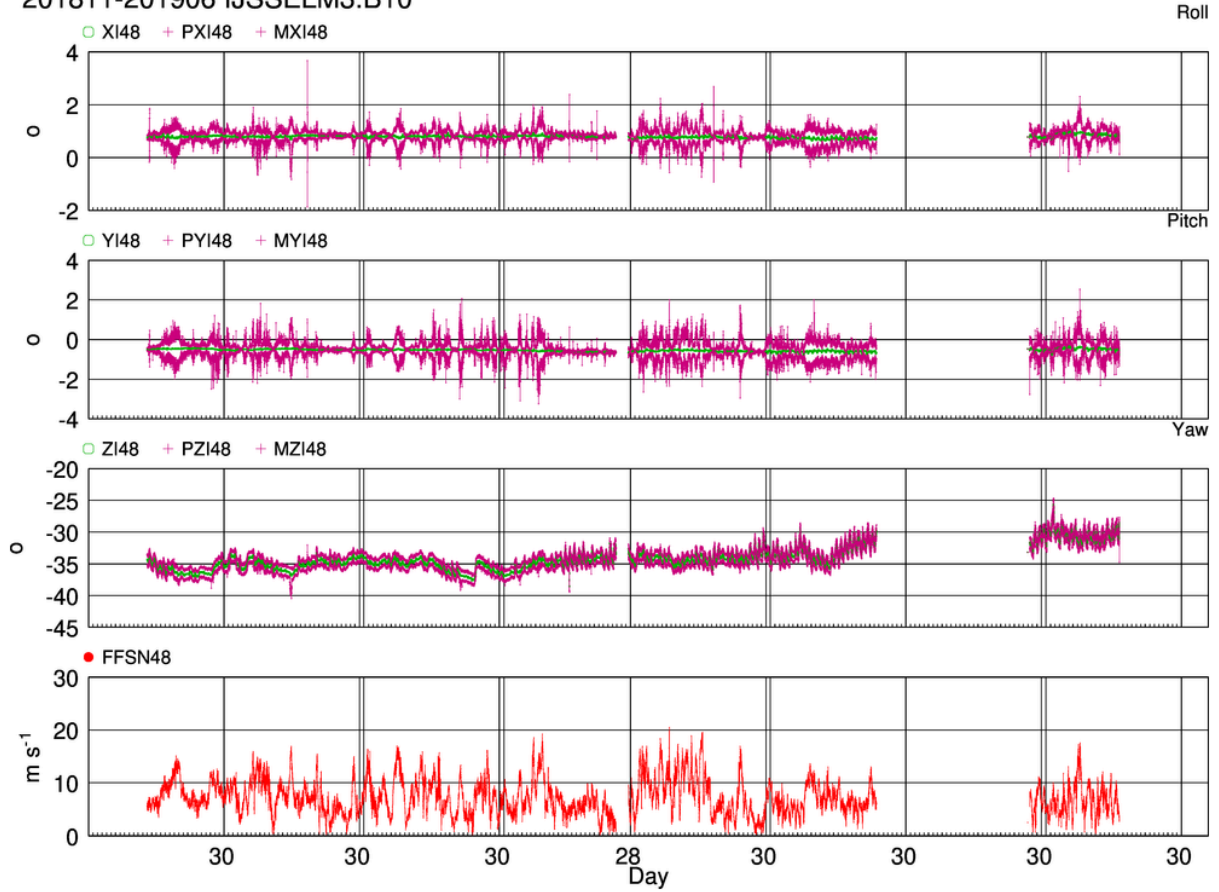


Figure 14 Inclinometers at FL48. 10 minute average minimum and maximum values are shown for the period Nov 2018 – Jun 2019. The lowest panel shows wind speed.

IJSSELM3.B10

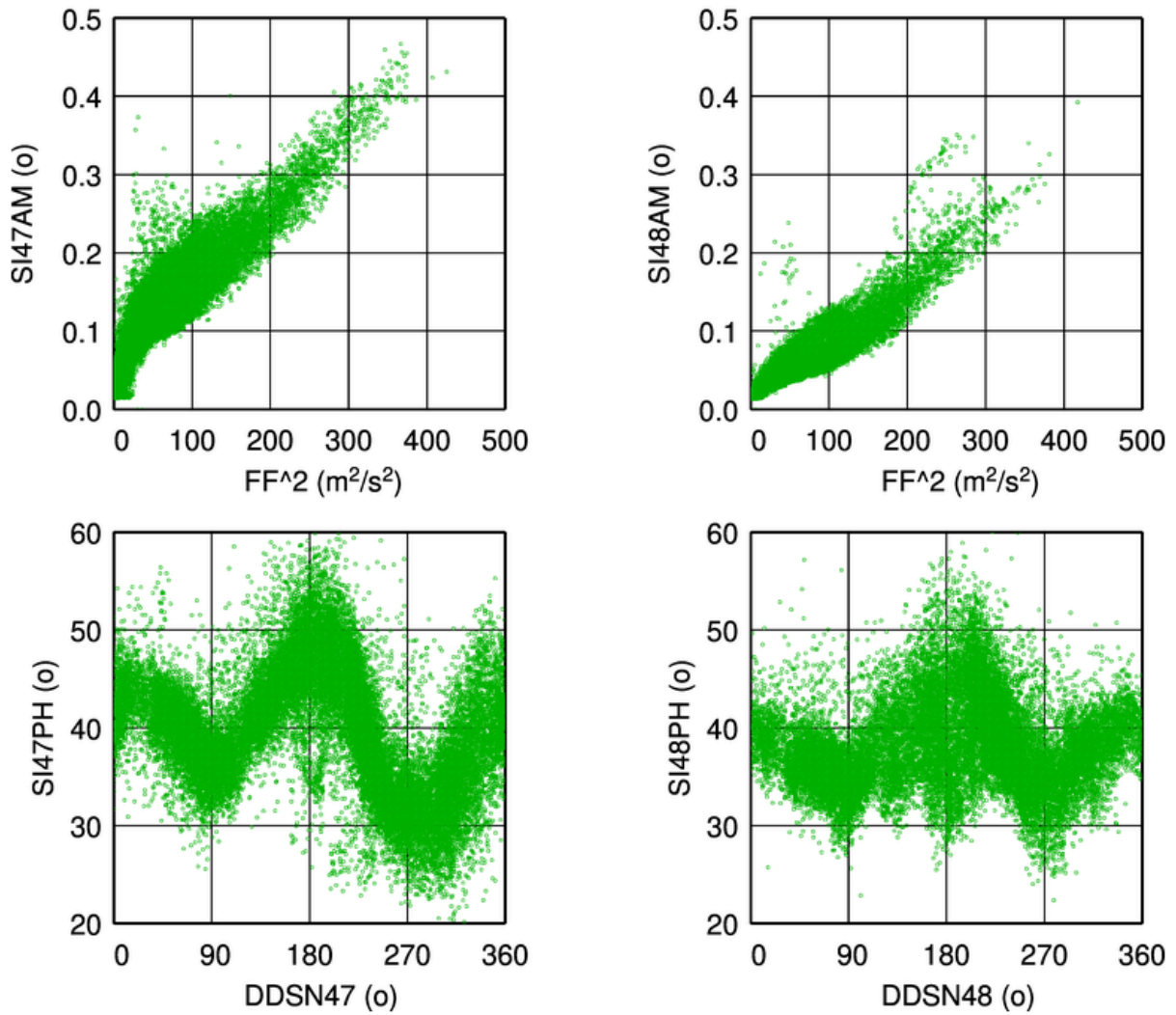
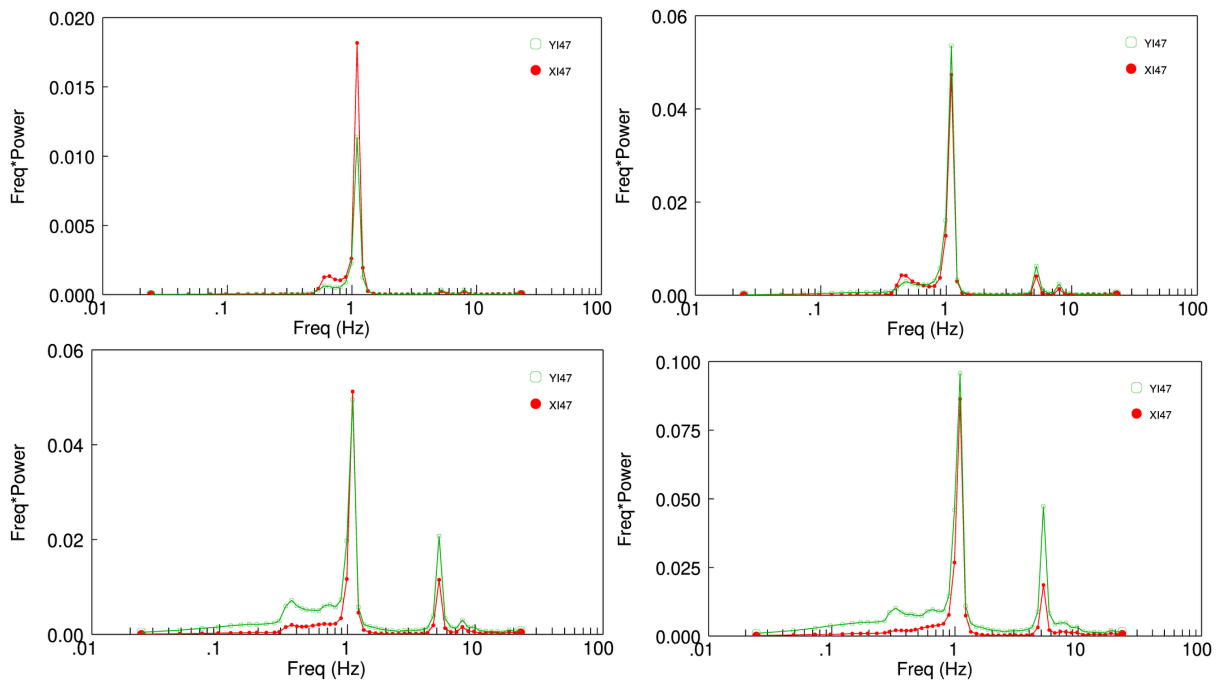
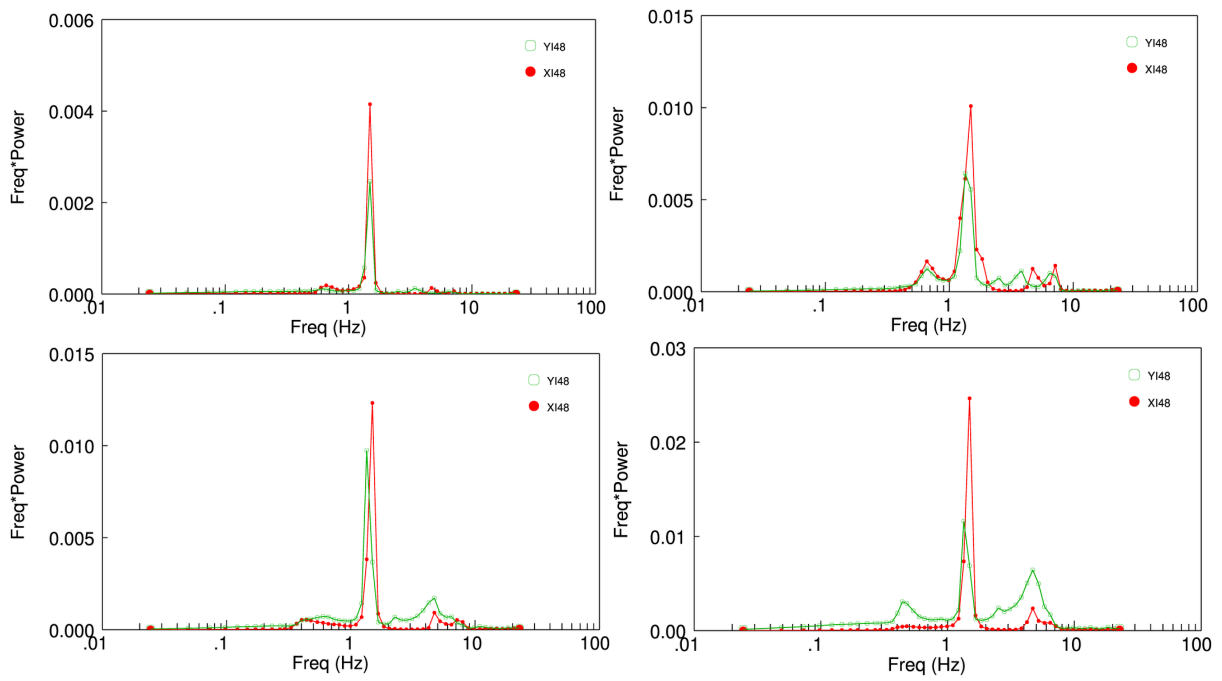


Figure 15 Standard deviation of x and y inclinometers as function of wind. (Upper panels) Amplitude as function of squared wind speed, (Lower panels) Phase as function of wind direction. Left panels FL47 and right panels FL48. Data are from the full period Nov 2018 – Jun 2019.



**Figure 16 Spectra of x and y inclinometers at FL47. (UL) FF=3.5 m/s; (UR) 7 m/s; (LL) FF=10 m/s; (LR) 13 m/s. Note the different scaling of the y-axis.**



**Figure 17 Spectra of x and y inclinometers at FL48. (UL) FF=3.5 m/s; (UR) 7 m/s; (LL) FF=10 m/s; (LR) 13 m/s. Note the different scaling of the y-axis..**

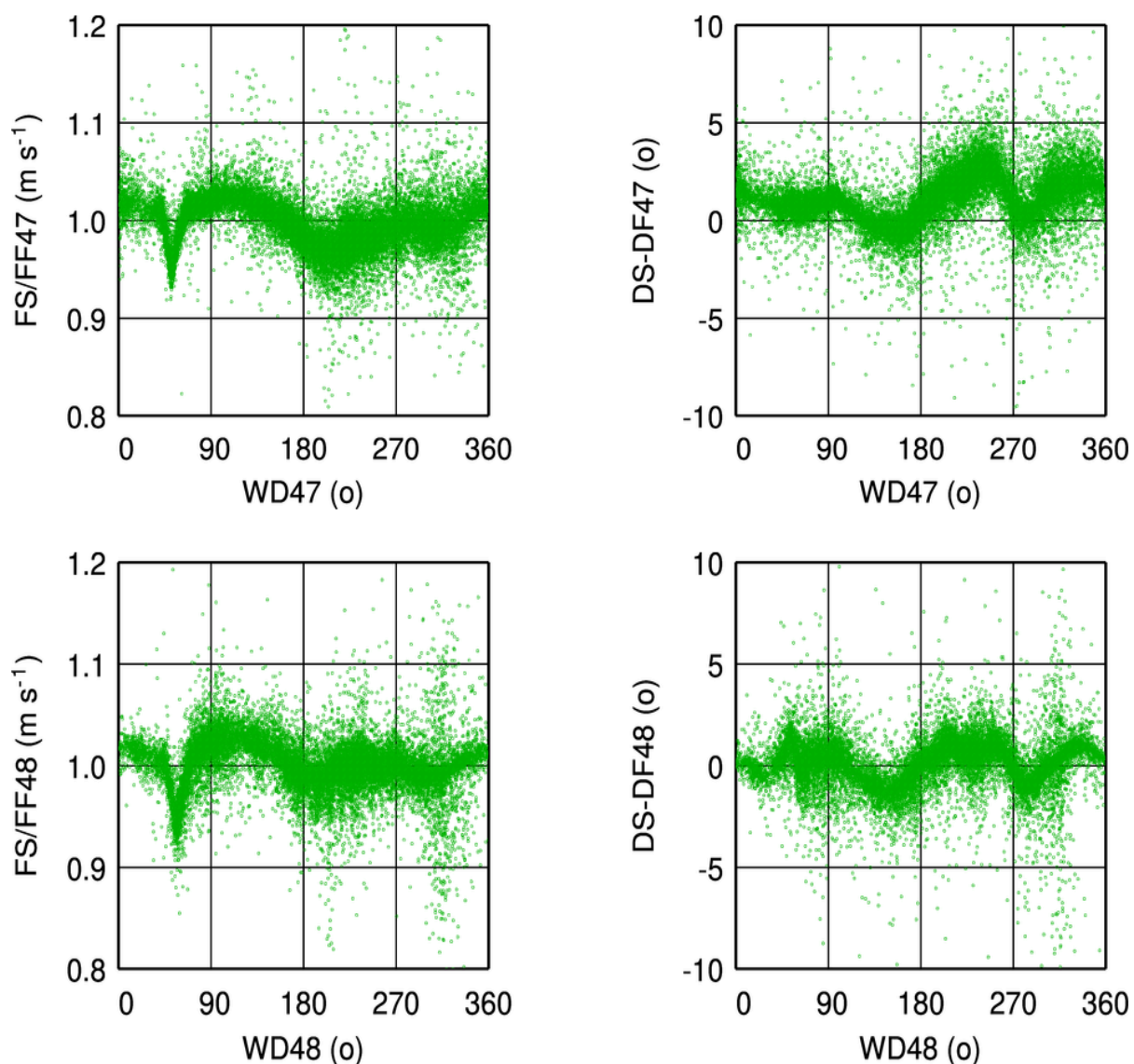


**Figure 18** Difference between sonic wind and standard wind as function of wind direction. (Left panels) wind speed ratio (sonic divided by cup), (right panels) wind direction difference (sonic minus vane). For FL47 (top panels) and FL48 (lower panels). Observations from the full period Nov 2018 – Jun 2019 are taken with wind speeds larger than 3 m/s, and with no significant missing values at the sample level.

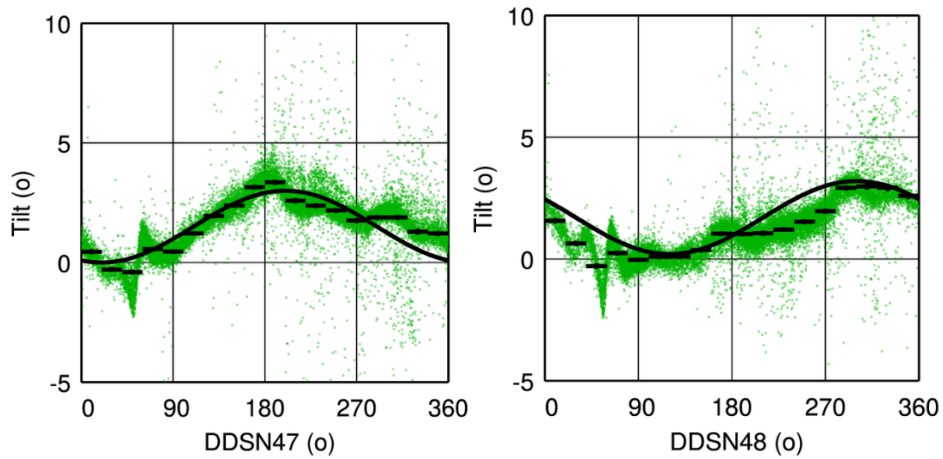


**Figure 19** Apparent slope of streamlines derived from 10-min sonic data as function of wind direction for FL47 (left panel), and FL48 (right panel). “eye-fit” sinuses are drawn. Tilt is calculated from the ratio of vertical and horizontal sonic wind. Observations from the full period Nov 2018 – Jun 2019 with windspeed larger than  $3 \text{ m s}^{-1}$  are plotted. Data are binned in 20 degree wind direction classes and for each class the average value is also shown.

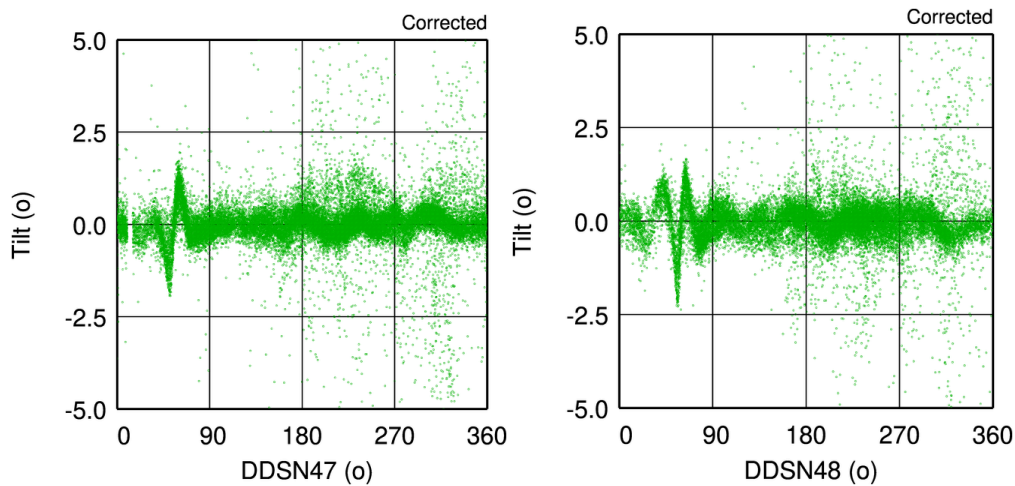


**Figure 20** Remaining tilt of streamlines derived from 10-min sonic data as function of wind direction after tilt correction for FL47 (left panel), and FL48 (right panel). Observations from the full period Nov 2018 – Jun 2019 with windspeed larger than  $3 \text{ m s}^{-1}$  are plotted.

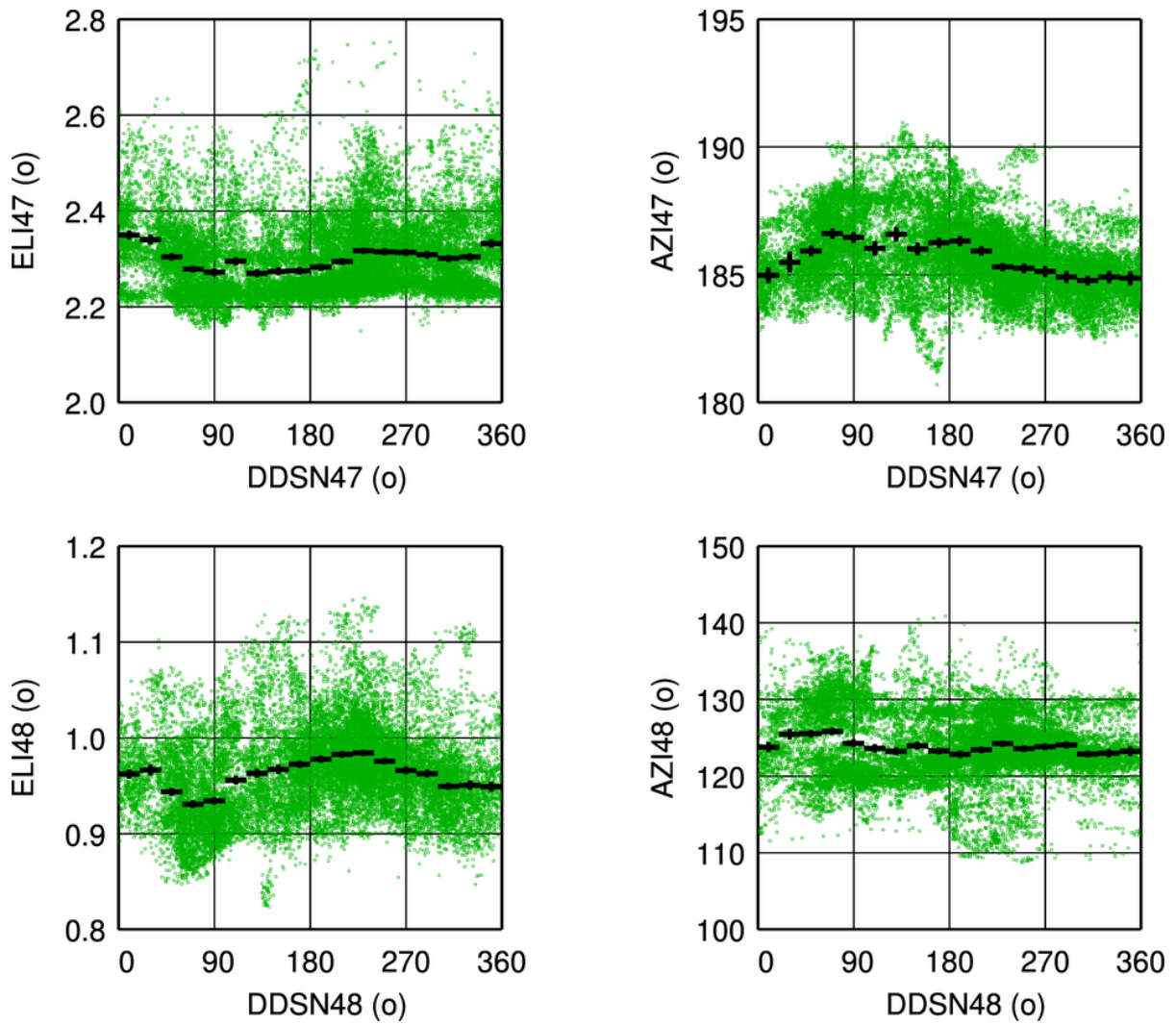


**Figure 21** Tilt (left) and azimuth (right) of x-y inclinometer pairs at FL47 (top) and FL48 (bottom) as function of wind direction. 10 min. data are used with wind speeds larger than 3 m/s for the full period Nov 2018 – Jun 2019.

**Figure 22 A-D: Full co-spectral information of observed fluctuations for a steady 4 hour period (03-Nov-2014) at the 60-m level of the Cabauw 200 m tower, FF=10 m/s, DD=180°. (UL-panel) Power spectra of both parameters, (UR-panel) covariance spectrum, (LL-panel) coherence spectrum, and (LR-panel) phase-spectrum.**

**Figure 22A) Co-spectrum of along wind (YS060), and vertical wind (WS060)**

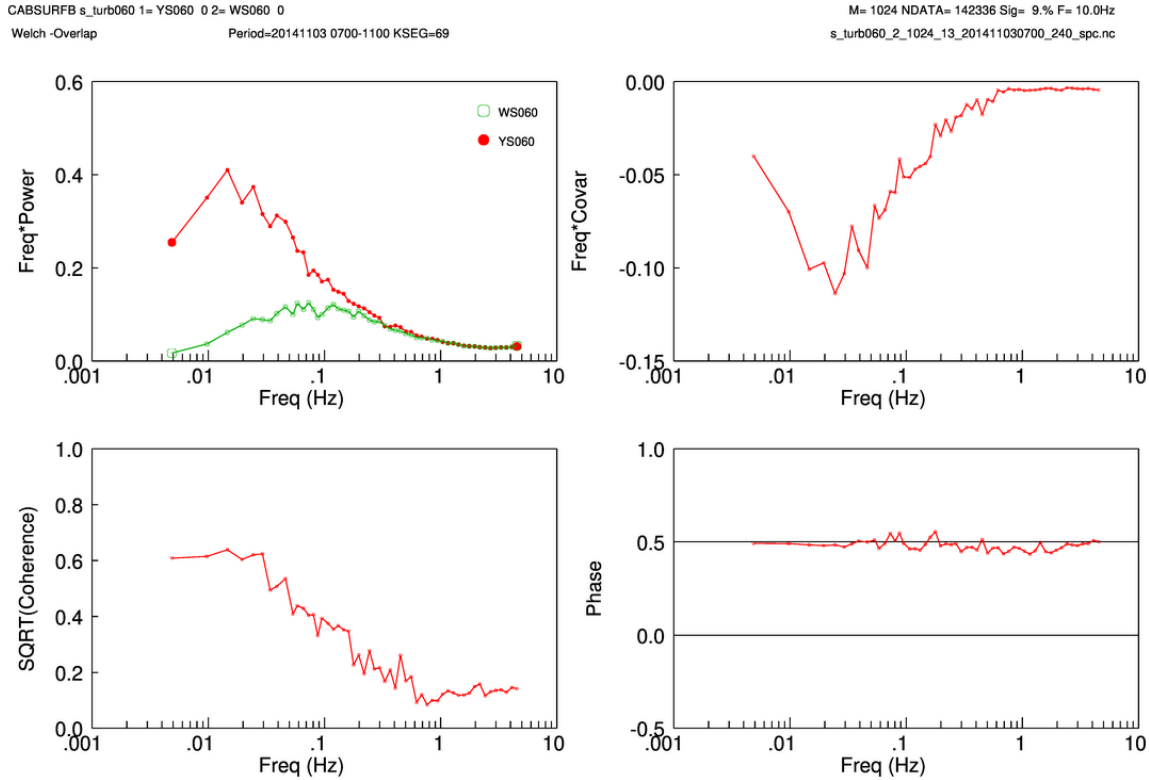


**Figure 22B) Co-spectrum of cross wind (XS060), and vertical wind (WS060)**

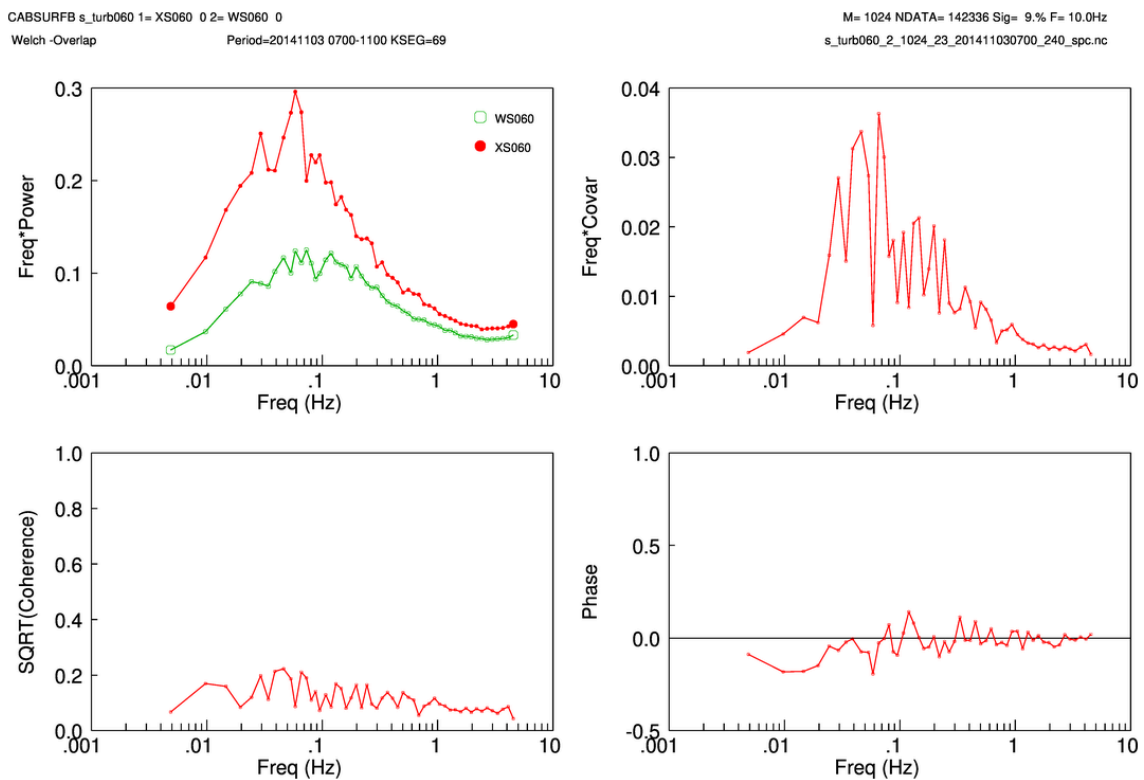


**Figure 22C) Co-spectrum of along wind (YS060) and cross wind (XS060)**

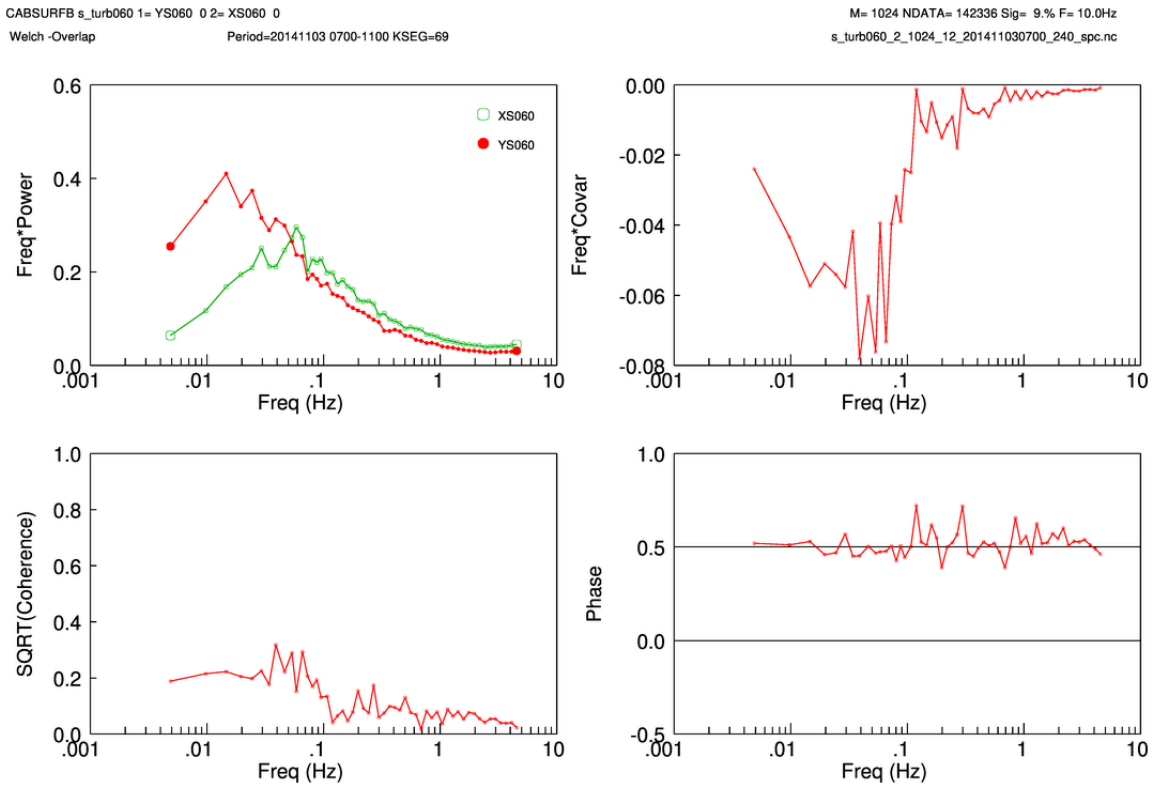


**Figure 22D) Co-spectrum of vertical wind (WS060), and sonic temperature (TS060)**

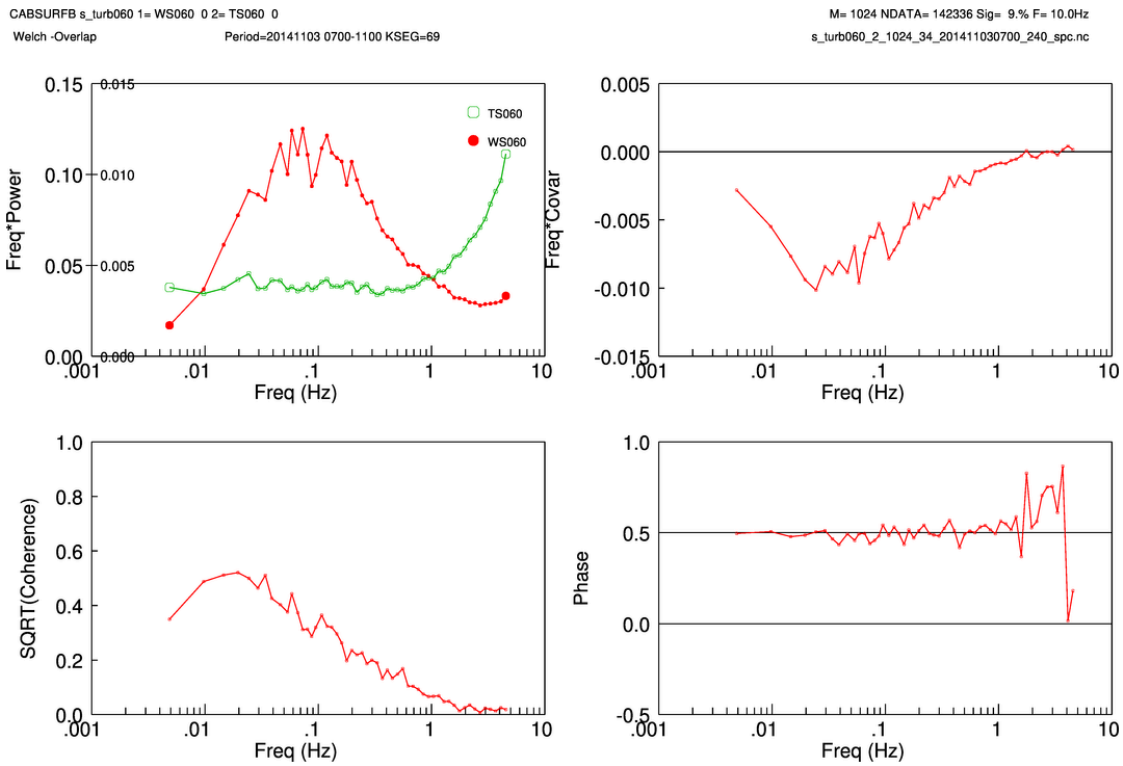


**Figure 23 A-E: Full co-spectral information of observed fluctuations for a steady 3 hour period (04-Mar-2017) at FL47. FF=17.0 m/s, DD=258°. For the meaning of the 4 co-spectral panels see Figure 22.**

**Figure 23A) Co-spectrum of along wind (US47) and vertical wind (WS47)**

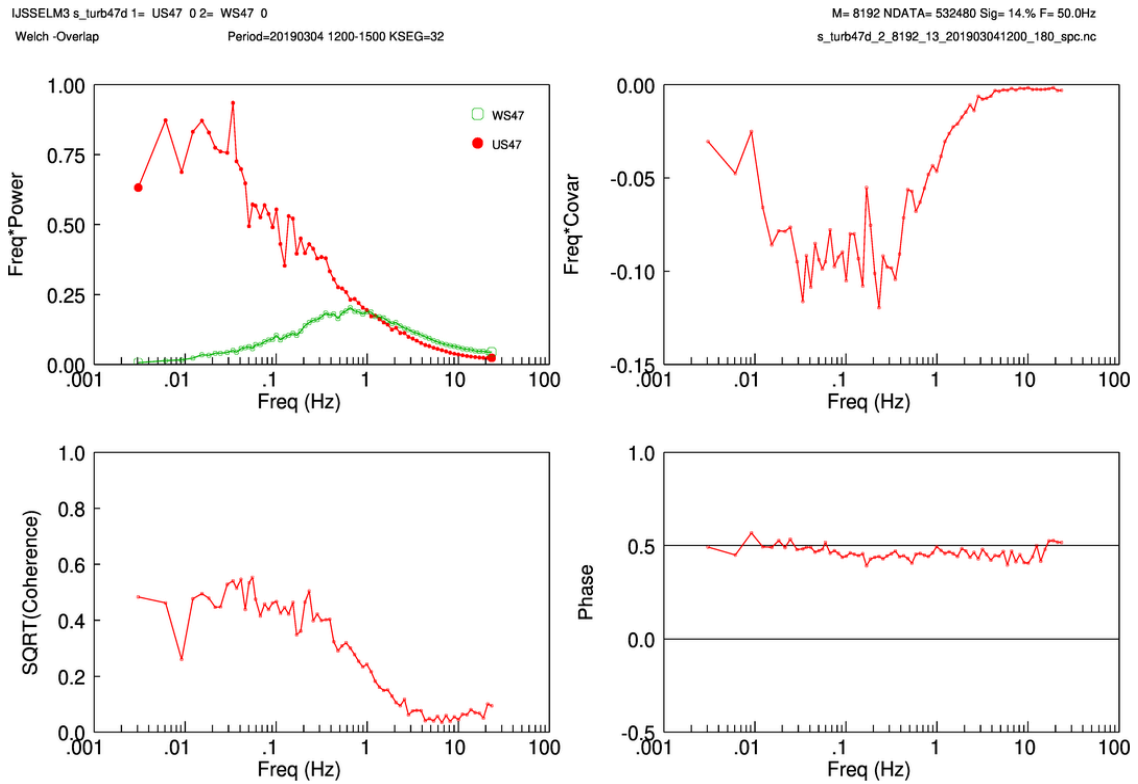


**Figure 23B) Co-spectrum of along wind and (US47) and cross wind (VS47)**

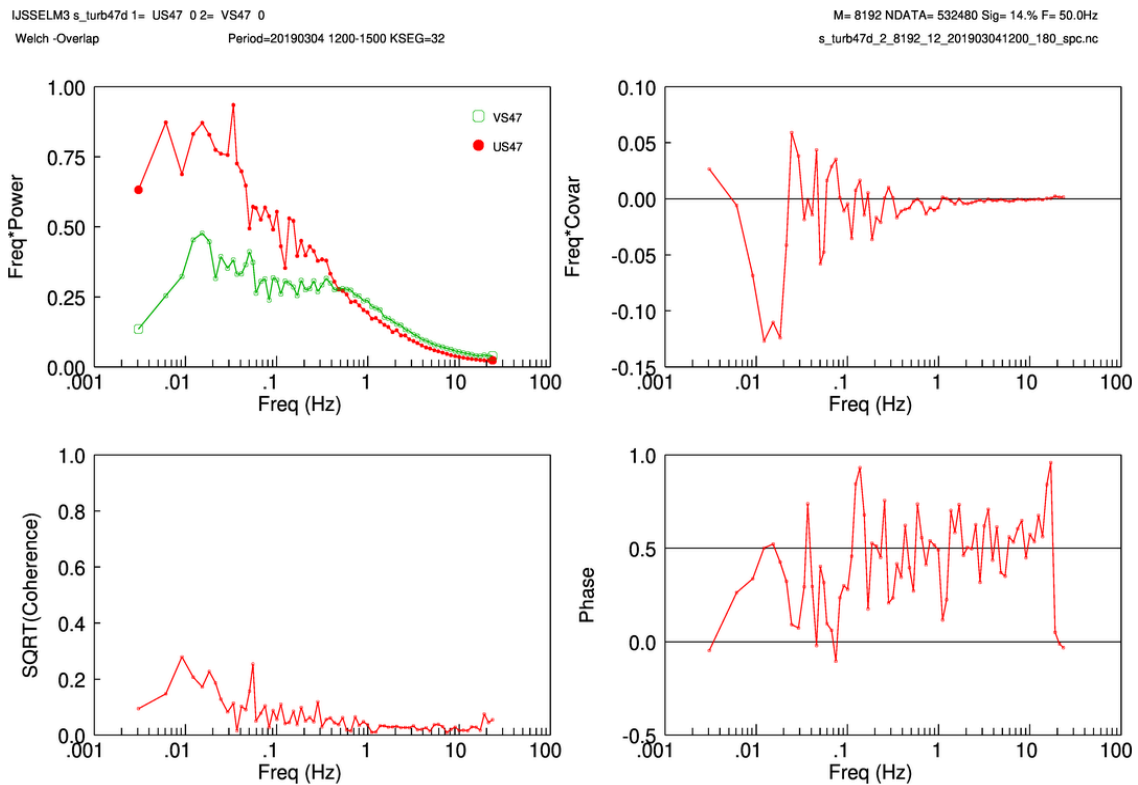


**Figure 23C) Co-spectrum of cross wind (VS47) and vertical wind (WS47)**

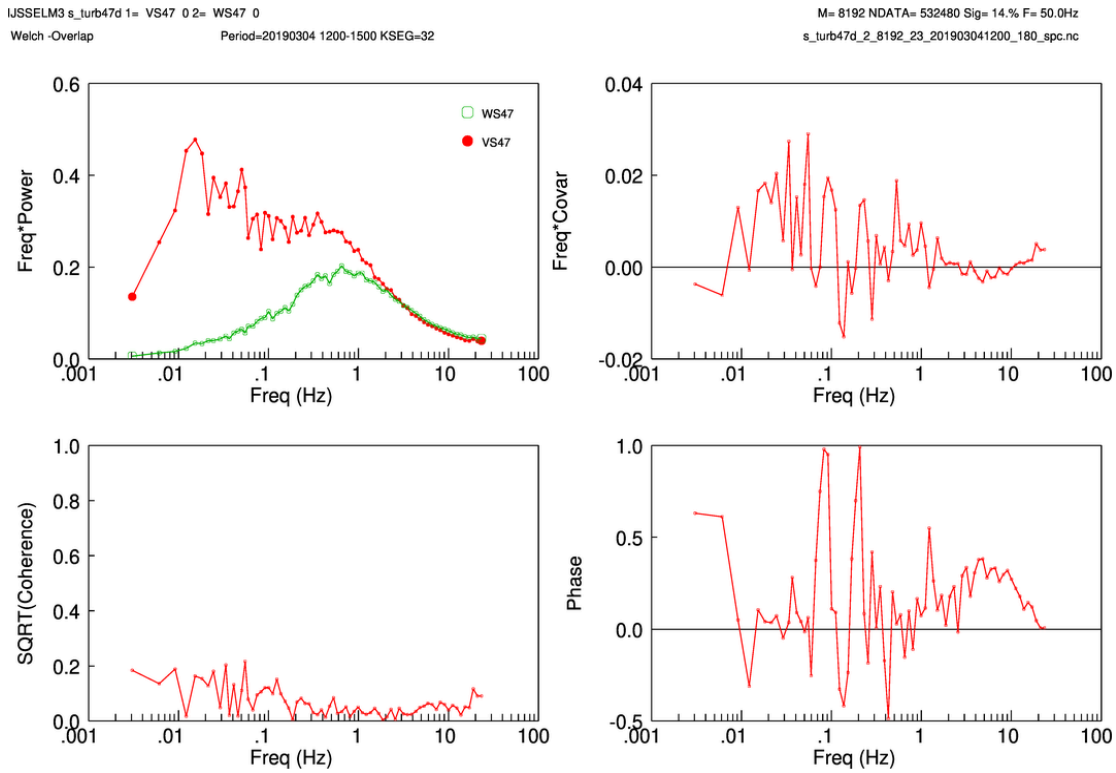


**Figure 23D) Co-spectrum of vertical wind (WS47) and sonic temperature (TS47)**

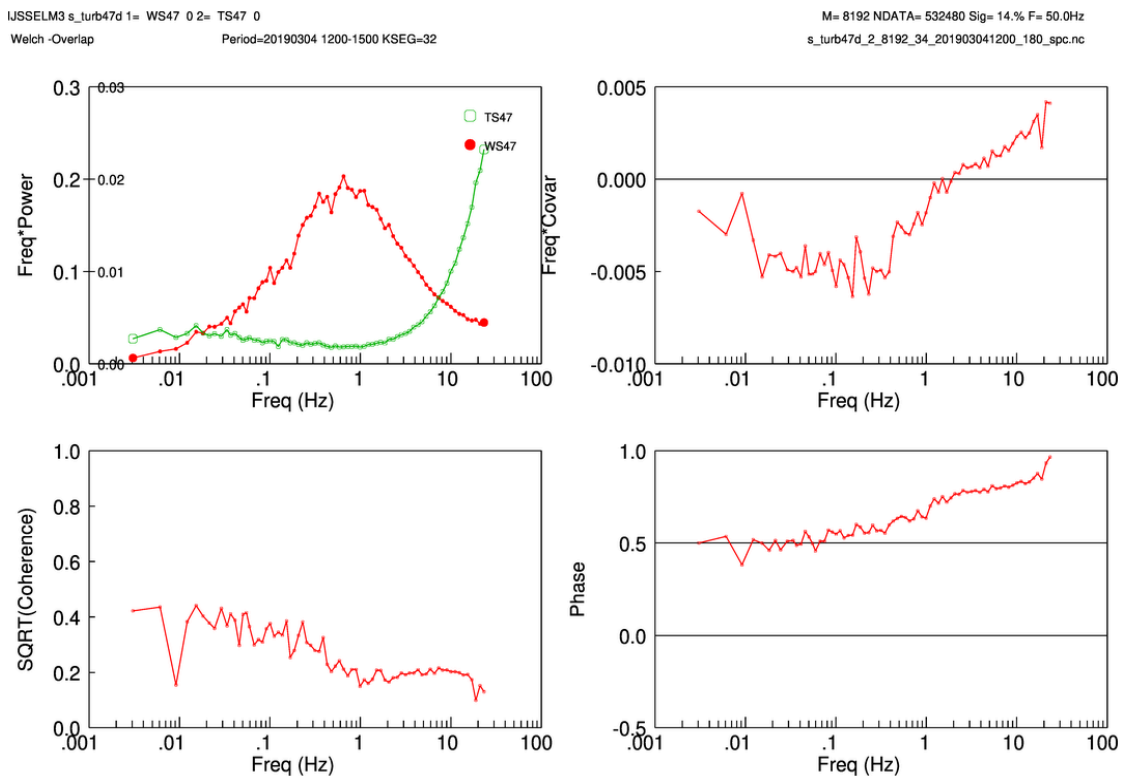


**Figure 23E) Power spectra of along wind (US47) and cross wind (VS47) (Left panel), and cross wind (VS47) and vertical wind (WS47) (Right panel)**

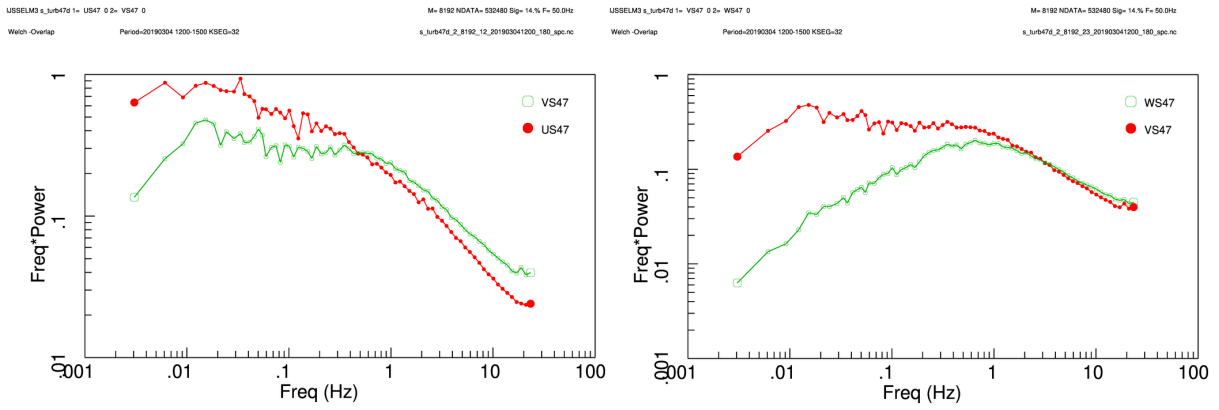


**Figure 24 A-D: Full co-spectral information of observed fluctuation at FL48 for the same period (04-Mar-2017) as is displayed for FL47 in Figure 23. FF=17.0 m/s, DD=258°. For the meaning of the 4 panels see Figure 22.**

**Figure 24A) Co-spectrum of along wind (US48) and vertical wind (WS48)**

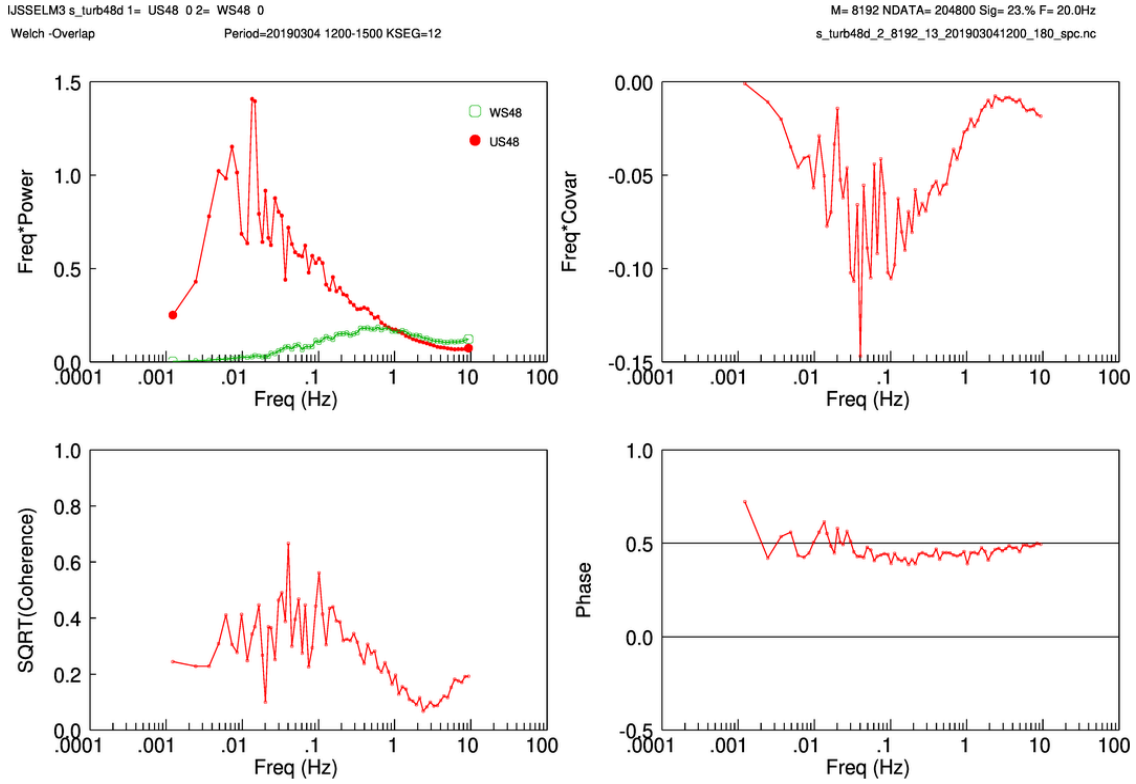


**Figure 24B) Co-spectrum of along wind (US48) and cross wind (VS48)**

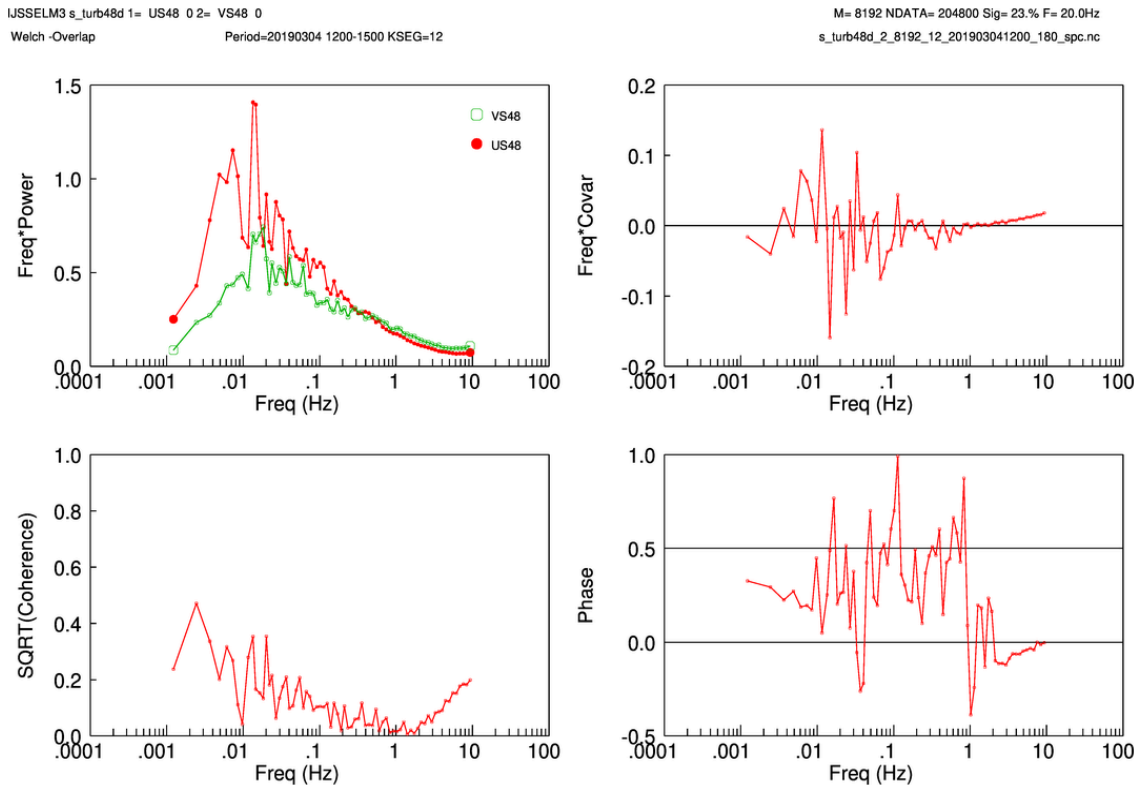


**Figure 24C) Co-spectrum of cross wind (VS47) and vertical wind (WS47)**

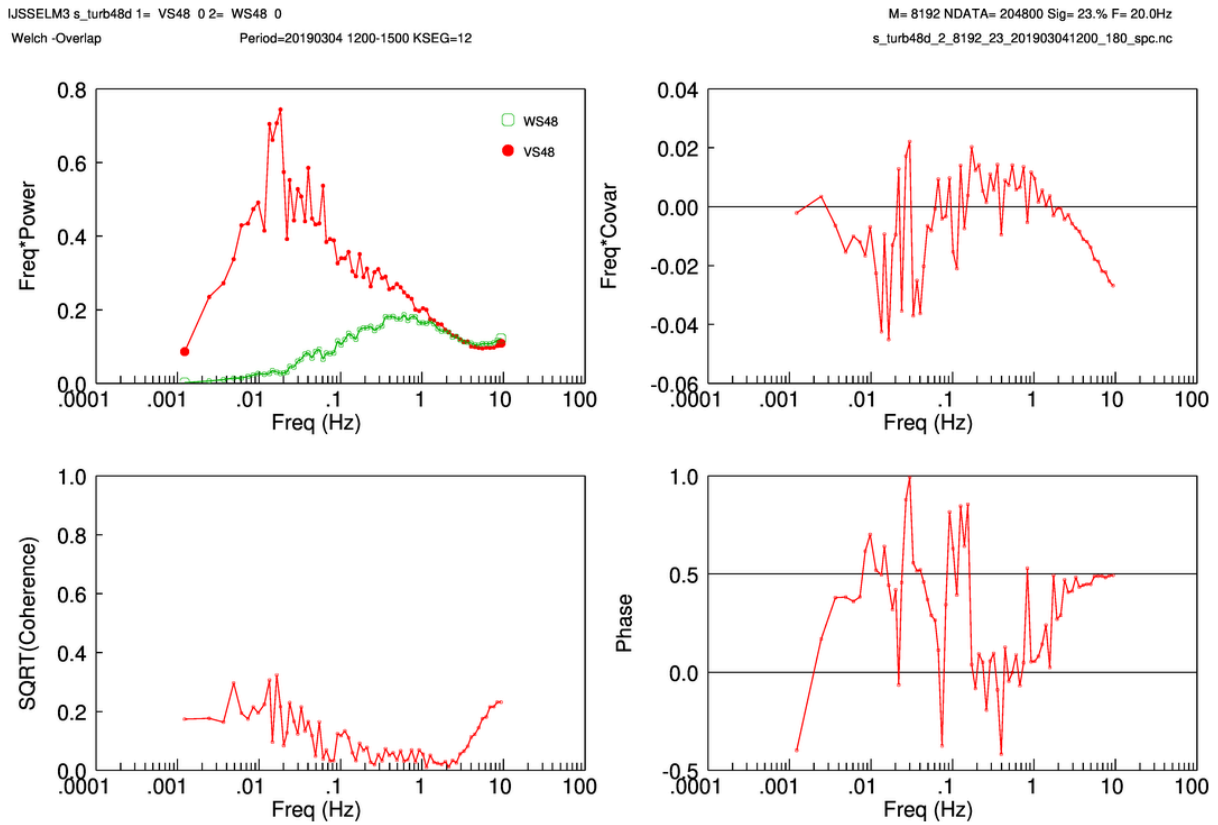


**Figure 24C) Co-spectrum of vertical wind (WS48) and sonic temperature (TS48)**

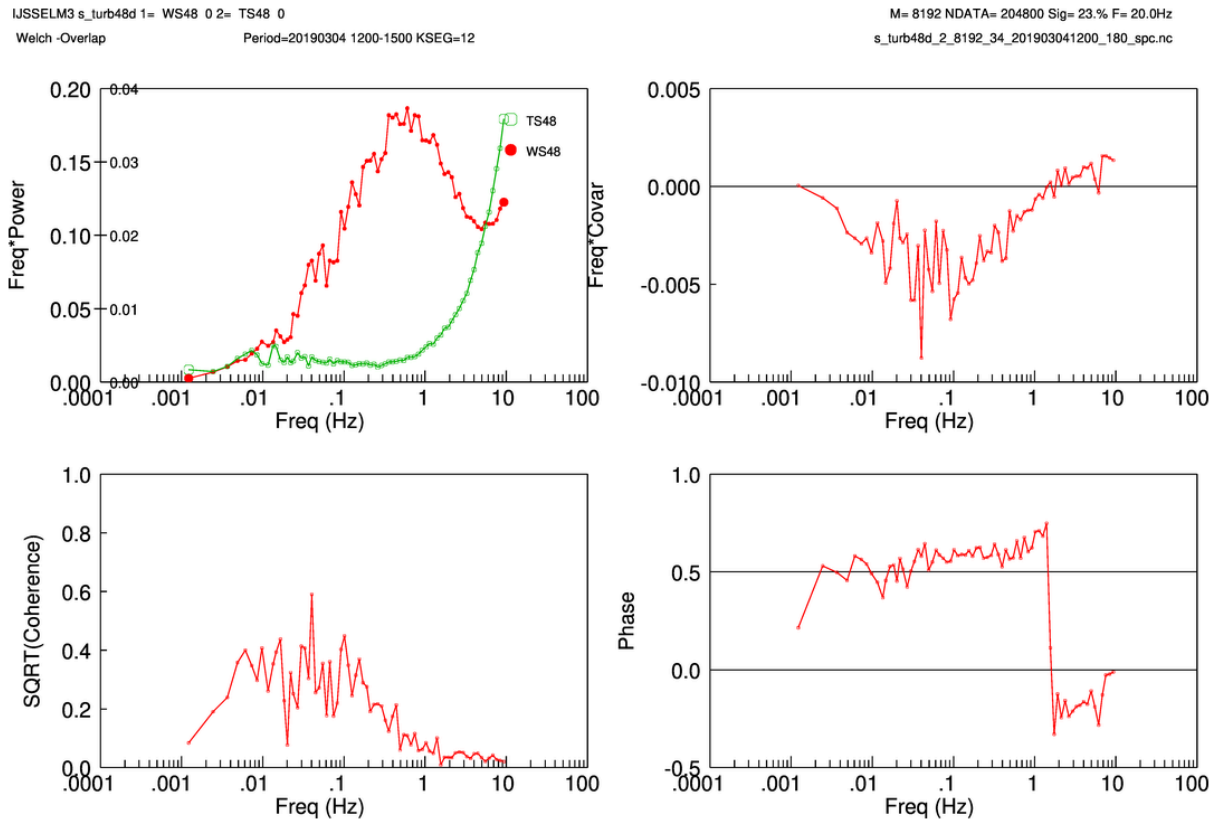


**Figure 24D)** Power spectra of along wind (US48) and cross wind (VS48) (Left panel), and cross wind (VS48) and vertical wind (WS48) (Right panel)

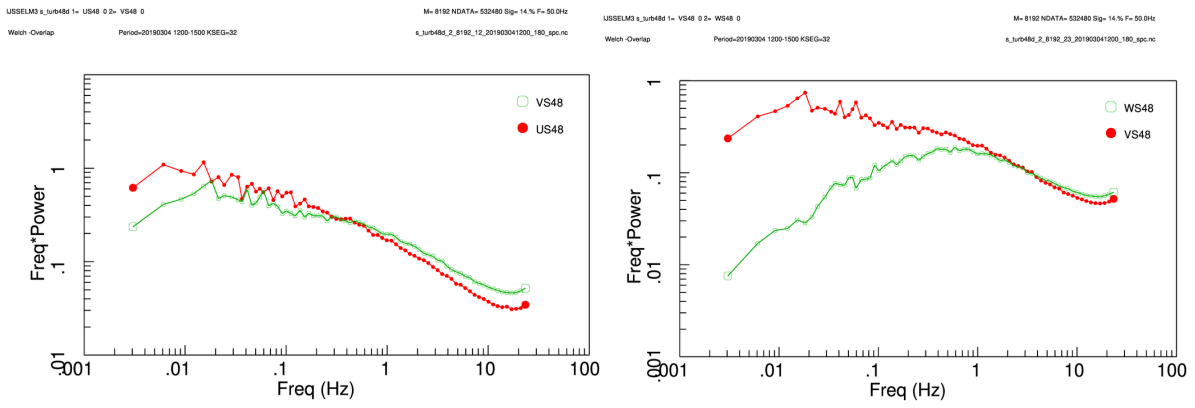


**Figure 25 A-B: Full co-spectral information of observed fluctuations for a steady 3 hour period (05-Mar-2019) at FL47 and FL48. FF=9.7 m/s, DD=236°. For the meaning of the 4 panels see Figure 22.**

**Figure 25A) Co-spectrum of along wind (US47) and vertical wind (WS47)**

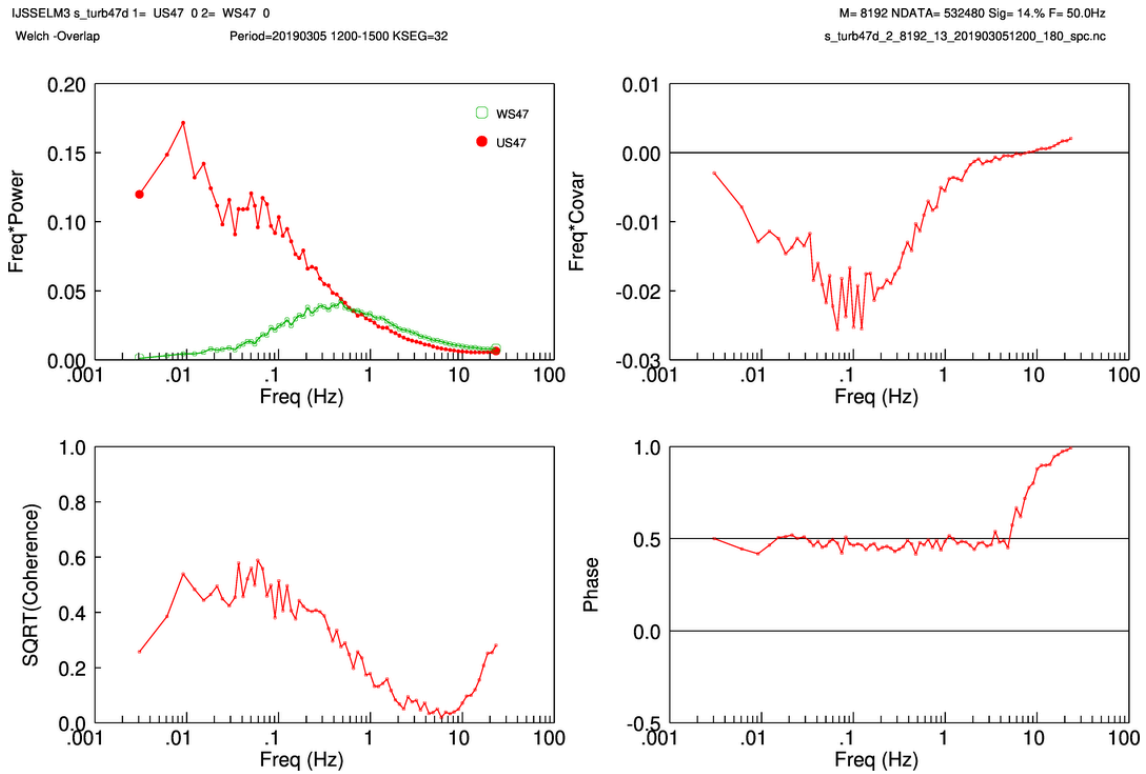


**Figure 25B) Co-spectrum of along wind (US48) and vertical wind (WS48)**

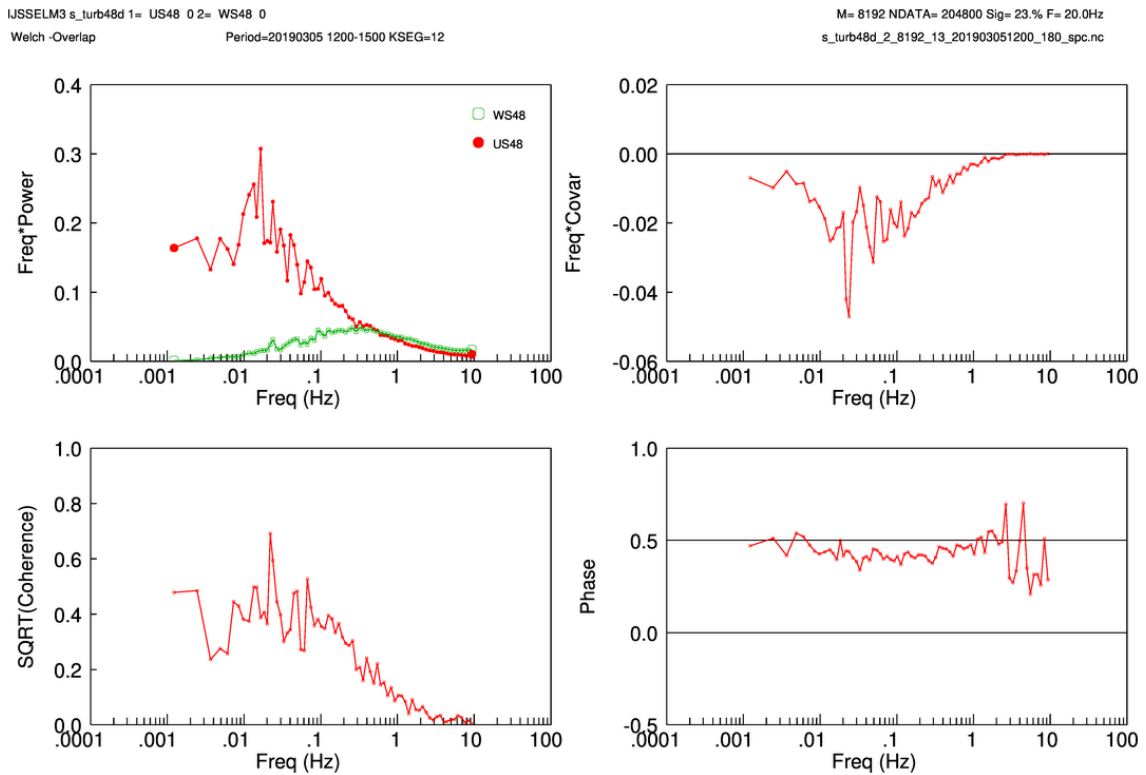


**Figure 26 A-B: Full co-spectral information of observed fluctuations for a steady 3 hour period (09-Mar-2019) at FL47 and FL48. FF=16.5 m/s, DD=285°. For the meaning of the 4 panels see Figure 22.**

**Figure 26A) Co-spectrum of along wind (US47) and vertical wind (WS47)**

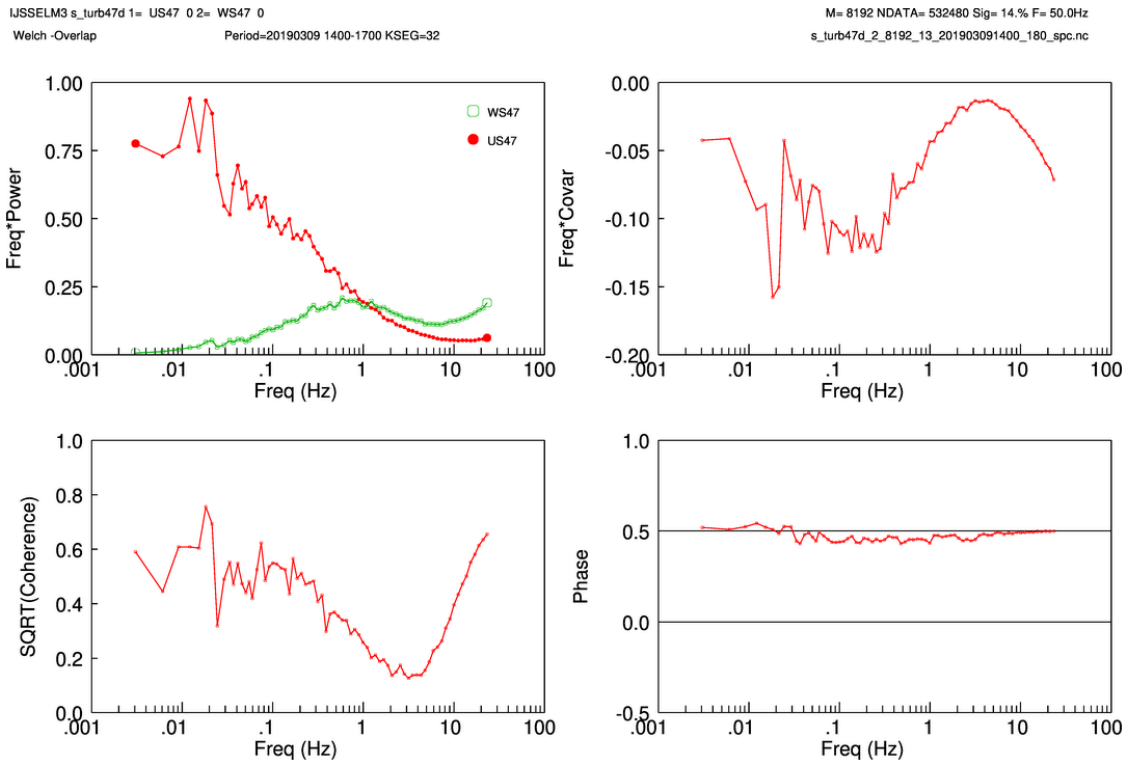


**Figure 26B) Co-spectrum of along wind (US48) and vertical wind (WS48)**

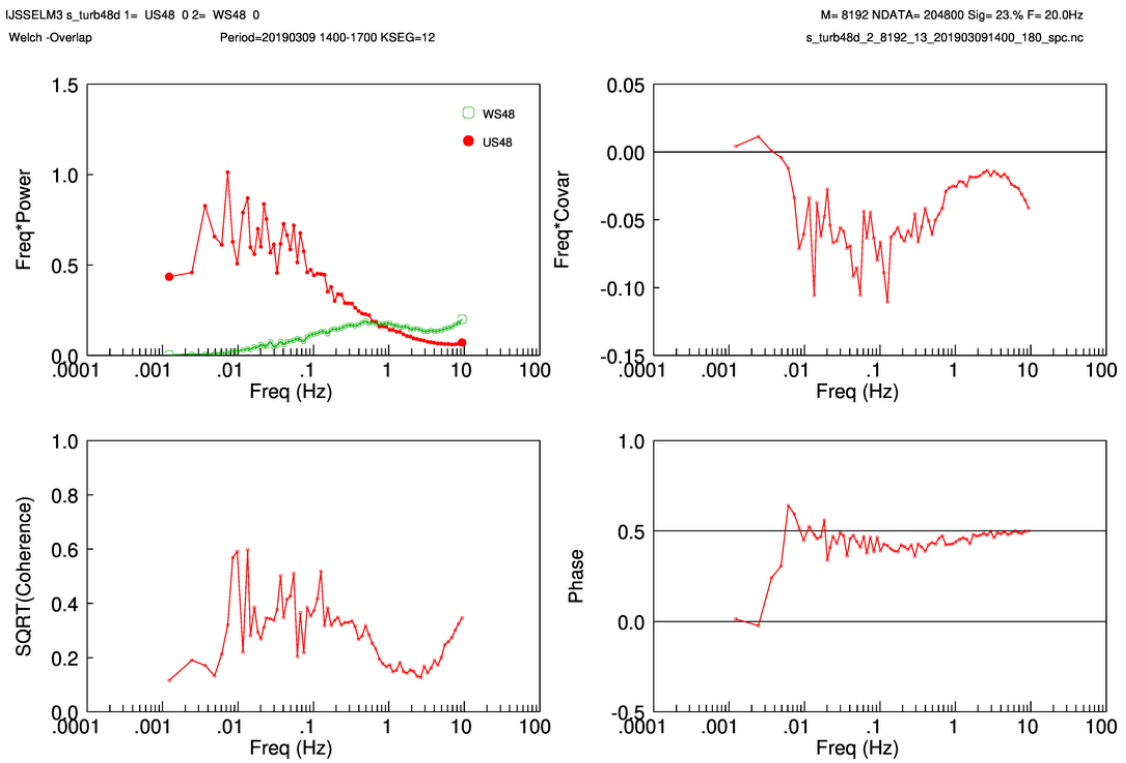


**Figure 27 A-B: Full co-spectral information of observed fluctuations for a steady 3 hour period (11-Mar-2019) at FL47. FF=18.1 m/s, DD=291°. For the meaning of the 4 panels Figure 22.**

**Figure 27A) Co-spectrum of along wind (US47) and vertical wind (WS47)**

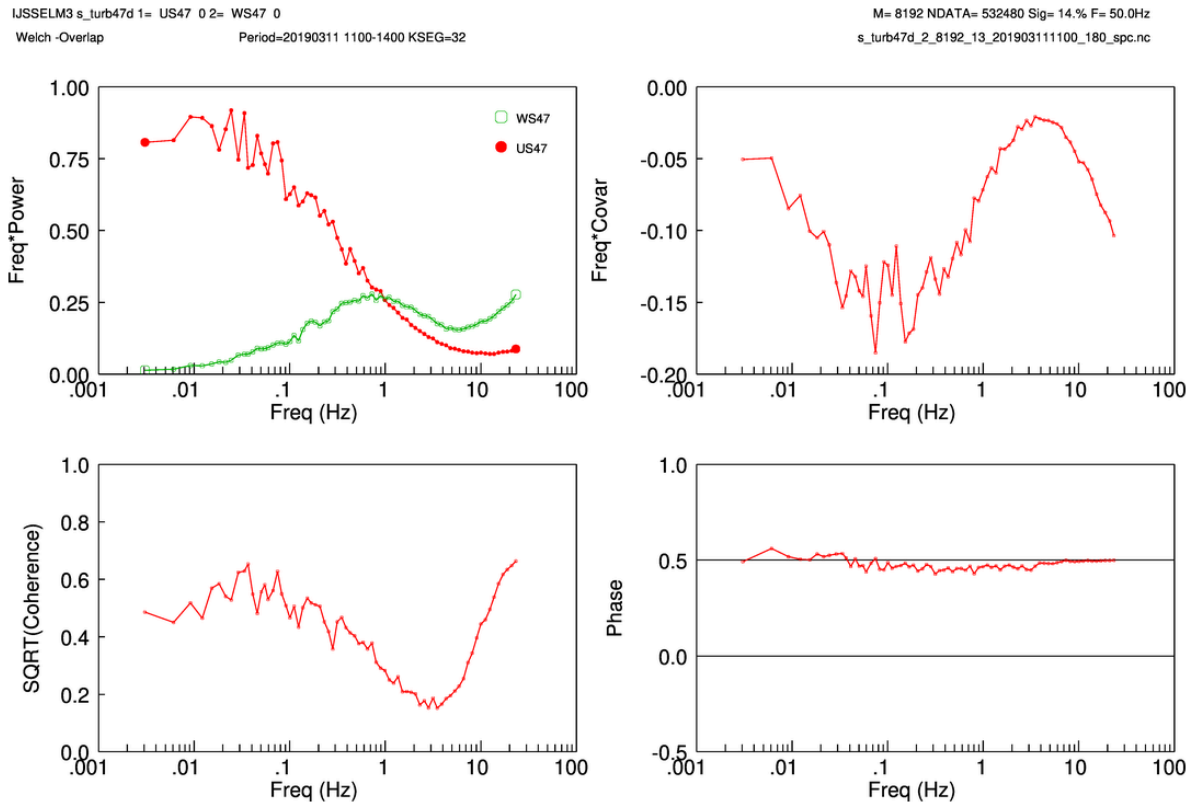


**Figure 27B) Co-spectrum of along wind (US48) and vertical wind (WS48)**

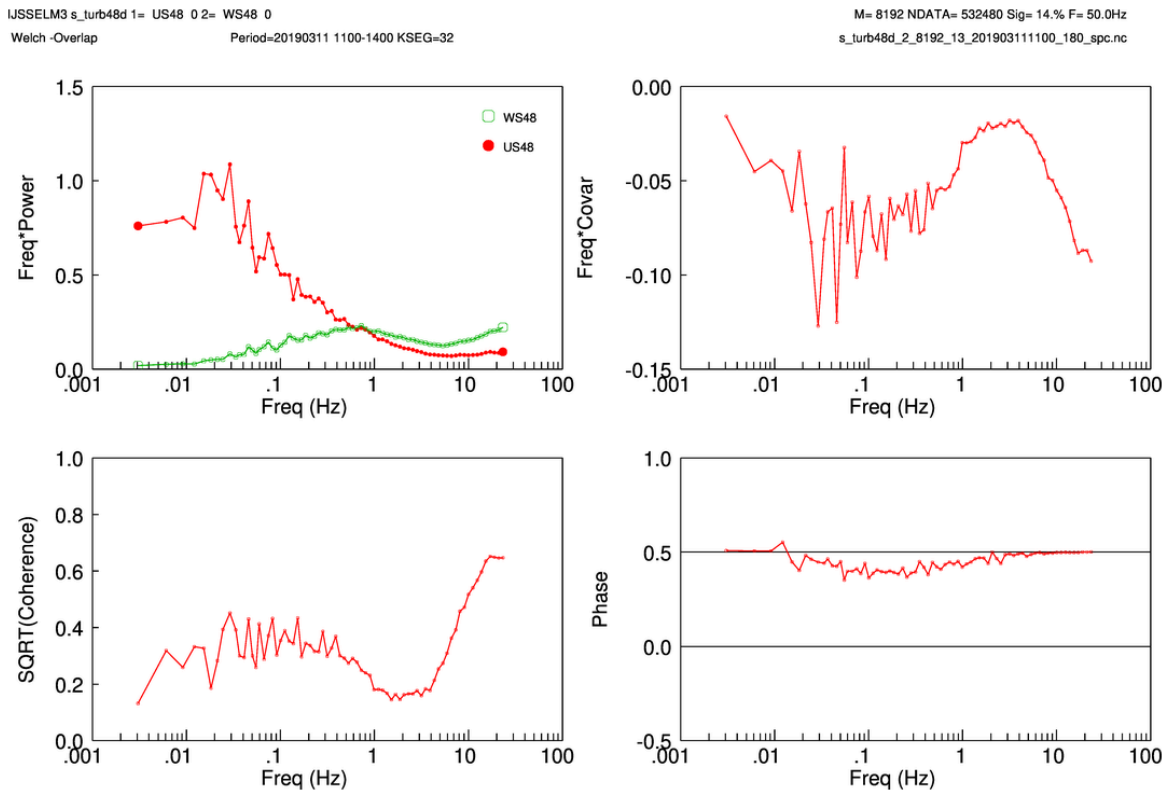


**Figure 28 A-B: Full co-spectral information of observed fluctuations for a steady 2 hour period (13-Mar-2019) at FL47 and FL48 . FF=15.4 m/s, DD=263°. For the meaning of the 4 panels Figure 22.**

**Figure 28A) Co-spectrum of along wind (US47) and vertical wind (WS47)**

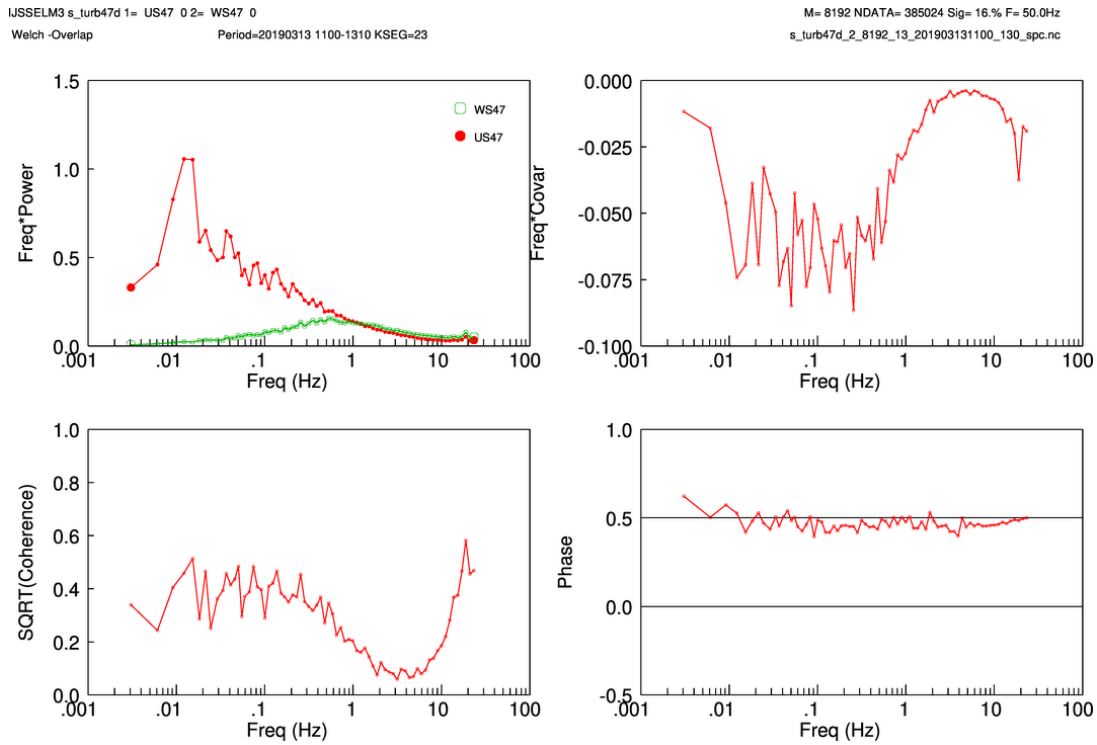


**Figure 28B) Co-spectrum of along wind (US48) and vertical wind (WS48)**

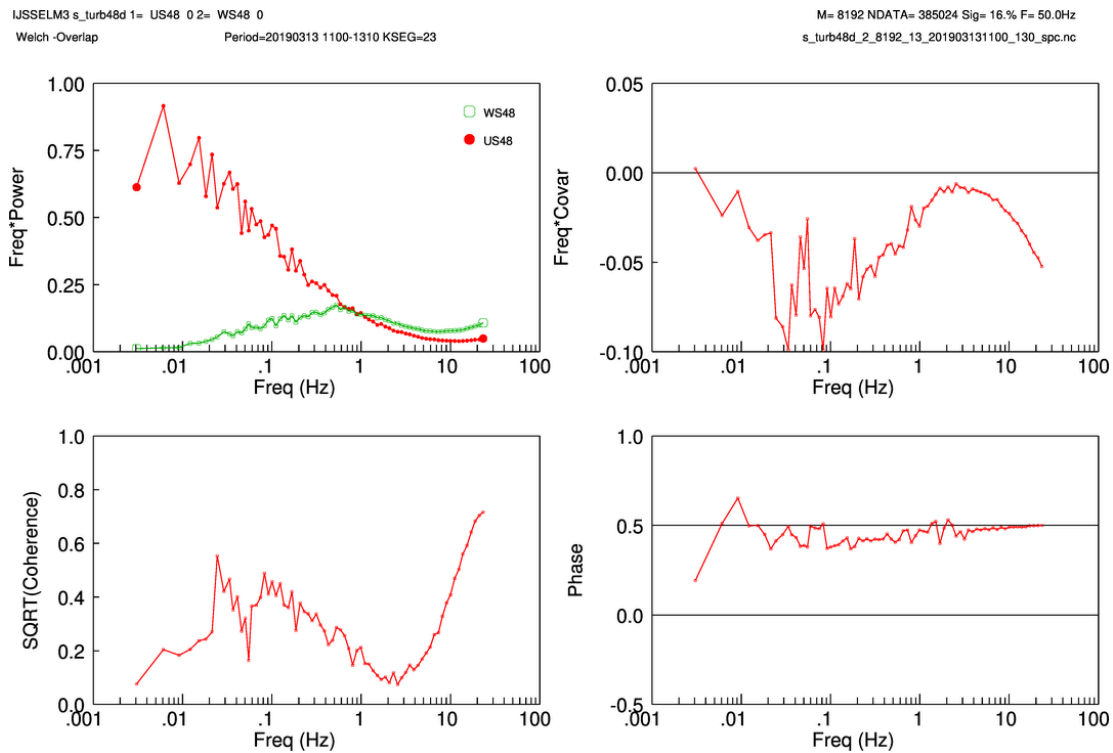


**Figure 29 A-B: Full co-spectral information of observed fluctuations for a steady 3 hour period (14-Mar-2019) at FL47 and FL48 . FF=13.1 m/s, DD=227°. For the meaning of the 4 panels see Figure 22.**

**Figure 29A) Co-spectrum of along wind (US47) and vertical wind (WS47)**

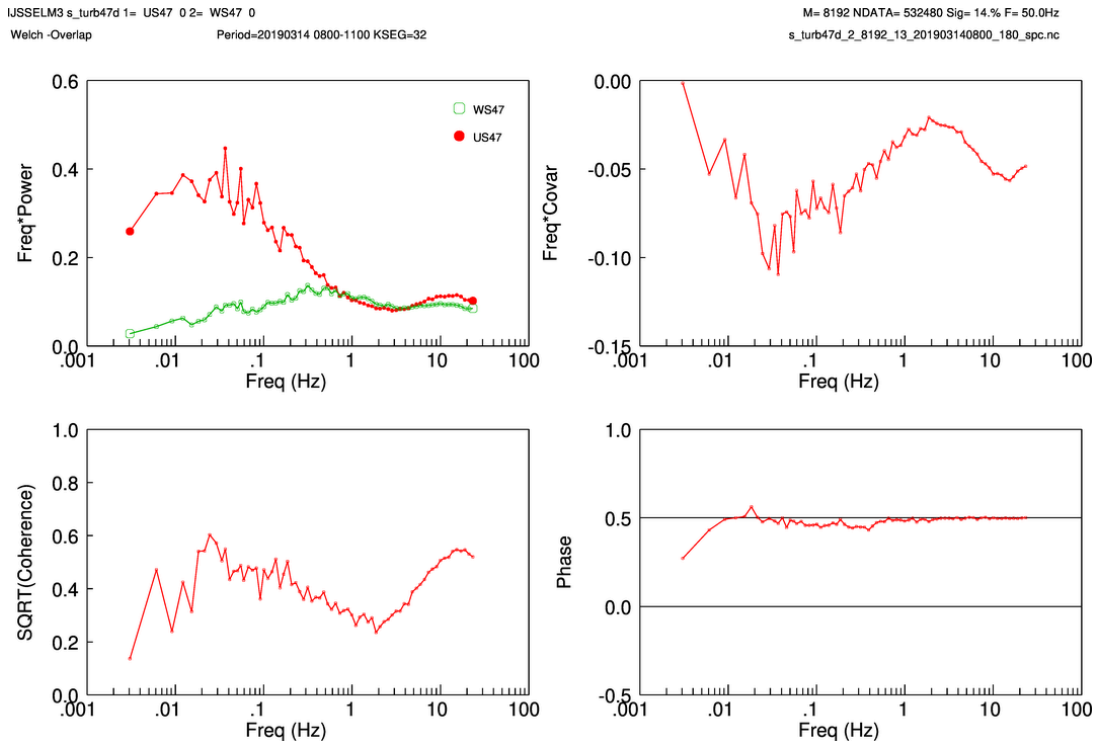


**Figure 29B) Co-spectrum of along wind (US48) and vertical wind (WS48)**

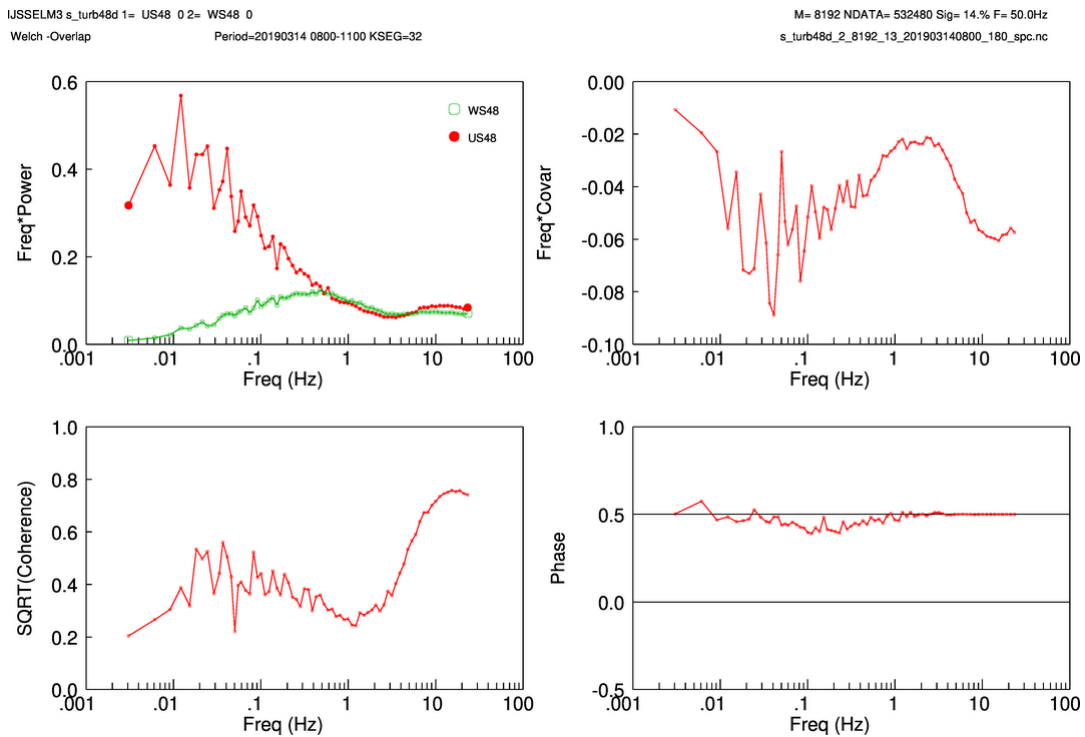


**Figure 30 A-B: Full co-spectral information of observed fluctuations for a steady 2 hour period (10-Mar-2019) at FL47 and FL48. FF=3.6 m/s, DD=165°. For the meaning of the 4 panels see Figure 22.**

**Figure 30A) Co-spectrum of along wind (US47) and vertical wind (WS47)**

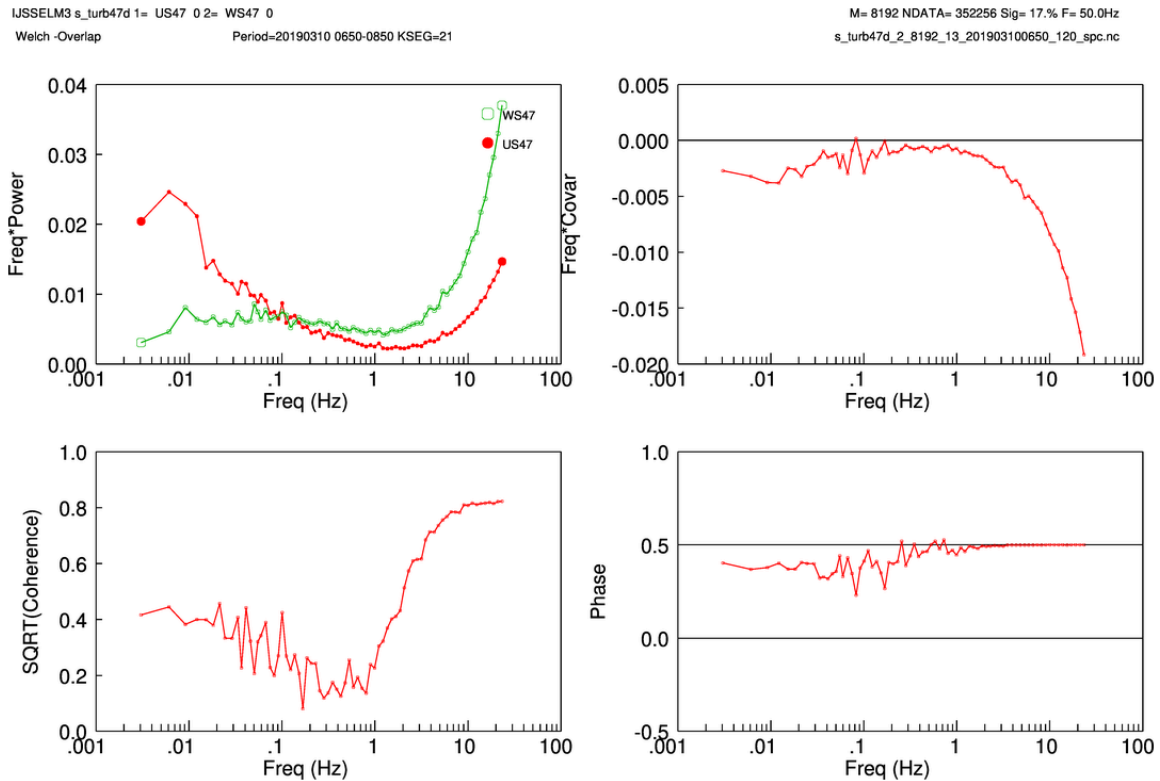
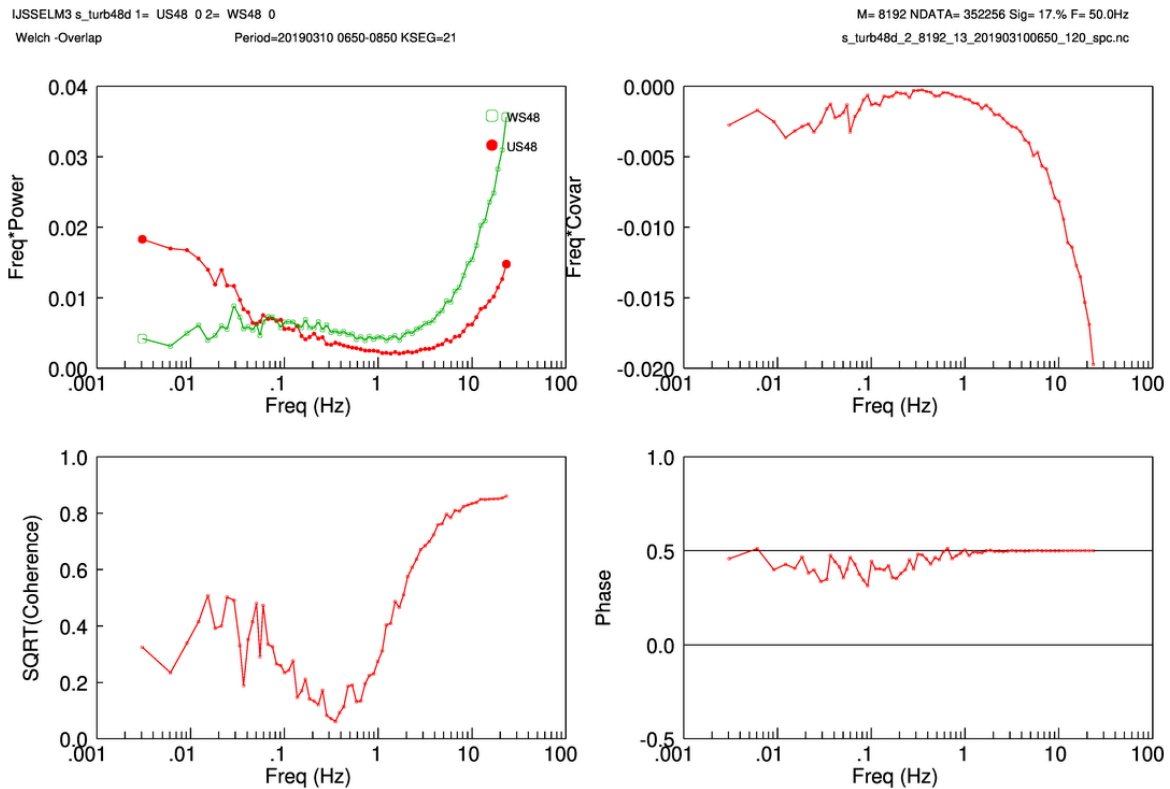


**Figure 30B) Co-spectrum of along wind (US48) and vertical wind (WS48)**



20161120 IJSSELM3.B10

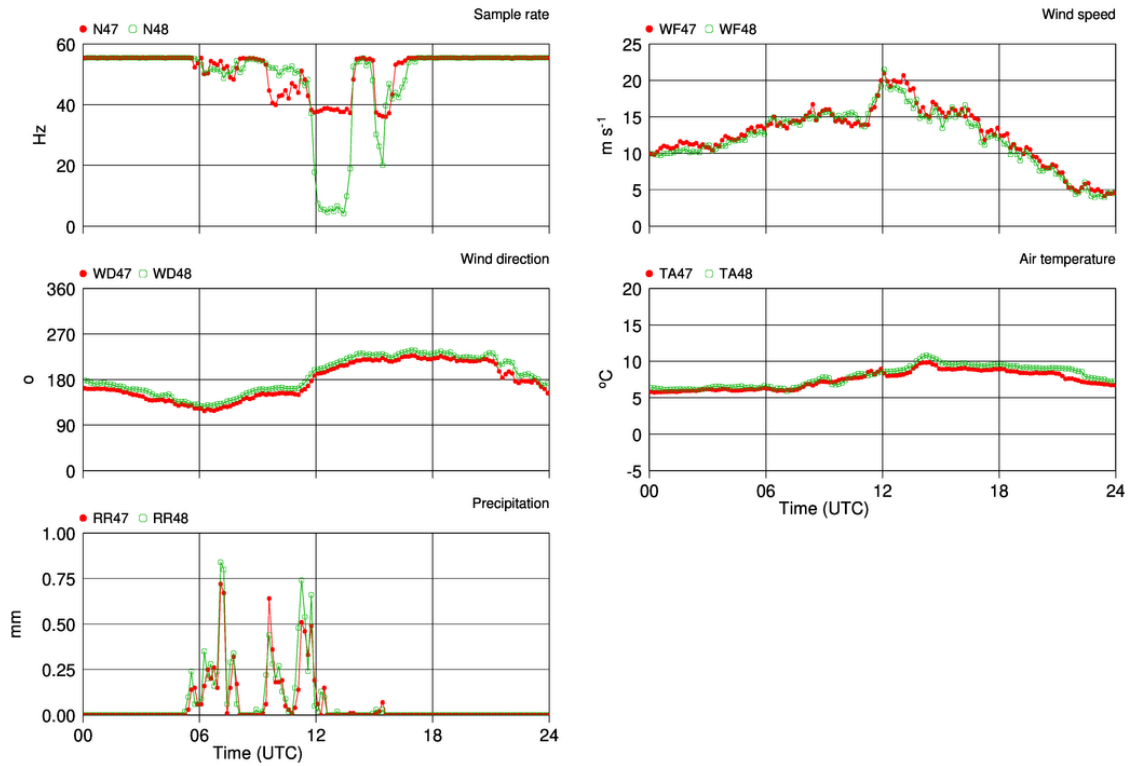


**Figure 31** 10 minute values for sampling rate (upper-left), and meteo: wind speed (upper right); wind direction (middle left), temperature (middle right) and rain rate (lower left) for FL47 and FL48 for the storm day 20-nov-2016.

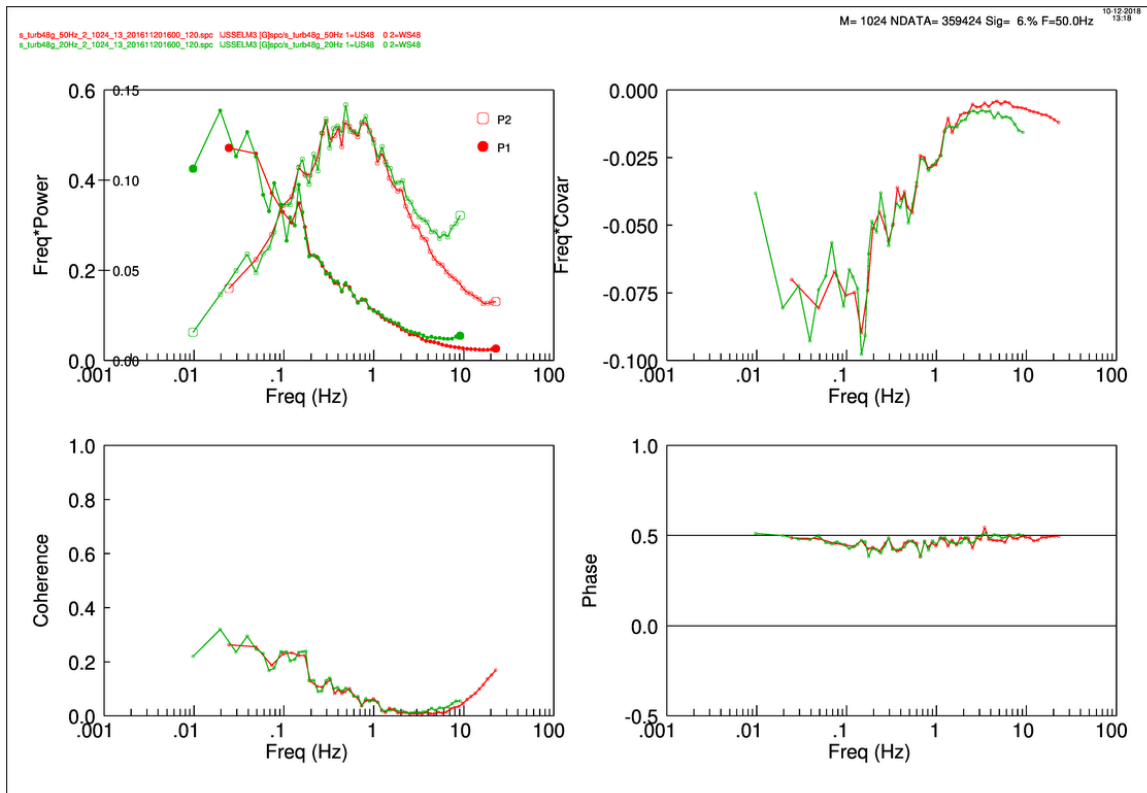


Figure 32 Full spectral information of  $u$  and  $w$  for the 120 minute period 20-Nov-2016 16:00-18:00 UTC when vibration intensity is small. Spectra are based on 50 and 20 Hz resampling. 50 Hz data are in red, 20 Hz data are in green. In the power spectrum plot (left upper panel)  $u$ -data are denoted by closed symbols and the y-scale is on the outer side of the data plotting area,  $w$ -data are denoted by open symbols and the y-scale is on the inner side of the data plotting area.

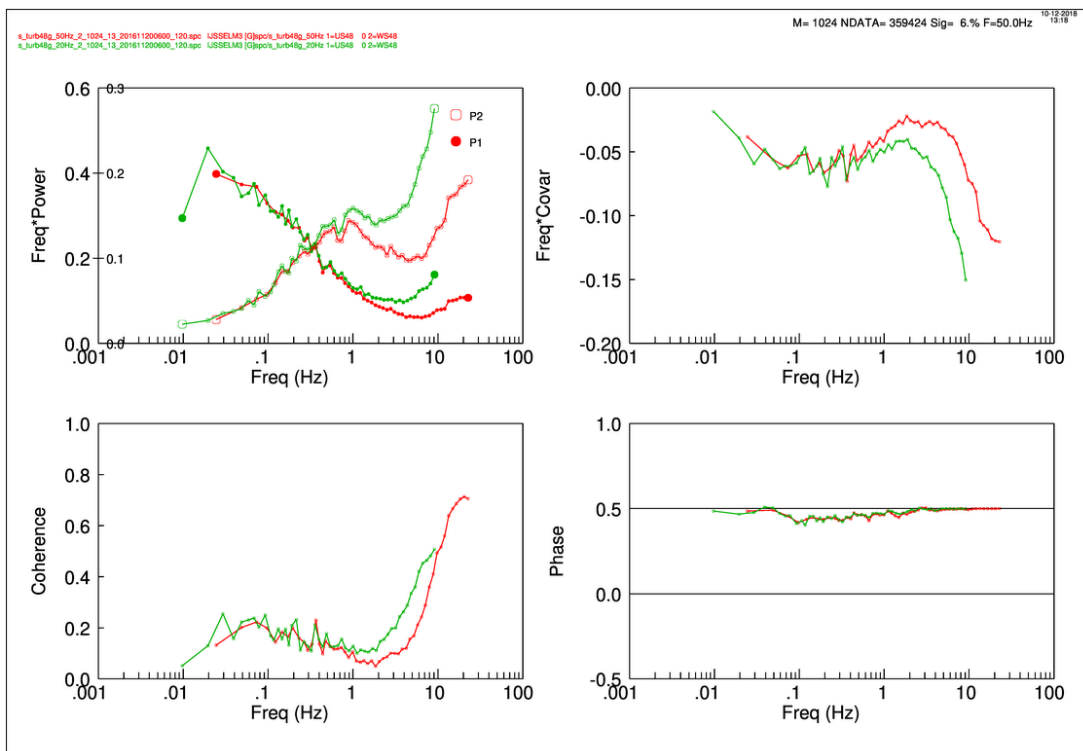


Figure 33 Full spectral information of  $u$  and  $w$  for the 120 minute period 20-Nov-2016 06:00-08:00 UTC when vibration intensity is large. For further explanation see Figure 32

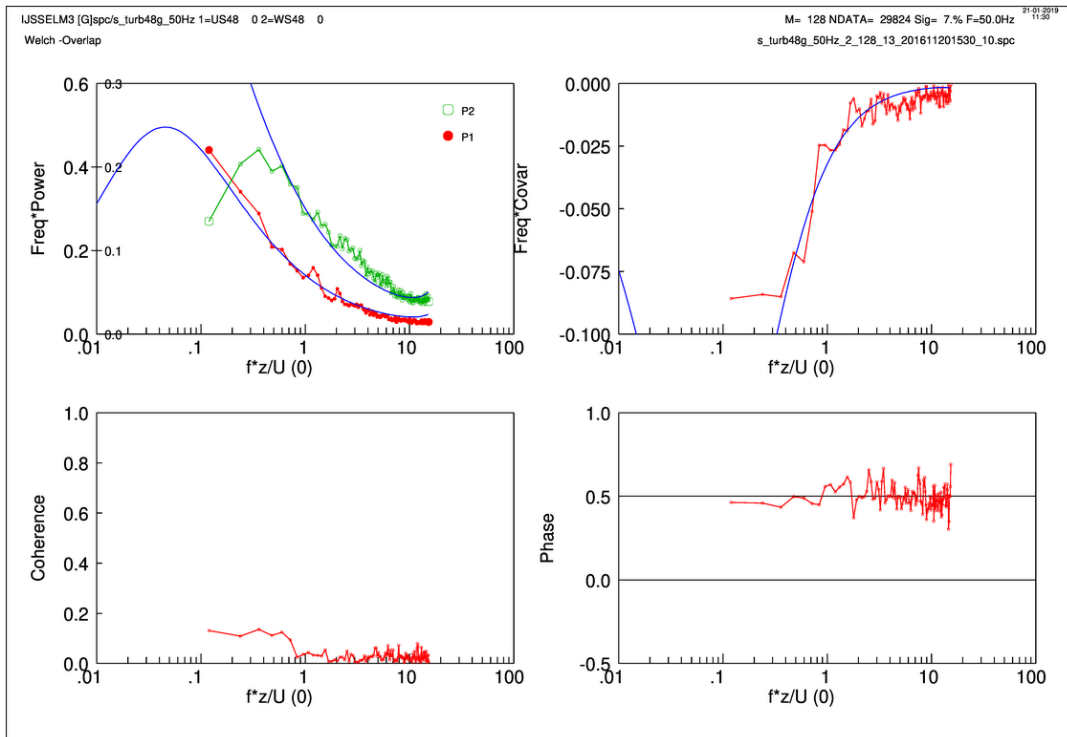


Figure 34 Full spectra information for the period 20-Nov-2016 15:30-15:40 UTC with short segment size and 50 Hz resampling. The frequency axis is normalized. Also shown are Kaimal spectra which are fitted to the observed spectral values in the range  $n=[0.5:1.0]$ . The influence of vibration is very small.

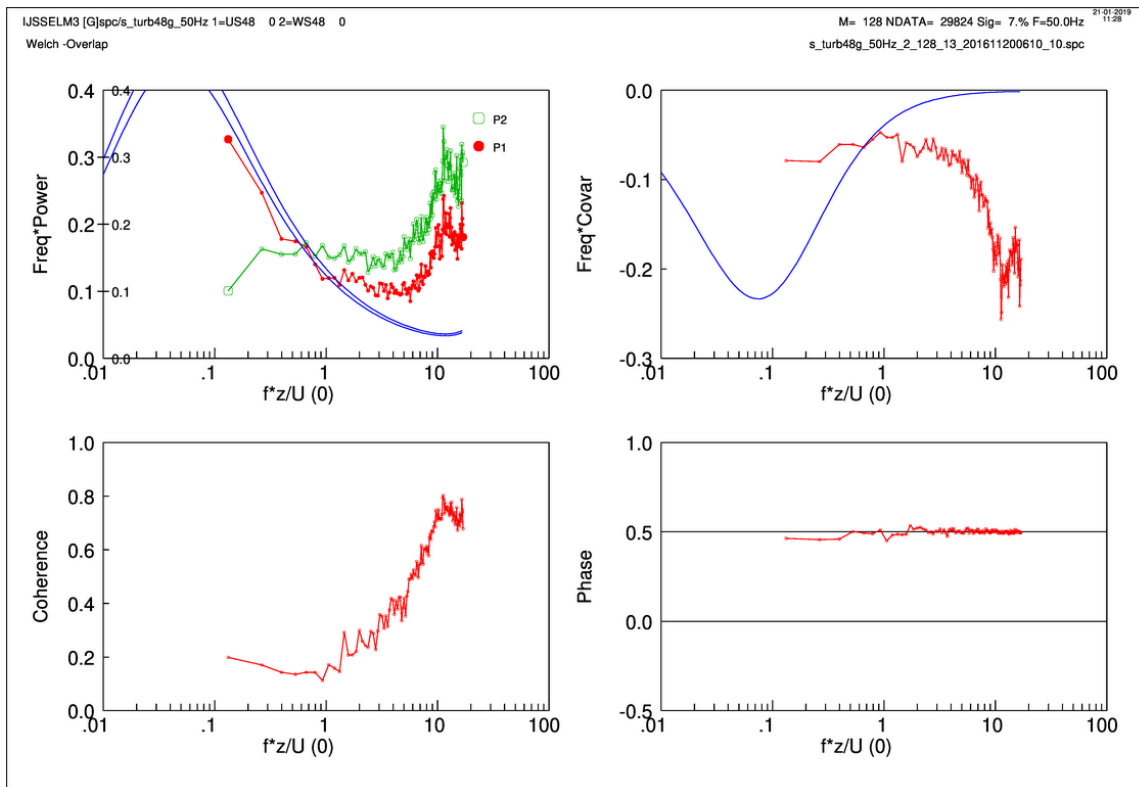


Figure 35 Full spectra information for the period 20-Nov-2016 06:10-06:20 UTC with short segment size and 50 Hz resampling. The frequency axis is normalized. Also shown are Kaimal spectra which are fitted to the observed spectral values in the range  $n=[0.5:1.0]$ . The influence of vibration is large.

## Corrections to friction velocity

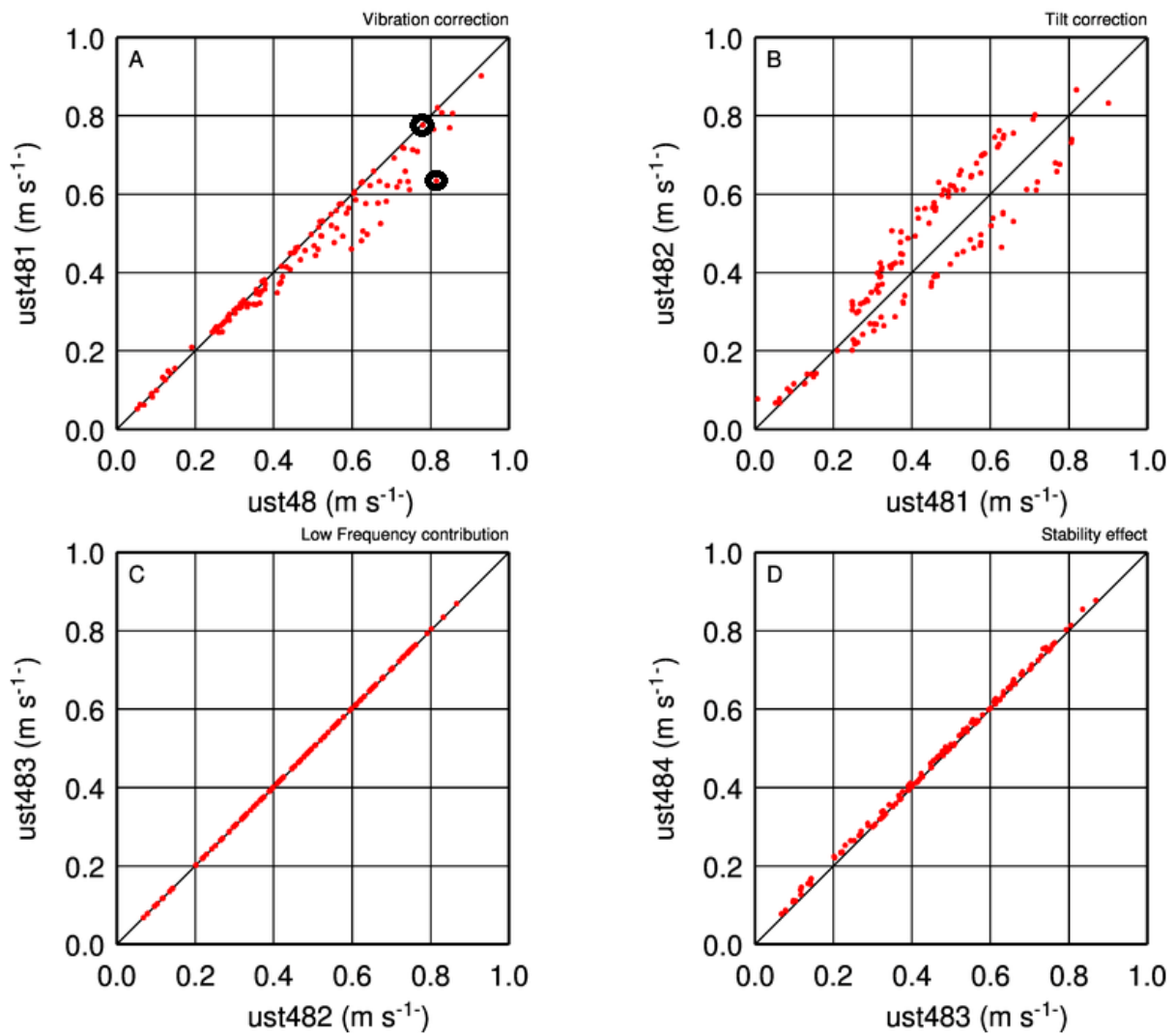


Figure 36 Incremental effects of corrections on the observed friction velocity at FL48 for the storm of 20-Nov-2016. UST48 is uncorrected friction velocity, (Panel A) UST481 after vibration correction, the two encircled points are discussed in the main text, (Panel B) UST482 after tilt correction, (Panel C) UST483 after low frequency correction, and (Panel D) UST484 after accounting for stability effects.

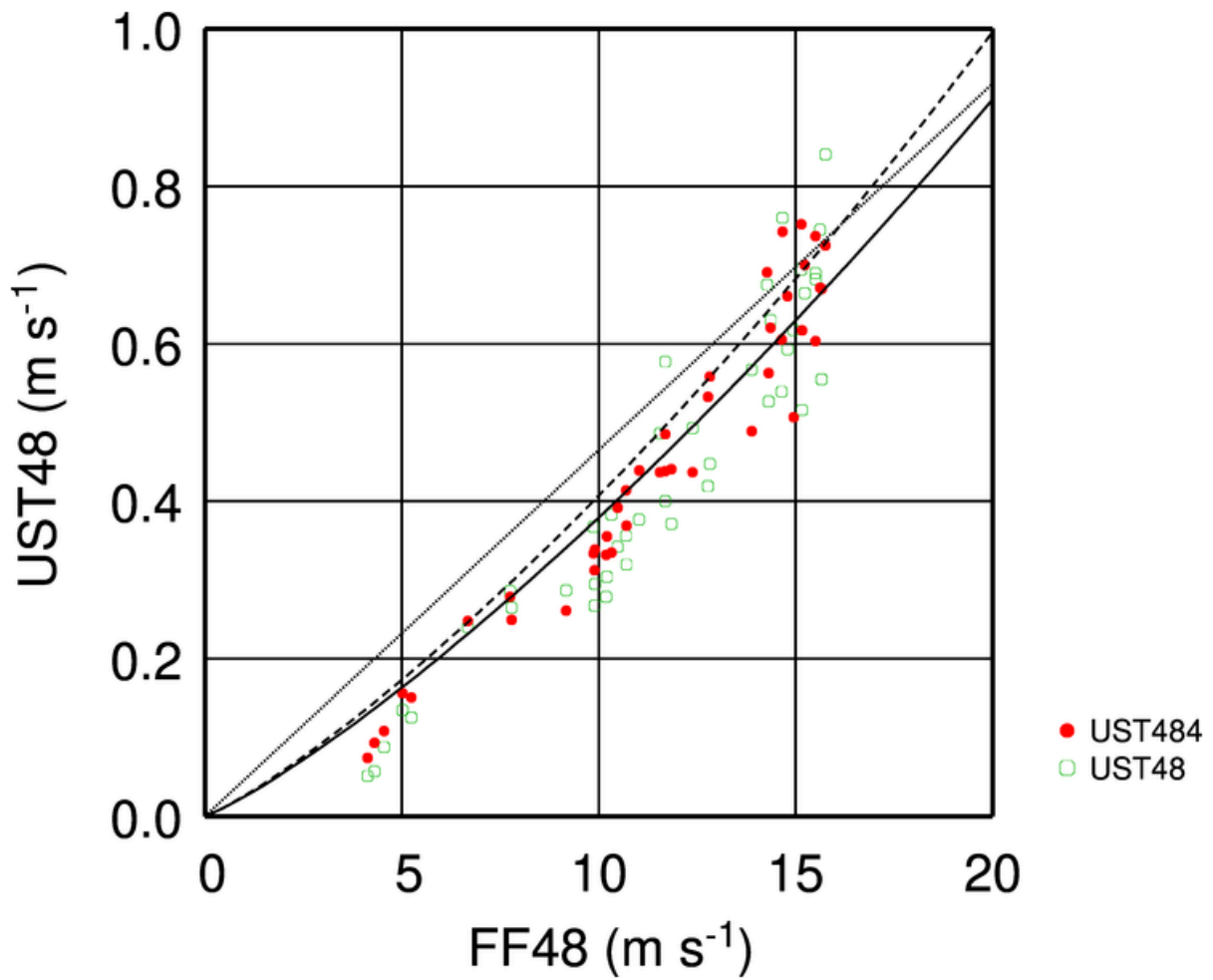
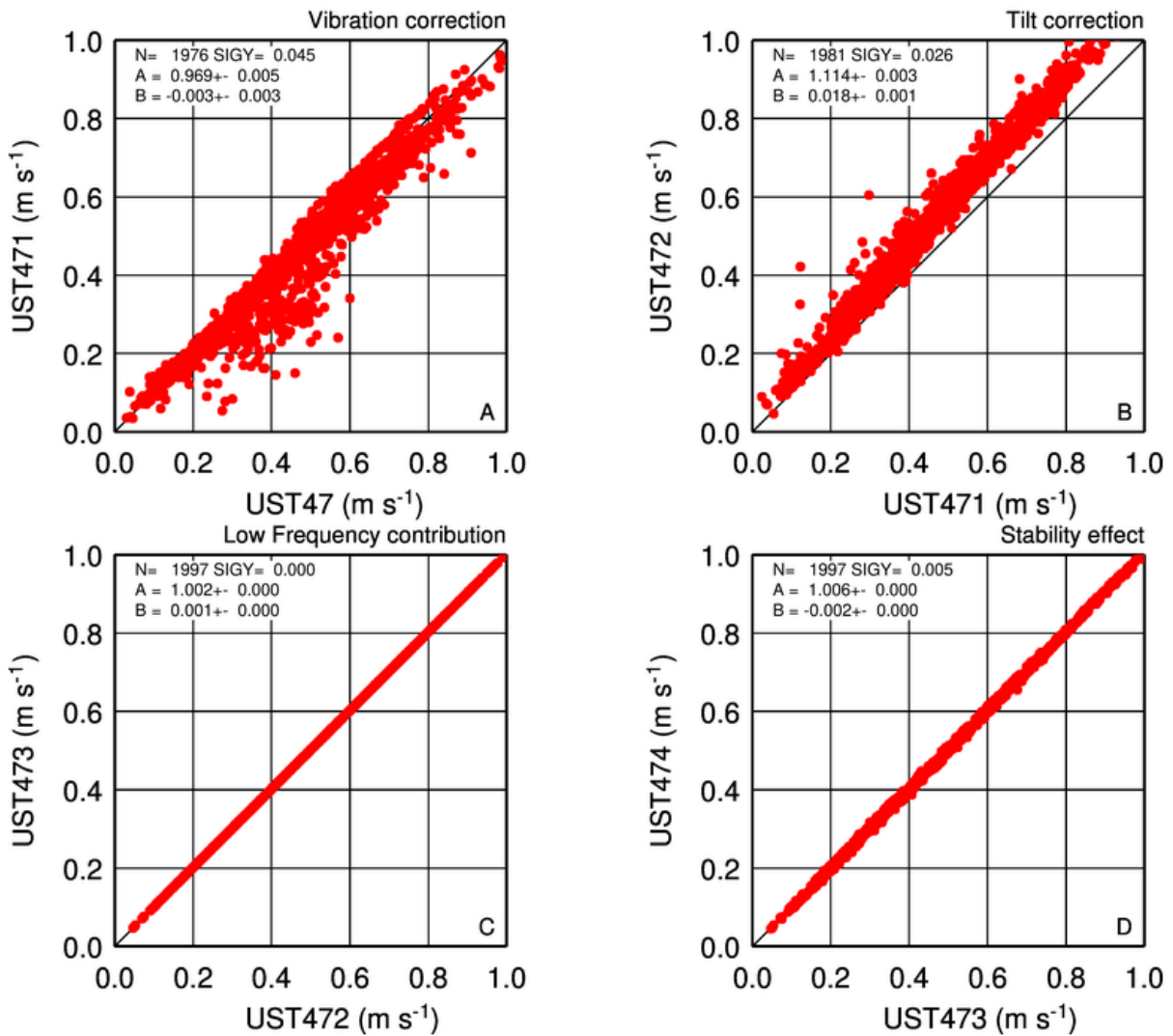


Figure 37 30 minute friction velocity as function of wind speed for FL48 during the storm day 20161120. (green dots) Uncorrected and (red dots) all corrections applied. (solid line) Theoretical relation derived from the Charnock relation ( $\alpha_c=0.018$ ) with assumed neutral conditions. (dashed line) Same but with  $\alpha_c=0.032$ . (dotted line) Theoretical relation with roughness length constant at 1.8 mm, corresponding to surface roughness of water at  $u^*=1$  m/s according to Charnock relation.

## Corrections to friction velocity



**Figure 38** Incremental effects of corrections on the observed friction velocity at FL47 for the period 20190304-20190317. UST47 is uncorrected friction velocity, (Panel A) UST471 after vibration correction, (Panel B) UST472 after tilt correction, (Panel C) UST473 after low frequency correction, and (Panel D) UST474 after accounting for stability effects.

## Corrections to friction velocity

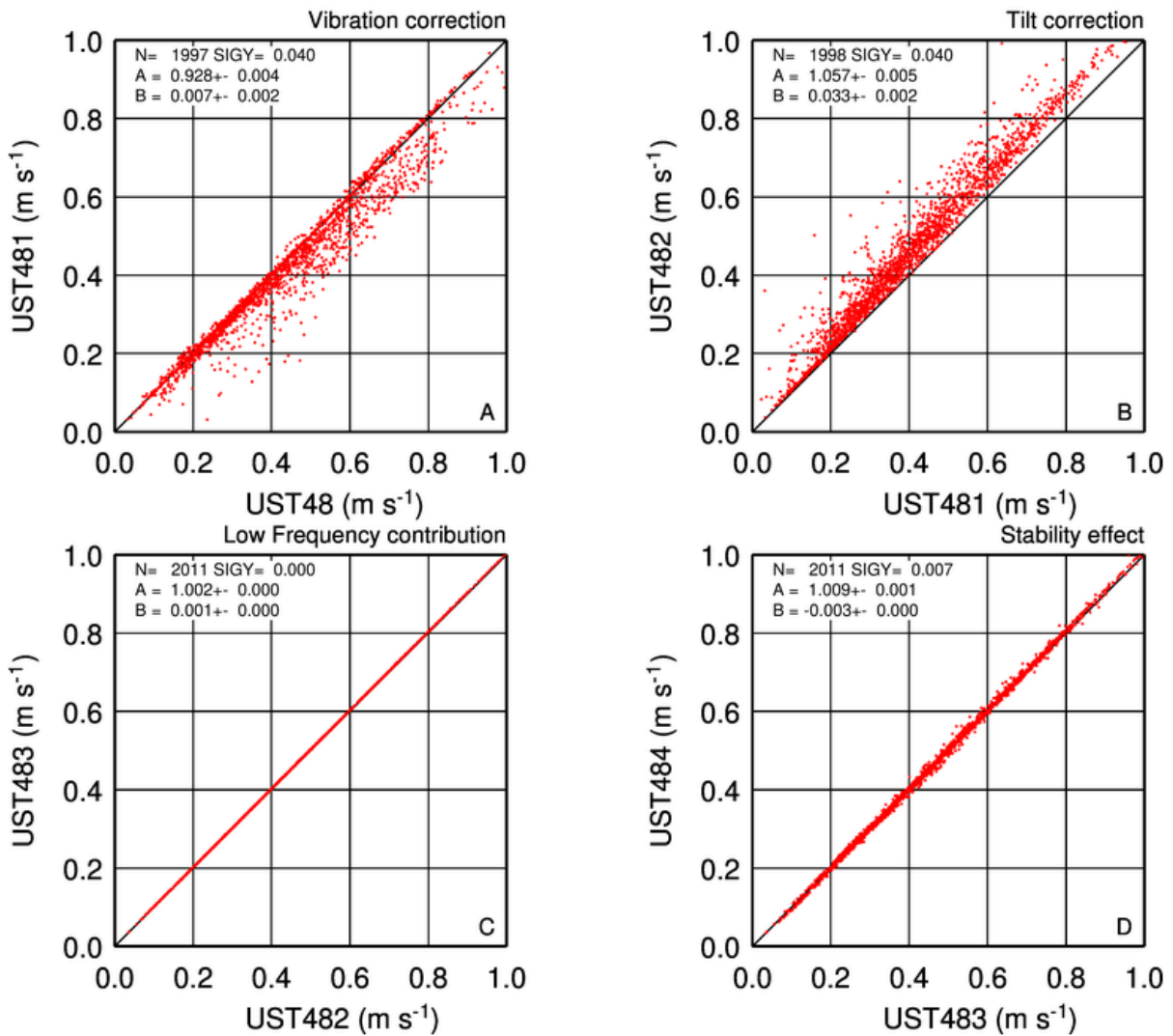


**Figure 39** Incremental effects of corrections on the observed friction velocity at FL48 for the period 20190304-20190317. UST48 is uncorrected friction velocity, (Panel A) UST481 after vibration correction (Panel B) UST482 after tilt correction, (Panel C) UST483 after low frequency correction, and (Panel D) UST484 after accounting for stability effects.

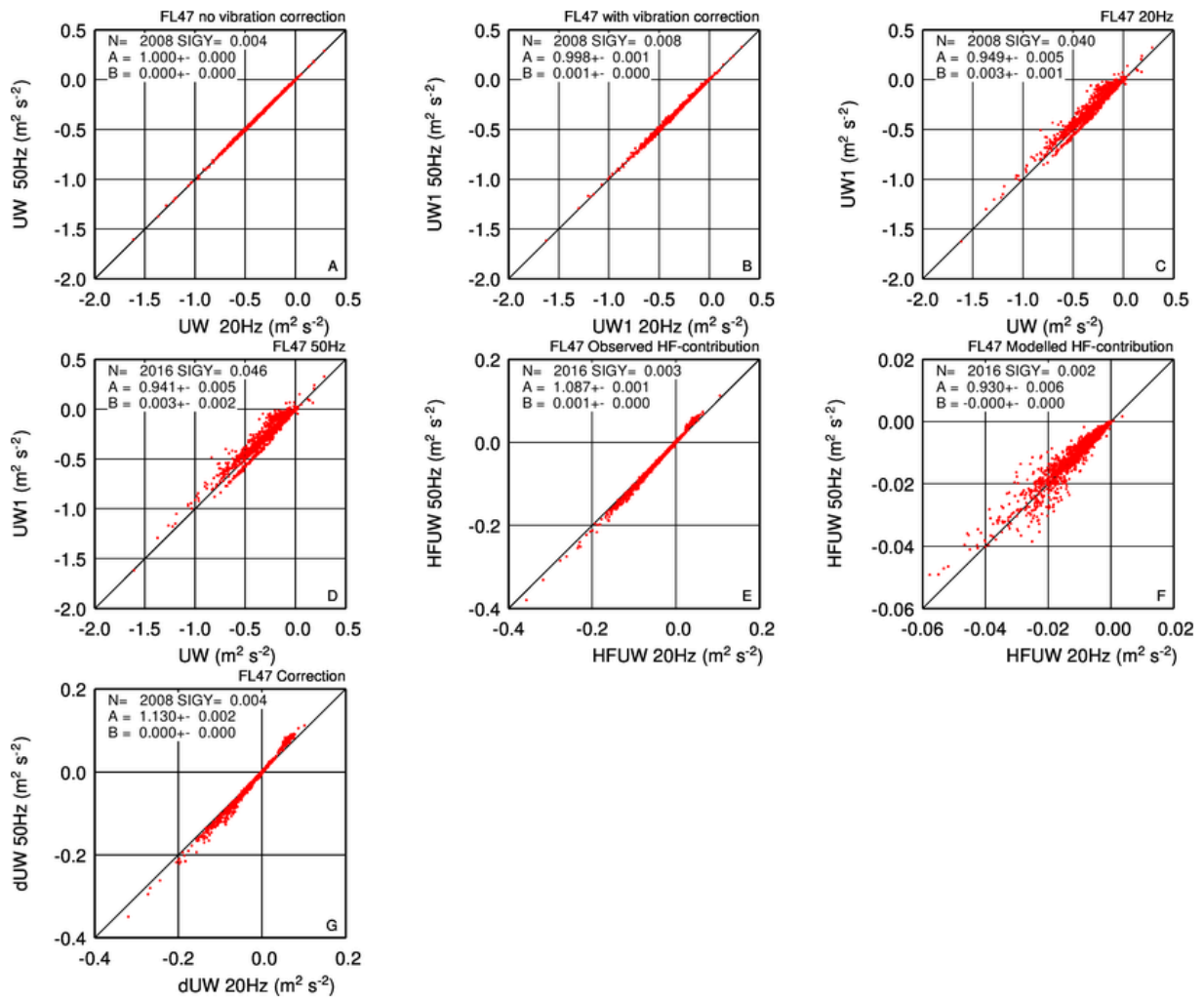


Figure 40 FL47 comparison of stress vibration corrections based on 20 Hz and 50 Hz resampled data for the period 20190304-20190317. (A) Uncorrected 50 Hz versus uncorrected 20 Hz; (B) Corrected 50 Hz versus corrected 20 Hz; (C) Corrected versus uncorrected for 20 Hz; (D) Corrected versus uncorrected for 50 Hz; (E) Observed high frequency contribution, including vibration, 50 Hz versus 20 Hz; (F) Modelled high frequency contribution as expected without vibration, 50 Hz versus 20 Hz; (G) Vibration correction, i.e. Observed minus Modelled HF contribution, 50 Hz versus 20 Hz.

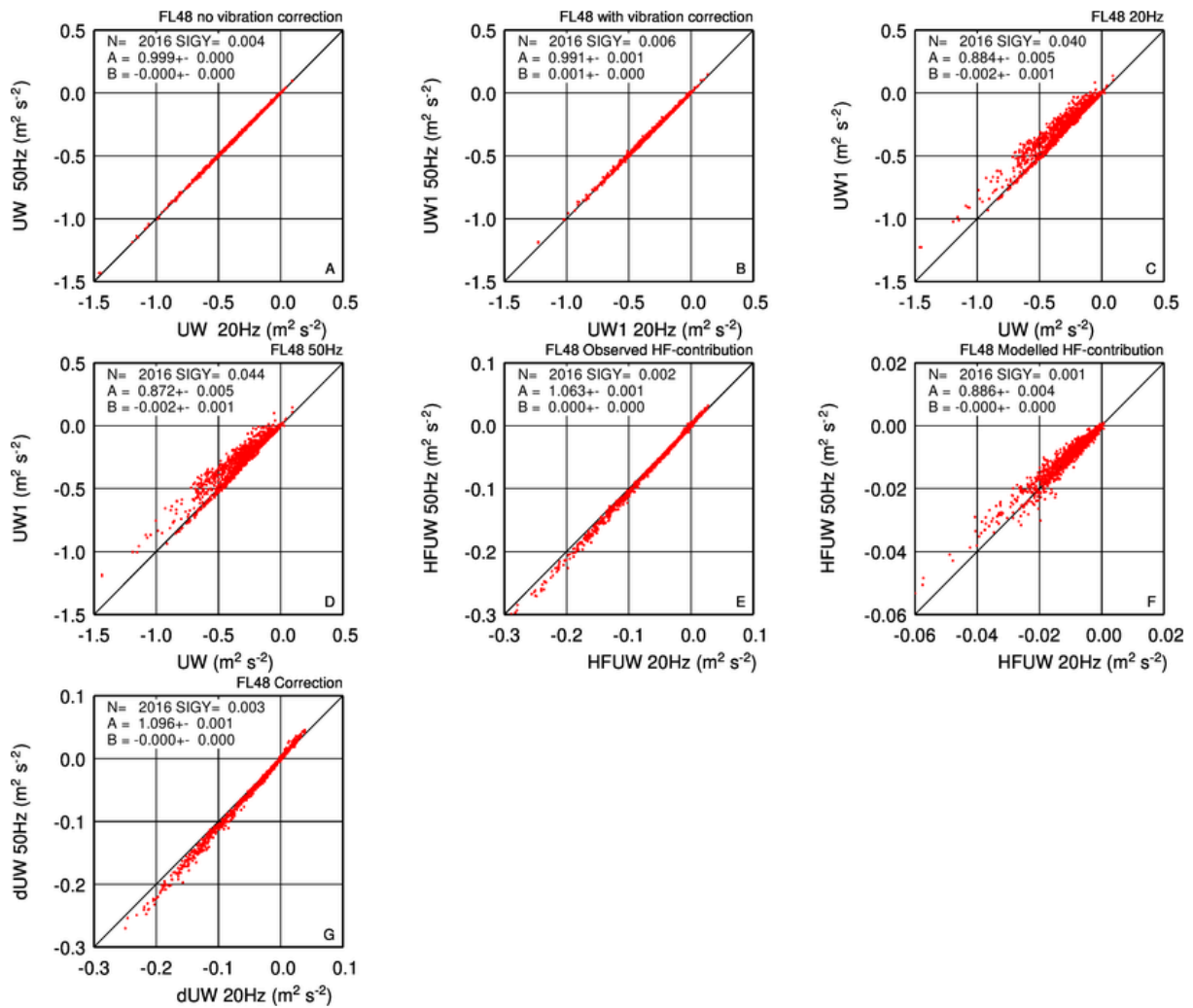


Figure 41 FL48 comparison of stress vibration corrections based on 20 Hz and 50 Hz resampled data for the period 20190304-20190317. (A) Uncorrected 50 Hz versus uncorrected 20 Hz; (B) Corrected 50 Hz versus corrected 20 Hz; (C) Corrected versus uncorrected for 20 Hz; (D) Corrected versus uncorrected for 50 Hz; (E) Observed high frequency contribution, including vibration, 50 Hz versus 20 Hz; (F) Modelled high frequency contribution as expected without vibration, 50 Hz versus 20 Hz; (G) Vibration correction, i.e. Observed minus Modelled HF contribution, 50 Hz versus 20 Hz.

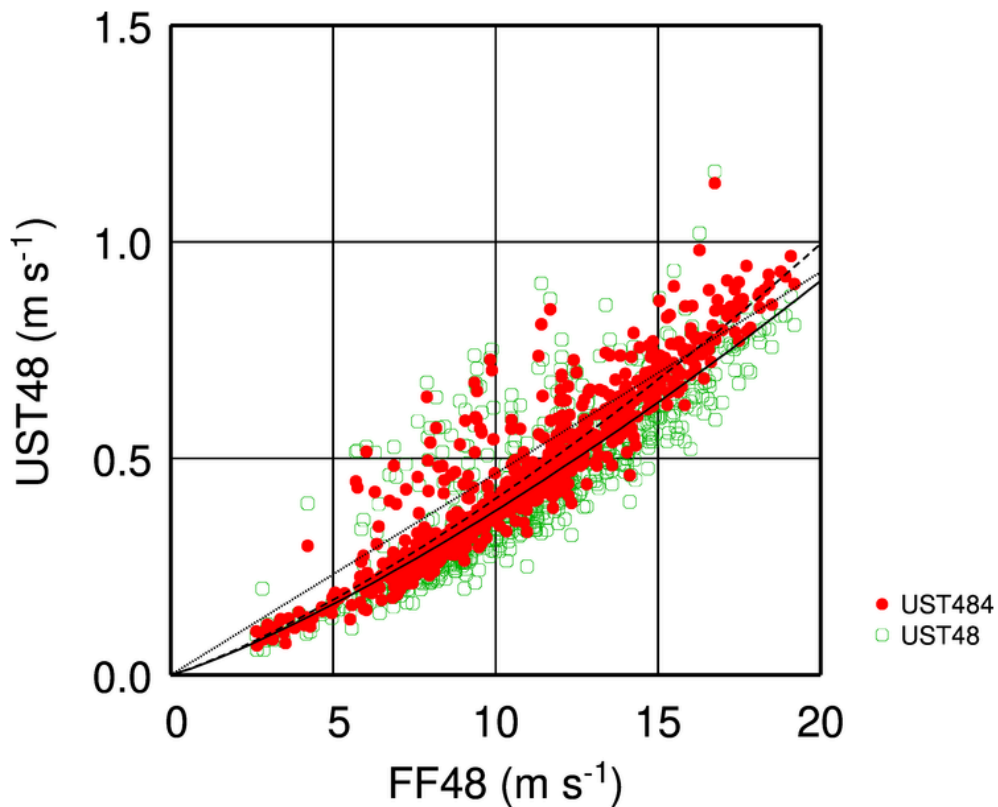
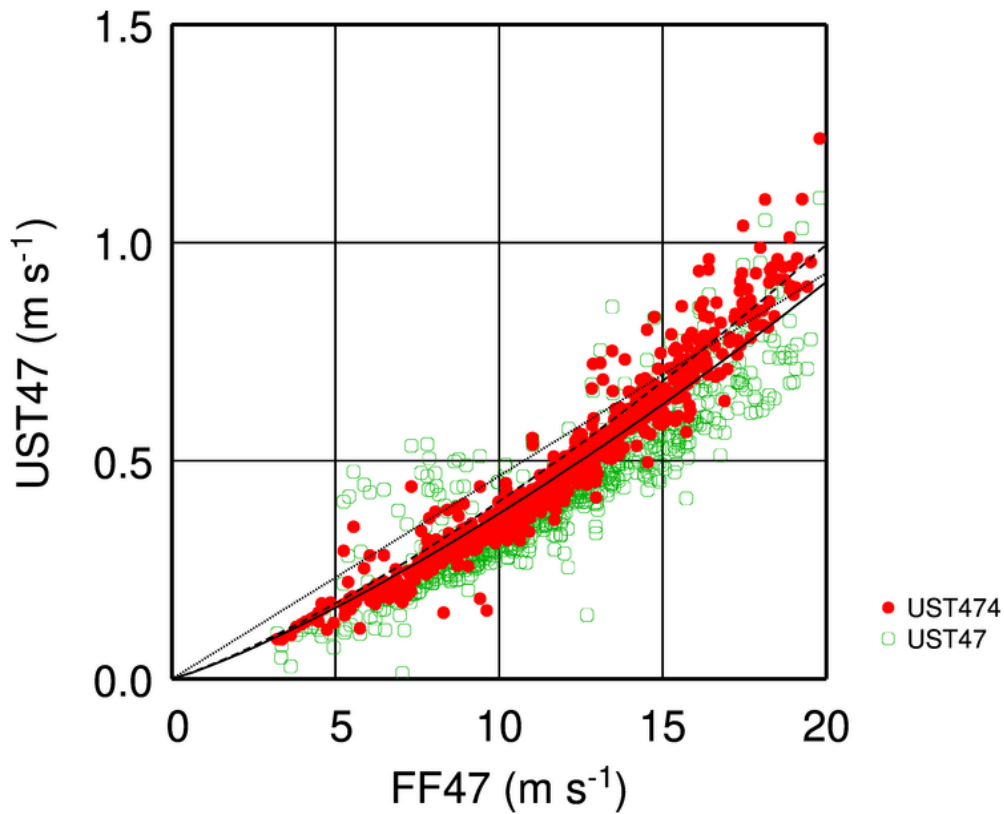


Figure 42 30 minute friction velocity as function of wind speed for FL47 (upper panel) and FL48 (lower panel) for the period 20190304-20190317. (green dots) Uncorrected data and (red dots) all corrections applied. (solid line) Theoretical relation derived from the Charnock relation ( $\alpha_c=0.018$ ) with assumed neutral conditions. (dashed line) Same but with  $\alpha_c=0.032$ . (dotted line) Theoretical relation with roughness length constant at 1.8 mm, corresponding to surface roughness of water at  $u^*=1$  m/s according to Charnock relation.

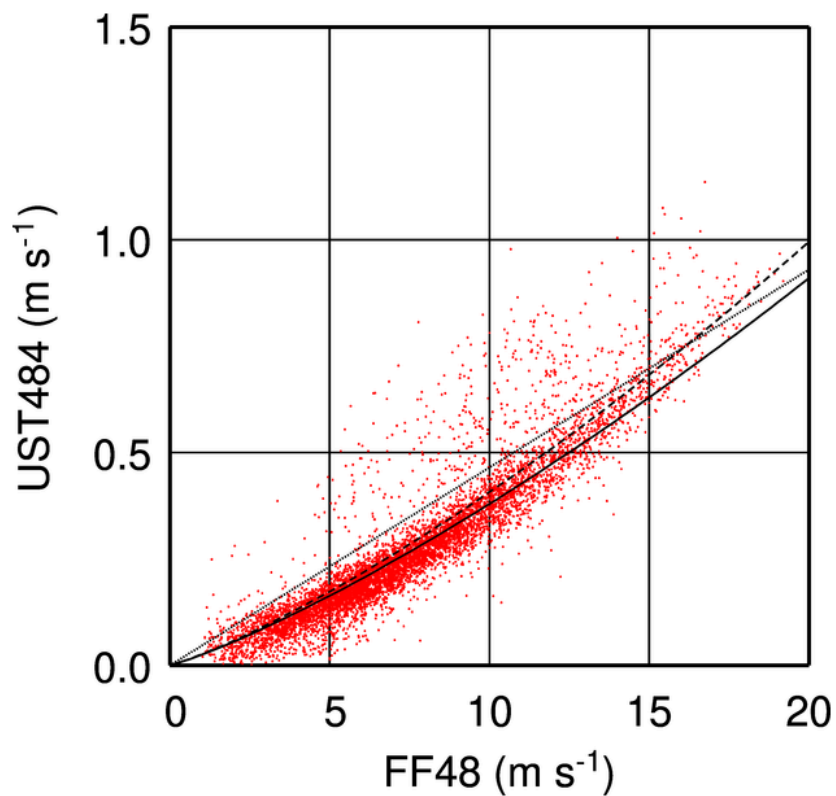
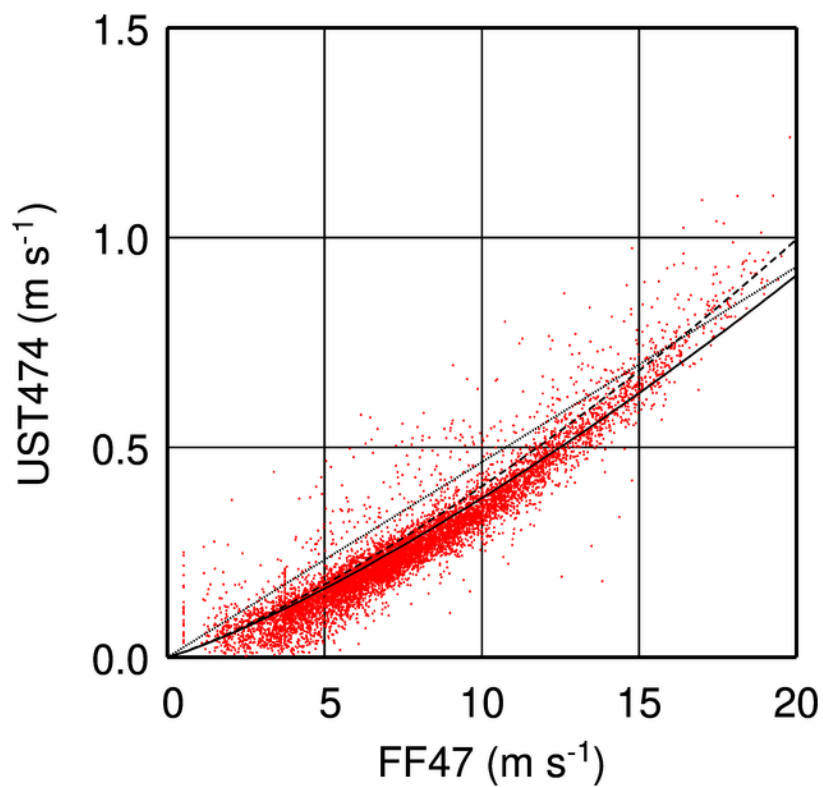


Figure 43 30 minute friction velocity fully corrected as function of wind speed for FL47 (upper panel) and FL48 (lower panel) for the full period 20181114-20190617. (solid line) Theoretical relation derived from the Charnock relation ( $\alpha_c=0.018$ ) with assumed neutral conditions. (dashed line) Same but with  $\alpha_c=0.032$ . (dotted line) Theoretical relation with roughness length constant at 1.8 mm, corresponding to surface roughness of water at  $u^*=1$  m/s according to Charnock relation.

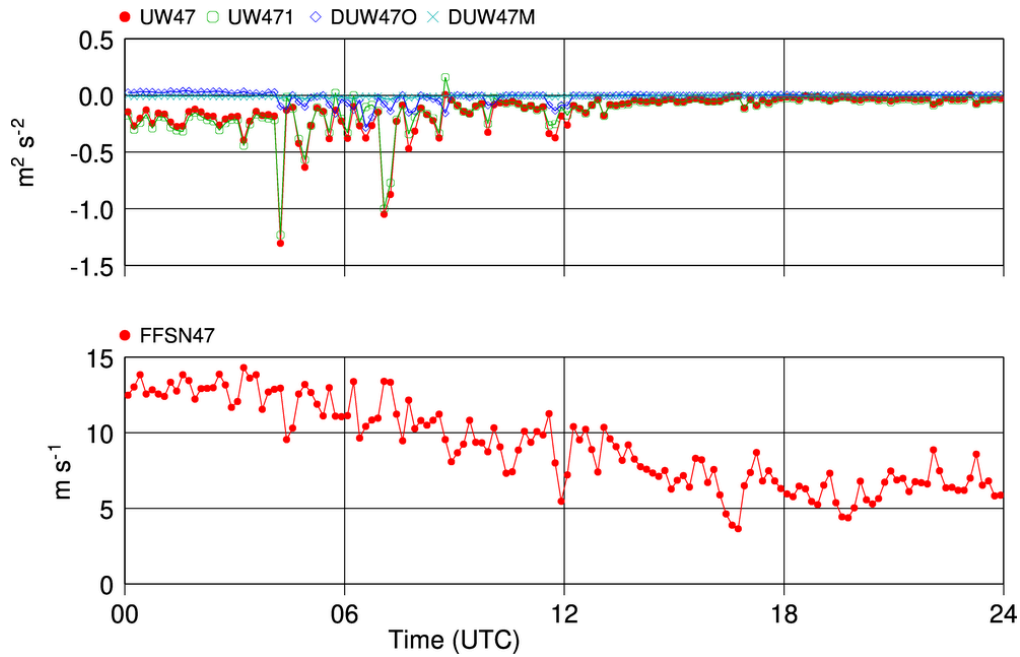


Figure 44 10 min. stress (upper panel) and wind speed (Lower panel) for 20190102 at FL47. Shown in upper panel are uncorrected stress (UW47), stress with vibration correction (UW471), contribution of vibration (DUW47O), and modelled high-frequency contribution.

IJSSELM3 20190102 0700-0710

s\_flux\_uw.ctr

04-08-2021  
15:28

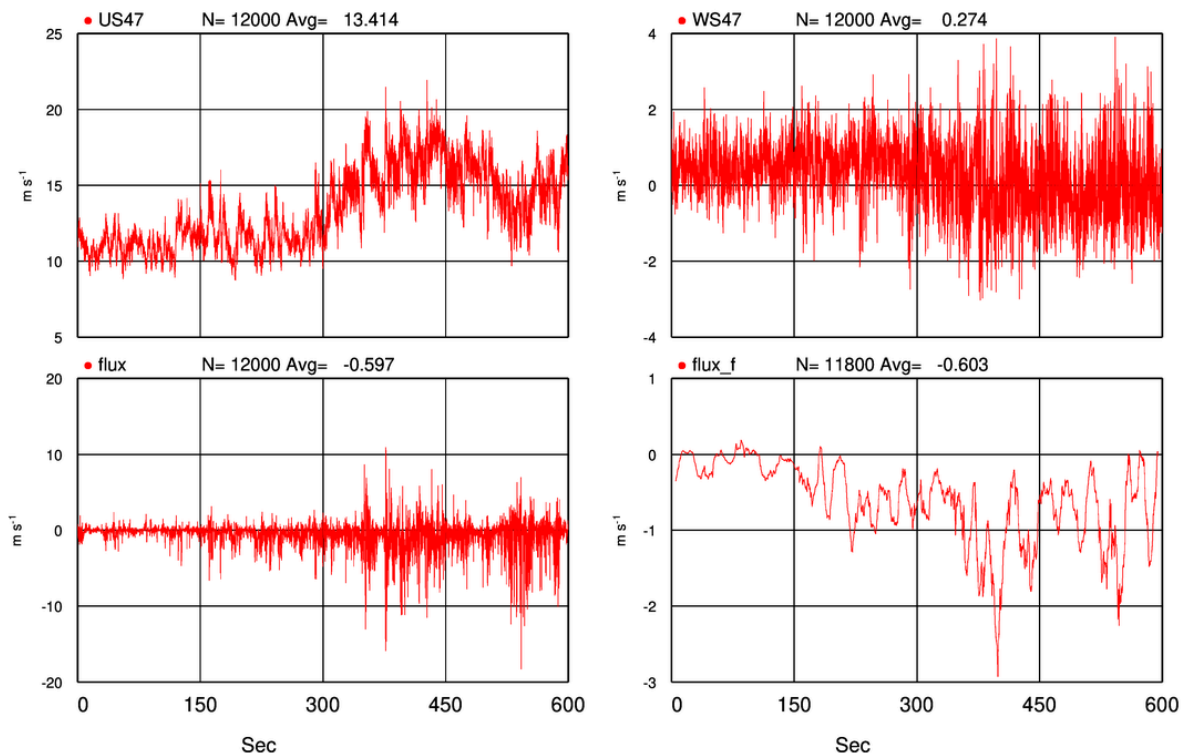


Figure 45 20Hz sample data for a 10 minute period starting at 20190102 0700 UTC. (Upper left panel) Along mean wind horizontal wind speed, (upper right panel) vertical wind speed, (lower left panel) product of horizontal and vertical wind after subtraction of mean values, and (lower right panel) as previous panel but with a 10 sec. block average low pass filter applied, clearly showing the contribution to the stress during the entire 10 min. period.

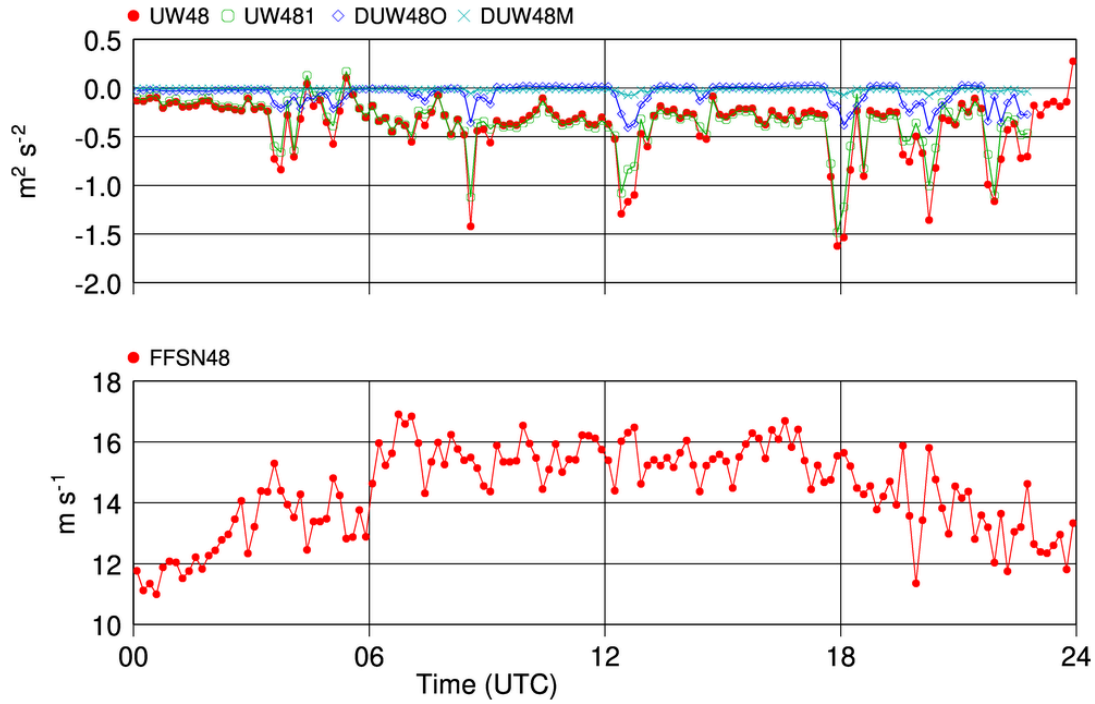


Figure 46 As Figure 44 but for the period 20190108 at FL48.

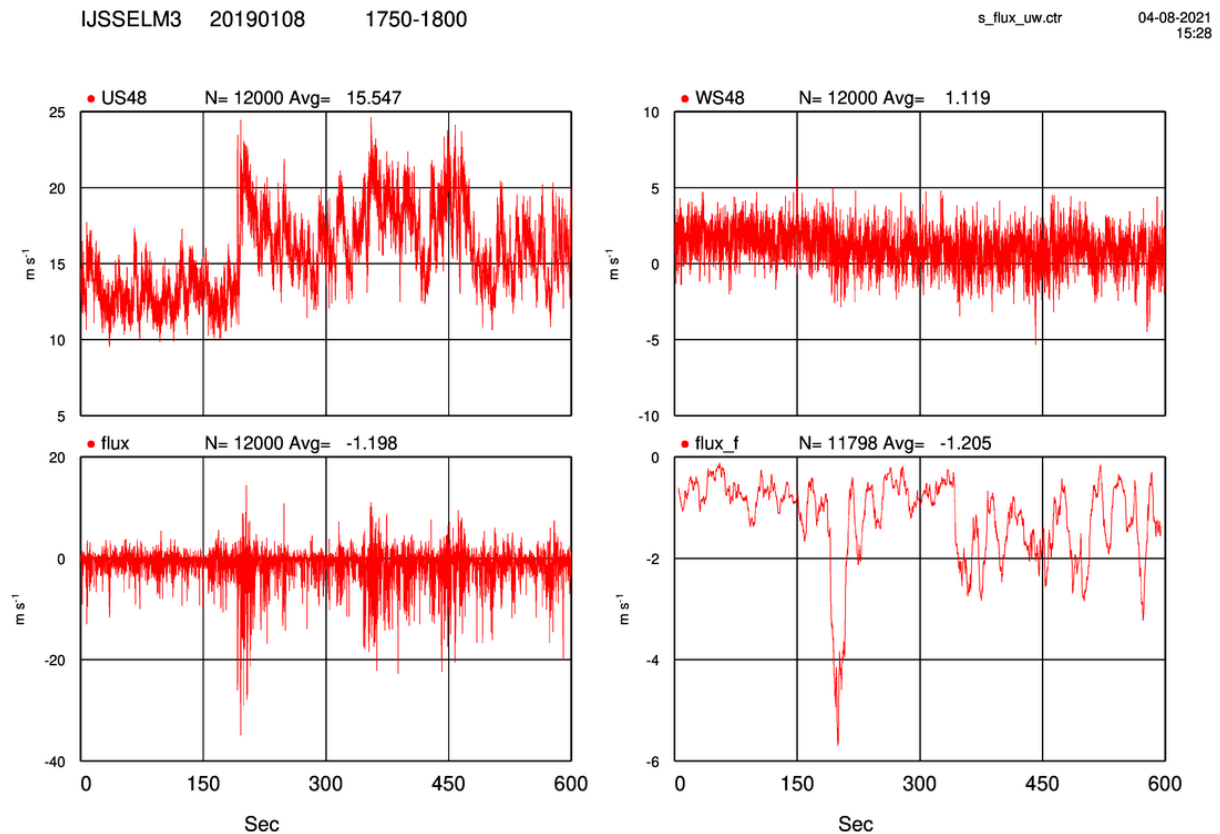


Figure 47 As Figure 45 but for the 10 min. period starting at 20190108 1750 UTC at FL48.

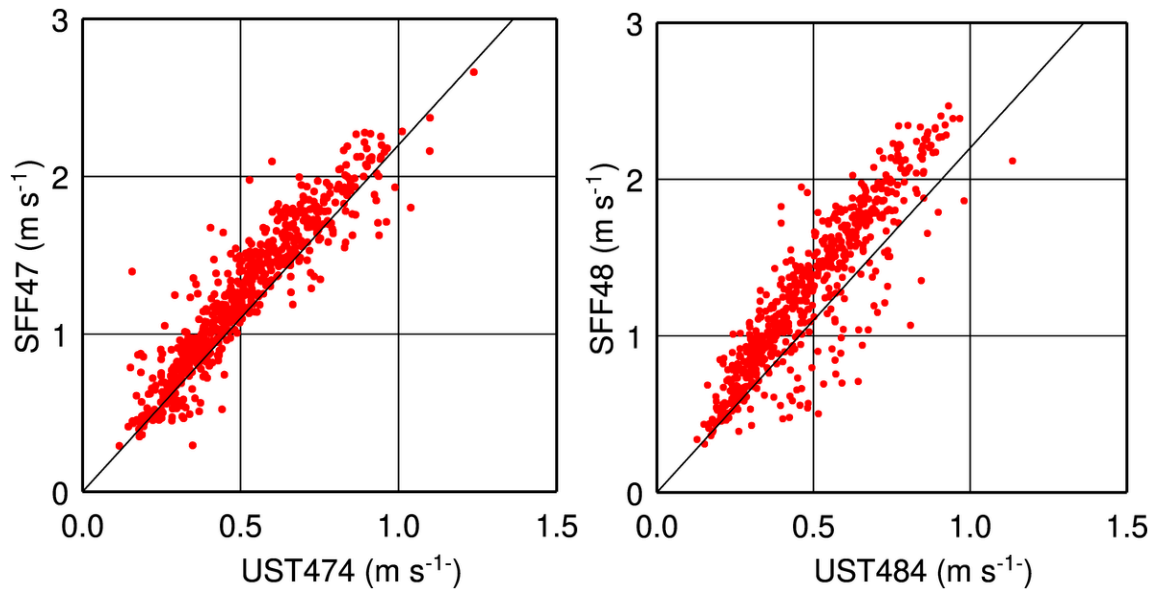


Figure 48 30 min. based standard deviation of horizontal wind (SFF) as function of friction velocity (UST) for the period 20190304-20190317 at FL47 (Left Panel) and FL48 (Right Panel). Data are selected on windspeeds larger than 5 m/s. The straight lines are the expected neutral values according to the literature (factor 2.2).

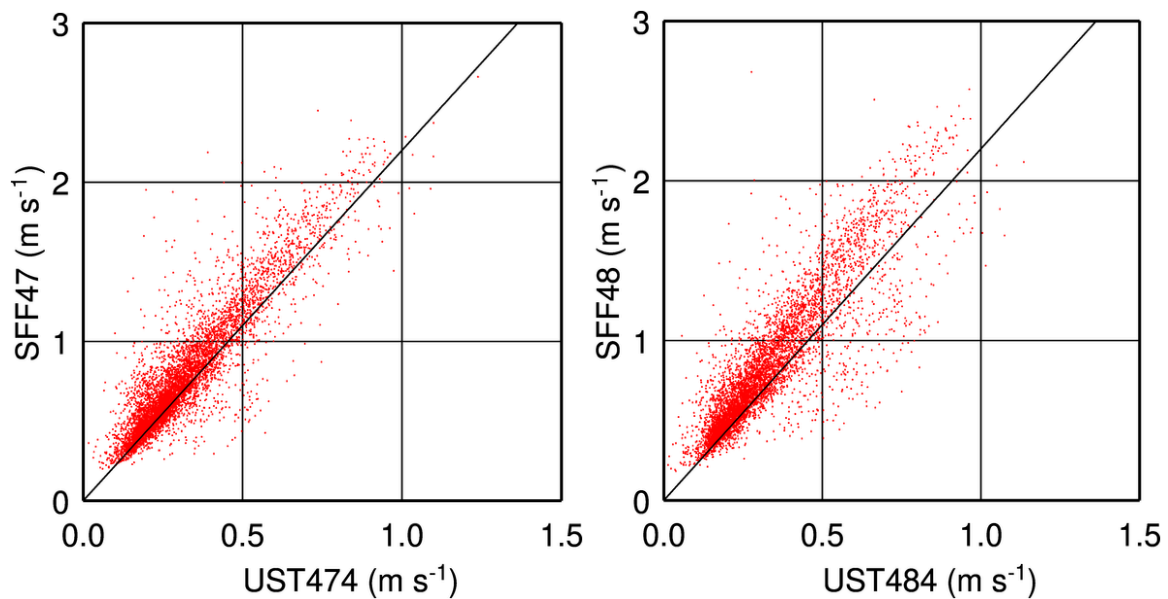


Figure 49 30 min. based standard deviation of horizontal wind (SFF) as function of friction velocity (UST) for the full period 201811-201906 at FL47 (Left Panel) and FL48 (Right Panel). Data are selected on windspeeds larger than 5 m/s. The straight lines are the expected neutral values according to the literature (factor 2.2).

## Appendix A: Working and configuration of the Thies 3D UltraSonic Anemometer

---

---

Manual Ch2 introduction:

The Ultra sonic Anemometer 3D consists of 6 ultrasonic transformers, in pairs facing each other at a distance of 200 mm. The three resulting measurement paths are vertical in relation to each other. The transformers function both as acoustic transmitters and receivers.

The electronic control system is used to select the respective measurement path and its measuring direction. When a measurement starts, a sequence of 6 individual measurements is performed in all 6 directions of the measurement paths in a pre-selectable timing cycle.

The measurement directions (sound propagation directions) rotate clockwise (looking from above), firstly from top to bottom and then from bottom to top.

The mean values are worked out from the 6 individual measurements of the path directions depending on the measuring speed and output rate selected and used to make further calculations.

The time required for a measuring sequence is approx.. 3.5 m sec at +20°C. with the maximum measuring speed, which is only limited by the sound velocity over the measurement paths.

---

---

Is this indeed pre-selectable, or is it fixed.

The travel time of sound (343 m/s at 20 °C) over a 200 mm path is 0.583 ms. Times 6 paths gives indeed 3.499 ms.

---

---

Manual Ch7.3 Data acquisition

The main function of the ULTRASONIC firmware is data acquisition and preparation. For data acquisition sound impulses are transmitted by the sensors in a clockwise direction and received by the sensor opposite. The propagation time measured is a measure of the velocity. A measuring cycle is complete when every sensor has performed transmit and receive once. The complete data record is then time-stamped and passed on to the next level. After the plausibility check the individual components are calculated and, depending on the setting, either output (see **Instantaneous values and output of raw measured values**) or written to the averaging buffer (see **Averaging**) prepared and output.

---

---

Can this time-stamp be outputted?

Plausibility check is important, what happens when a cycle does not pass this test?

---

---

Ch 7.3.1 Instantaneous values and output of raw measured values

The output of instantaneous values is generally a special case. Due to the high acquisition speed of the measured values averaging of the data is sensible in most cases. If instantaneous values are to be output, averaging must not be switched on. The parameter AV should be set to '0', see **Command AV**.

The OR parameter is used to adjust the output rate with independent output. With a value '0 a telegram is output whenever a new measured values is determined. If the baud rate is set high enough and a short user-specific telegram is defined in this mode, the raw measured values of the ULTRASONIC can be output

## Appendix B Influence of frame deformation on sonical wind speed and temperature

Sonic wind speed ( $V$ ) and speed of sound ( $C$ ) along a transducer pair are calculated according to:

$$V = \frac{1}{2} \left( \frac{l}{t_d} - \frac{l}{t_u} \right); C = \frac{1}{2} \left( \frac{l}{t_d} + \frac{l}{t_u} \right) \quad ( 1 )$$

where  $t_+$  and  $t_-$  are the sound flight time downwind and upwind along the transducer path of length  $l$  respectively. Sonic temperature ( $T$ ) in Kelvin is given by:

$$T = \frac{C^2}{401}$$

when  $C$  is in m/s. If the path has a fixed distortion of  $\Delta l$  than the sound flight times become:

$$t_d = \frac{(l + \Delta l)}{C + V}; \quad t_u = \frac{(l + \Delta l)}{C - V}$$

substituting in Eq. 1 and using that  $|\Delta l/l| = |\alpha'| \ll 1$  we get for the resulting deviations in  $V$ ,  $\Delta V$ , and in  $C$ ,  $\Delta C$ , and in  $T$ ,  $\Delta T$ , to first order:

$$\Delta V = -V\alpha'; \quad \Delta C = -C\alpha'; \quad \Delta T = -2T\alpha'$$

respectively. Thus, when the transducer path is longer than assumed, wind speed, speed of sound, and sonic temperature will be underestimated proportional with the relative distortion of the path length.

As an example we take  $\alpha' = 0.01$ . This result in a (negative) wind speed bias of 1%, which for many applications will be sufficient. The resulting temperature deviation will be  $-6^\circ\text{C}$ . This makes clear that a comparison of measured sonic temperature and an independent air temperature measurement close to the sonic anemometer can give an indication of the integrity of the sonic transducer path length, and thus of the wind speed measurements.

Within the measurement cycle of the sonic anemometer there is a delay in time between the upwind and downwind measurements along a transducer path. For the Thies sonic anemometer this delay is 3.5 ms. If the length deviation is varying in time, the outcome of the measurements will be influenced by the fact that the length of the transducer path will be different during the upwind measurement and during the downwind measurement. If we now interpret  $l$  as the average of the length of the transducer paths  $1/2 \cdot (l_d + l_u)$  at the downwind ( $l_d$ ) and upwind ( $l_u$ ) measurement in a measurement cycle, and  $\Delta l$  as half of the path length difference  $1/2 \cdot (l_d - l_u)$  between these two moments in time we than have:

$$t_d = \frac{(l + \Delta l)}{C + V}; \quad t_u = \frac{(l - \Delta l)}{C - V}$$

Note that  $\Delta l$  can be negative. Using that  $|V|/C = |\beta| \ll 1$  and  $|\Delta l/l| = |\alpha| \ll 1$  (here without accent to discriminate from the static deformation coefficient), and substitute in Eq. 1 we have then:

$$V + \Delta V = \frac{C}{2} \left( \frac{1 + \beta}{1 + \alpha} - \frac{1 - \beta}{1 - \alpha} \right) = \frac{C}{2} \frac{(1 + \beta)(1 - \alpha) - (1 - \beta)(1 + \alpha)}{1 - \alpha^2}$$

$$C + \Delta C = \frac{C}{2} \left( \frac{1 + \beta}{1 + \alpha} + \frac{1 - \beta}{1 - \alpha} \right) = \frac{C}{2} \frac{(1 + \beta)(1 - \alpha) + (1 - \beta)(1 + \alpha)}{1 - \alpha^2}$$

and find:

$$V + \Delta V = \frac{C}{2} \frac{2(\beta - \alpha)}{1 - \alpha^2} = C(\beta - \alpha) \cdot (1 + \alpha^2 + O(4))$$

$$C + \Delta C = \frac{C}{2} \frac{2(1 - \alpha\beta)}{1 - \alpha^2} = C(1 - \alpha\beta)((1 + \alpha^2 + O(4)))$$

Here we used the Taylor expansion to second order:

$$\frac{1}{1 - \alpha^2} = 1 + \alpha^2 + O(4)$$

For the deviation in the windspeed the first order terms are dominant which result in:

$$\Delta V = -C\alpha$$

With the speed of sound as proportionality factor this means that the wind speed becomes quite sensitive to dynamic frame deformation. Especially if the deformation is significant at the time scale of the transducer cycle time of the sonic anemometer. which are.

For the deviation in the speed of sound the first order terms cancel and the second order terms become dominant:

$$\Delta C = C(\alpha^2 - \beta\alpha)$$

$$\Delta T = 2T(\alpha^2 - \beta\alpha)$$

this shows that dynamic deformation effects will be smaller than static effects. Whether one of the two terms in the latter two results can be neglected depends on the ratio of  $\beta$  and  $\alpha$ . Especially at high wind speed the second term may dominate over the first term.

It is clear that for the wind speed deviations the dynamic deformation effects can be much larger than the static effect, and thus the cycle times will have an important effect on the result. For temperature the static effect is always much larger.

The frequency of frame vibration play a significant role. We can represent the variation of the path length for a harmonic vibrating frame by  $\Delta l \sin(\omega t)$ . From this we can derive the path length difference between upwind and downwind in the measurement cycle as  $\alpha(t) \cdot \Delta l = \omega \tau \cdot \Delta l \cos(\omega t)$ , where  $\tau$  is the cycle time between upwind and downwind measurement. Here it is assumed that the frequency of deformation is much lower than the frequency of the transducer cycle time, i.e.  $\omega \tau \ll 1$ . Thus at a given dynamic deformation  $\Delta l$  the effect on the measurement increases with increasing frequency of the deformation. For the Thies the cycle time is 3.5 ms which corresponds to 300 Hz.

## Appendix C Data archiving, processing and visualisation

The raw turbulence data are resampled to 50 Hz and to 20 Hz. The 20 Hz and the 50 Hz raw data are brought into the framework of the software package MOBIBASE in the database *ijsselm3*. 10 minute reduced data derived from the 20 Hz timeseries are archived in the datasets *ijsselm3.a10* and a copy with further corrections and derived quantities are archived in *ijsselm3.b10* (10 min values) and *ijsselm3.b30* (30 min values). The same procedure is followed to derive reduced data from the 50 Hz timeseries and archived in the dataset *ijsselm3.e10*, *ijsselm3.f10*, and *ijsselm3.f30* respectively. Production of these database is organized in a script file: *create.sc*. which enable fully or partly reprocessing.

The figures in this report are produced with MOBIBASE, and this is organized in a script file: *create\_figures.sc* which enable easy (re-)processing of all or some of the figures.

Archived in the KNMI Mass storage system (currently at Surf Sara) are under the sub-directory */archive/climate/CABAUW/mobibase/ijsselm3* the following files:

- The raw data files (Original, 50 Hz and 20 Hz)
- The reduced data files with extension .a10, b10, b30, e10, f10, and f30
- The essential MOBIBASE files that defines the database *ijsselm3* which makes it possible to work further on the database with MOBIBASE. This also includes the FORTRAN files specific to this MOBIBASE database.

- The scripts (LINUX tc-shell) to create this database and the figures
- Pdf-s of the earlier intermediate reports

Finally two datasets are available in the KNMI Data Platform (KDP) each consisting of a NetCdf file with the most important reduced parameters from the MOBIBASE *ijsselm3* dataset. The dataset names are *ijsselmeer\_FL47-48\_turb20Hz* and *ijsselmeer\_FL47-48\_turb50Hz*, where the 20 and 50 Hz relates to the raw data files resampling frequency of 20 and 50 Hz respectively, from which these reduced data are derived. A reference to this report is added to the description of this dataset.

**Royal Netherlands Meteorological Institute**

PO Box 201 | NL-3730 AE De Bilt  
Netherlands | [www.knmi.nl](http://www.knmi.nl)